Hotspot formation in polymer-based lightweight PV modules

Rahul Kodali

Delft University of Technology

TU Delft

Hotspot formation in polymer-based lightweight PV modules

by

Rahul Kodali

In partial fulfillments of the requirements for the degree of

Master of Science

In Sustainable Energy of Technology

At Delft University of Technology,

To be defended publicly on August 30, 2023, at 14:30.

Company Supervisor :	Dr. Menno van den Donker
Thesis Supervisor :	Dr. Patrizio Manganiello
Thesis Committe :	Prof. Arno Smets (chair)
	Dr. Pedro P. Vergara (external)
Project Duration :	December, 2022 - August, 2023
Student Number :	5470080
Faculty :	PVMD , Delft

An electronic version of this thesis is available at http://repository.tudelft.nl/

TU Delft Delft University of Technology

solarge

PVMD

Preface

This thesis could not have been completed without the invaluable assistance and resources provided by Solarge and the PVMD faculty at TU Delft. It was my privilege to work under the supervision of Patrizio and Menno, who not only provided expert guidance and encouragement but also assisted me in overcoming any obstacles encountered during the nine-month duration of this project. Their expertise in the field and understanding of the subject matter provided me with the clarity and direction I needed to move forward with my research. I was also given a lot of freedom to pitch new experimental designs, and my supervisors were always eager to hear my findings. This dynamic of constructive feedback followed by iterative implementation of changes is what brought this thesis to fruition.

A special thanks to Henk Stijvers for generously allowing me to use their equipment at TNO, Soliance, and Joeren Pijs (Hopper) for his assistance around the pilot-line at Solarge. I would also like to acknowledge Stefaan Heimans for his help in setting up and customizing the equipment in the Esp lab at TU Delft to my requirements, which allowed me to conduct the majority of my experiments. Lastly, Jurriaan Peeters from the Process & Energy department of the faculty of 3ME, TU Delft, for lending his multi-disciplinary insights on heat transfer in solids, which arose curiosity in a new perspective to comprehend hot-spots from a different stand-point.

I am also deeply grateful to my colleagues and friends, Raju,Mihir, Sathya, and Alonzo, for their constant support and encouragement throughout my research. Their belief in my abilities has been a constant source of strength and has fueled my determination to persevere through the challenges presented during this project.

I am truly delighted for the opportunity to delve into a topic that I am passionate about and to share my enthusiasm with the readers of this paper. While I hope that these findings have the potential to make a meaningful impact on the field, I also humbly recognize that there is always more to learn and that my contributions are a small drop in the ocean compared to all those who have worked before me. Sir Issac Newton once remarked, ”If I have seen a little further, it is by standing on the shoulders of giants”.

Rahul Kodali
Delft, September 2023

Abstract

This thesis presents experimental research on a phenomenon that has been widely observed in photovoltaic systems in recent years. Hot-spots, most commonly reported as areas of extreme temperature within PV modules, have been identified as a critical issue in the industry. This is primarily due to the fact that solar cells are subjected to various mismatches and time-varying stresses in real-world operation, affecting their long-term reliability. Moreover, hot-spots are mostly invisible to the naked eye and require special inspection such as EL and IR imaging for detection, making them challenging to solve. The use of low-temperature lamination techniques on the front sheet and encapsulation increases the risk of hot-spots within Solarge's polymer-based lightweight modules, with permanent damage being observed after exceeding temperatures beyond 160°C. Therefore, robust design criteria were needed to pass the hot-spot certification test, which was developed keeping in mind the thermal limits of failure for the polymer module.

This study provides an overview of contemporary cell technologies, encompassing Passivated Emitter and Rear Cell (PERC) and Interdigitated Back Contact (IBC), in the context of reverse bias characterization. The methodology involves comprehending hot-spot behavior across various configurations, beginning from single-cell laminates to strings, followed by module-level testing. The experiments include the assessment of various commonly used industry wafer sizes to evaluate cell breakdown properties and performance using IV curve analysis. Notably, two electrical processes contribute largely to the power dissipation in a solar cell in reverse: zener and avalanche breakdown. The investigation revealed cell breakdown voltages of -5.2V for IBC cells and -19.6V for PERC cells. These findings were consistent with values provided by manufacturers, reinforcing the widely accepted nature of the cells. The main objective of the investigation of a string or a module of cells in series without bypass diodes was to identify cells with lower performance, which increases the vulnerability to the emergence of hot-spots.

The hot-spot endurance test was conducted on a standard polymer module, in accordance with the IEC 61215 guidelines, revealing essential parameters that significantly impact the resulting temperatures. A notable observation that emerged was the linear correlation between string length and power dissipation. This trend became evident when temperature values exceeded 165.84°C, accompanied by power dissipation of 150–200 watts and heat flux ($\dot{Q}$) ranging from 0.52 to 0.69 W/cm^2 for string lengths up to 24 cells in series. This led to irreparable damage to the module and the failure of the endurance test. Therefore, to pass the test, the string length was confined to less than 20 to stay below the thermal threshold. In addition, the findings included broader observations delving into intricate topics of hot-spot characteristics such as shape, frequency of occurrence, location, shading ratios, orientation, and various other relevant parameters. Hot-spot detection can be used to assess module health and enable proactive maintenance strategies. Understanding the phenomena of cell breakdown and power dissipation assists in the development of safer modules. Finally, this study aims to emphasize the importance of design considerations and offers the potential for optimized module architectures for the industry.

Contents

List of Figures

List of Tables

Nomenclature

Abbreviations

Abbreviation	Definition
EL	Electroluminescence
IBC	Interdigitated Back Contact
IEC	International Electrotechnical Commission
IR	Infrared
NREL	National Renewable Energy Laboratory
PERC	Passivated Emitter Rear Contact
PV	Photovoltaic
ReBEL	Reverse Bias Electroluminescence
SABIC	Saudi Arabia's Basic Industries Corporation
STC	Standard Test Conditions

Symbols

Symbol	Definition	Unit
V	Voltage	[V]
I	Current	[A]
P	Power	[W]
I_{sc}	Short circuit current	[A]
V_{oc}	Open circuit voltage	[V]
V_{mp}	Maximum Power Point Voltage	[V]
V_T	Thermal Voltage	[V]
V_{br}	Breakdown Voltage	[V]
V_{AB}	Avalanche Breakdown Voltage	[V]
V_Z	Zener Breakdown Voltage	[V]
V_{sh}	Shaded Voltage	[V]
I_{mp}	Maximum Power Point Current	[A]
I_{ph}	Photogenerated current	[A]
I_{rev}	Reverse current	[A]
I_D	Diode current	[A]
I_0	Saturation current	[A]
$I_{leakage}$	Leakage current	[A]
FF	Fill Factor	[-]

k_B	Boltzmann constant	[J/K]
q	Electron charge	[C]
R_{sh}	Shunt or parallel resistance	[Ω]
R_s	Series resistance	[Ω]
T	Temperature	[°C]
P_{diss}	Power dissipation	[W]
P_{illum}	Illuminated source Power	[W]
P_{ph}	Photogenerated Power	[W]
P_{rev}	Reverse bias Power	[W]
ξ_{cr}	Electric field	[V/cm]
R	Resistance	[Ω]
$\dot{Q}$	Heat flux	[W/m^2]
A_{cell}	Cell Area	[m^2]
$A_{effective}$	Unshaded cell Area	[m^2]
x%	Shading factor	[%]
SR	Shading rate	[-]
G	Illumination	[W/m^2]
Ln	Electron diffusion length	[m]
Lp	Hole diffusion length	[m]
N_A	Acceptor concentration	[cm^{-3}]
N_D	Donor concentration	[cm^{-3}]
D_N	Electron diffusion coefficient	[m^2/s]
D_P	Hole diffusion coefficient	[m^2/s]
E_g	Bandgap	[eV]
n_i	Intrinsic carrier concentration	[cm^{-3}]
M	Multiplication factor	[-]
S	String length	[-]
β	Temperature coefficient breakdown	[/°C]

1 Introduction

This section provides a detailed introduction to the thesis's main topic in section 1.1 by providing some context, followed by a background on the company Solarge in section 1.2. After briefly describing the preface, we start delving into the basic problem at hand and emphasizing the need for a more thorough analysis in section 1.3. Along with the topic, an overview of research questions is provided, laying the groundwork for further hot-spot investigation in section 1.4. Finally, the outline of the report is summarized in section 1.5.

1.1. Context

Hot-spots in partial shading are a complex and multifaceted phenomenon that have garnered significant attention in the PV industry due to its negative impact on module performance [1]. Hot-spots refer to areas on the module that experience a significantly higher temperature than the surrounding cells, leading to local overheating. This phenomenon is particularly prevalent in partial shading conditions, where the incident light on the module is non-uniform [2]. Hot-spots can occur as a result of mismatches in the electrical characteristics of the cells, leading to non-uniform current distribution and increased resistance in certain areas. The occurrence of hot-spots can significantly reduce the lifetime and efficiency of PV modules, making it an important topic of study in the industry [3].

PV modules are subject to various unexpected and time-varying stresses in real-world operation, affecting their long-term reliability [4]. Understanding how these stresses interact in complex environments is crucial for examining irreversible degradation mechanisms. Conventional indoor testing often fails to capture the effects of multiple stresses, mimicking the natural environment in which modules are installed. Hot-spots can be created by various unknown conditions and stresses as shown in Figure A.2, which illustrates the complex relationships between these degradations. Standardizing accelerated tests to meet updated field conditions is required in a rapidly evolving industry with the introduction of new and unfamiliar materials into their manufacturing processes. Experts at NREL have stated that "standards are not intended to serve as a guarantee of quality or reliability. The industry has been forced to design standards around known failures rather than develop a more comprehensive testing regime capable of detecting unexpected failure modes more frequently prior to deployment" [5].

PV installations in practice, face dynamic shading topologies with complex patterns, resulting from various nearby objects like: leaves, bird droppings, obstructions, clouds, and self-shading during different times of day being common occurrences among others depicted in Figure 1.1.

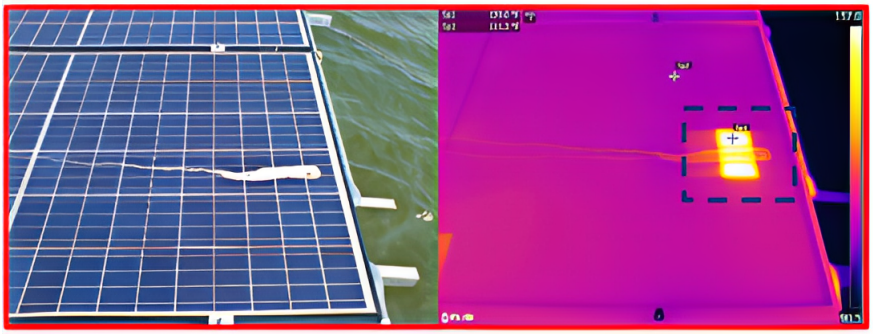

Figure 1.1: Partial shading (bird-dropping) causing a localized hot-spot on the module [6]

Furthermore, these shading patterns tend to shift periodically over an extended time period as a result of moving objects, changing sun angles, or varying cloud cover, with different areas of the cell being affected differently, causing hot-spots to shift their location with them. This unpredictable nature of hot-spots highlight the complexities involved in dealing with shading effects in PV systems. However, the scope of this thesis focuses mainly on the investigation of scenarios that adhere to the rigorous testing standards outlined in IEC 61215. A concise explanation of the intricacies of long-term hot-spot scenarios are addressed separately in the appendix A.1.

1.2. Solarge Lightweight Modules

Solarge is a developing manufacturer in the solar industry that specializes in producing lightweight circular solar modules. Through their innovative approach to PV module technology, they have developed a polymer-based design that is lightweight, efficient, and cost-effective. Solarge's panels are versatile and can be used in residential, commercial, and industrial projects. They are easy to install and provide a high power output per unit area, comparable to conventional solar panels, due to the polymer design that Solarge has adopted [7].

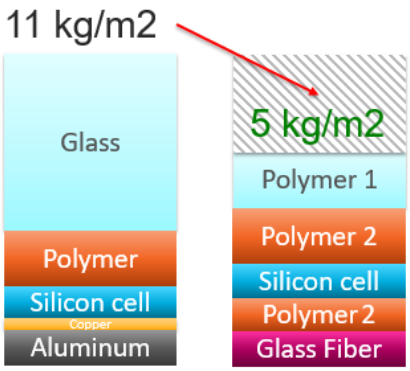

Figure 1.2: Layout of conventional module (left) and Solarge module (right) [7]

The proposed design of PV modules comprises of a slimmer-based front and back-sheet that retains the strength of a conventional glass front sheet or nPV module with a metal frame. Solarge's SOLO module weighs 5.5 kg/m^2, while typical glass modules weigh around 11–16 kg/m^2,which makes them approximately at least 50% or more lighter. The module consists of specially developed fibre reinforced polymers from the company SABIC. The manufacturing process involves laminating solar cells at around 160°C on polymer-based front and back sheets, providing the module with [8].

The panels are highly resistant to corrosion, UV rays, and other environmental factors, ensuring that they are a reliable and long-lasting solution for solar energy needs. Furthermore, the lightweight design of their panels reduces the load on structures and rooftops, which helps to decrease installation costs and prolong the life of supporting structures [9].

1.3. Problem statement

The impact of hot-spots on PV module performance has been well documented in the literature, with numerous studies highlighting the detrimental effects on cell efficiency and lifetime [10]–[13]. Hot-spots can lead to localized cell degradation and also induce thermal cycling stress on the PV module, resulting in mechanical failure and decreased system reliability due to de-lamination, encapsulant damage, and cracks. This may necessitate frequent inspection for component maintenance and replacement, which can be both expensive and time-consuming. As a result, understanding the underlying causes of hot-spots in partial shading is critical, as is devising strategies to mitigate their negative impact on PV module performance [14].

As mentioned earlier in in section 1.1, hot-spots are a particularly concerning issue for PV systems that experience partial shading due to a variety of factors, such as nearby trees, buildings, bird droppings, or other obstructions [15]. In fact, hot-spots appear to be the most pronounced and dangerous mode of degradation in systems installed in the last 15 years, in large part because of their high severity ranking [16]. A detailed overview of degradations that occur in PV modules is provided in the appendix A.1.

Another subject previously discussed in section 1.2, Solarge's polymer-based module is laminated at 160°C, as the encapsulant material melts to adhese to the different layers. If this temperature threshold is exceeded during operation, the module risks de-lamination. This lays the foundation to the scope of this thesis as Solarge is motivated to formulate and update safety design guidelines for their modules, with a focus on addressing hot-spots.

1.4. Research Questions

The main objective of this thesis is to conduct a comprehensive investigation into the phenomenon of hot-spots in photovoltaic cells, strings and modules, with a particular focus on partial shading scenarios. The aim is to uncover the underlying factors driving hot-spot formation and the fundamental mechanisms in solar cells and understand their impact on module safety using targeted research questions. Finally, it is necessary to apply the insights gained by studying the hot-spot phenomenon to perform and pass the hot-spot endurance test in accordance with IEC 61215 standards for the Solarge PV modules.

- How do the reverse bias characteristics of different cell technologies vary under different operating conditions?
- What are the worst-case scenarios that lead to hot-spot formation in different cell technologies under partial shading?
- What is the maximum number of cells that can be safely connected in series for different cell technologies under partial shading conditions to minimize the risk of hot-spot formation?
- What methods can be used to predict the formation and occurrence of hot-spots in specific locations, and which parameters are considered to characterize hot-spots?
- What design approaches can be used to reduce the risk of hot-spots in polymer-based solar modules and ensure a hot-spot-resistant design?

1.5. Report Outline

The thesis focuses on answering the above research questions, starting with background theory on the general working principles of solar cells and PV modules under normal and non-uniform operating conditions, as presented in chapter 2. It is important for the reader to also understand the fundamentals of the reverse bias characteristics of solar cells, as this lays the foundation for understanding hot-spots. The following chapter 3 dives into an extensive literature study on hot-spots in depth. Having done this literature study, it is possible to better specify the methodology that is embedded in an experimental investigation of cell and module behaviour that leads to hot-spots, which is elaborated in chapter 4. In the following chapters, chapter 5, the required experimental setup is presented. These two chapters lead to the results obtained, which are shown in chapter 6. Finally, a conclusion and a recommendation of a new guideline for reducing hot-spot behaviour and providing an overview of configurations are presented in chapter 7.

2 Theory

The following sections of this study are devoted to presenting crucial theoretical concepts. Section 2.1 provides an in-depth examination of the basic operation of a solar cell, while section 2.2 analyzes the representation of a solar cell through the use of an equivalent circuit.The current-voltage characteristics and their response to illumination are outlined in section 2.3. Additionally, section 2.5 conducts a comprehensive analysis of the operational behavior of a solar cell under varying temperature conditions to understand their relation in the coming chapters. A brief understanding of electrically matching two or more solar cells in series and parallel are discussed in section 2.4. Finally, the impact of partial shading and illumination on solar cells is thoroughly examined in section 2.6.

2.1. Solar Cell Operation

The underlying principle for the operation of solar cells is based on the photovoltaic effect, a physical process where the absorption of light by a material produces an electrical current [17]. The photovoltaic effect arises due to the excitation of electrons by illumination, which migrate to the conduction band, including photon absorption, carrier generation and separation, leaving behind positively charged holes in the valence band diagram shown in Figure 2.1a. This creates a voltage difference, driving an electric current through an external circuit. Figure 2.1b provides a visual representation of the functioning of a solar cell.

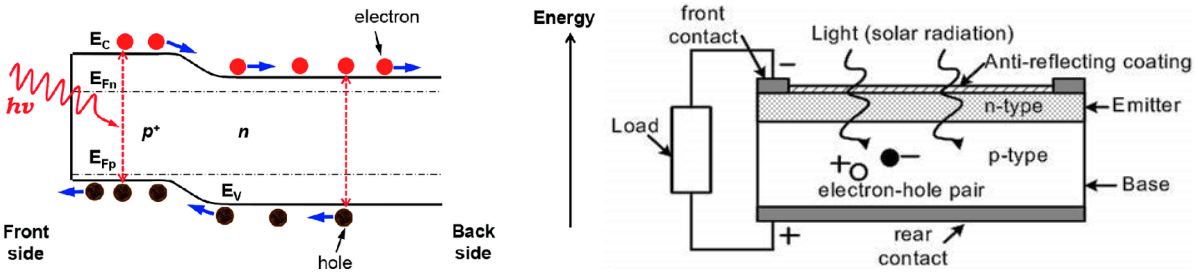

(a) (b)

Figure 2.1: (a) Depicts a schematic of an energy band diagram of n-type silicon solar cell in non-equilibrium under illumination [17] (b) Schematic of the operation principle of a solar cell [18].

2.2. Equivalent circuit of a solar cell

An equivalent circuit model can be constructed to analyze and predict the electrical behavior of a solar cell. For a single-junction PV cell, which does not receive illumination, it behaves in a similar manner as a semiconductor diode [19]. The equivalent circuit is composed of a current source, denoted as I, which represents the internal cell current. A diode, symbolized by a current-controlled voltage source V, captures the characteristics of the diode. Additionally, a series resistor, R_s, signifies the presence of series resistance leading to a voltage drop across the cell. The current source I_L is indicative of the photo-generated current, produced by solar irradiance. On the other hand, the diode I_D illustrates the non-linear current-voltage relationship of the solar cell. Finally, R_{sh} signifies the presence of a parallel resistance that enables current to flow in alternate paths. The components under discussion are depicted in Figure 2.2.

2.2.1. Single diode model

The single diode model can be used to mathematically describe the operation of a solar cell. This model is simplified, but it provides an intuitive and good approximation of the behavior of a solar cell under most operating conditions [1]. The equivalent circuit of a single diode model is depicted in Figure 2.2.

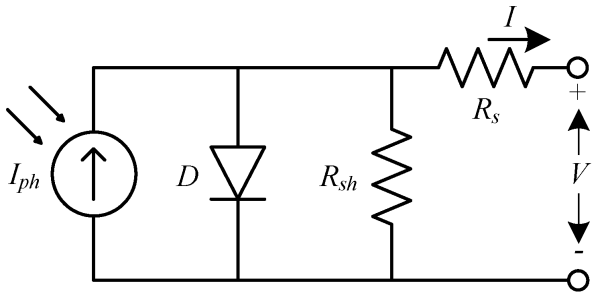

Figure 2.2: Equivalent circuit of the single diode solar cell model [20].

The I-V characteristic of the single diode model for an ideal cell can be represented by the Shockley diode equation, which describes the relationship between the current I_D and voltage V across the diode. The total current in the external load, I, is provided by the following equation using Kirchoff's current law:

$$I = I_{ph} - I_D - I_{sh} \tag{2.1}$$

The leakage current though the shunt resistance can be mathematically defined as :

$$I_{sh} = \frac{V + IR_s}{R_{sh}} \tag{2.2}$$

The Shockley diode equation under dark conditions is given by:

$$I_D = I_0 \left[\exp\left(\frac{q(V + IR_s)}{nk_BT} \right) - 1 \right] \tag{2.3}$$

where I_0 is the saturation current, q is the electronic charge, n is the ideality factor, generally assumed to be equal to 1, k_B is the Boltzmann constant, and T is the temperature in Kelvin.

[1] Refer diode equation 3.7 for reverse bias conditions.

Under illumination and by combining equations 2.1, 2.2 and 2.3, the single-diode equation describing the operation of a solar cell can be written as:

$$I = I_{ph} - I_0 \left[\exp\left(\frac{q(V + IR_s)}{nk_BT} \right) - 1 \right] - \frac{V + IR_s}{R_{sh}} \tag{2.4}$$

The effectiveness of the single-diode model in determining parameters under dynamic weather conditions such as I_L , I_0, R_s, R_{sh}, and n has been observed in [21].

2.2.2. Double diode model

The ideality factor n is assumed to be a constant in the single diode equation. The ideality factor is determined by the voltage across the device. When the recombination is dominated by the surfaces and bulk areas at high voltage, the ideality factor approaches one [22]. However at lower voltages, junction recombination is represented by attaching a second diode to the first and setting the ideality factor to two as shown in Figure 2.3. In practice, solar cells often exhibit ideality factors in the range of 3 to 4 due to ohmic shunting and recombination [23].

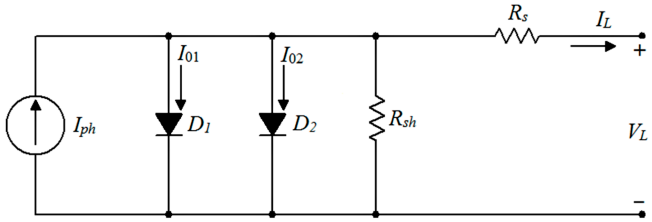

Figure 2.3: Equivalent circuit of the double diode model [19]

The equation of the double diode model under illumination is :

$$I = I_{ph} - I_{01} \left[\exp\left(\frac{q(V + IR_s)}{k_BT} \right) - 1 \right] - I_{02} \left[\exp\left(\frac{q(V + IR_s)}{2k_BT} \right) - 1 \right] - \frac{V + IR_s}{R_{sh}} \tag{2.5}$$

Research has shown that using a two-diode model to analyze PV cells in different operating conditions is more accurate than the single-diode model [24], for instance during partial shadowing. As a result, many researchers have adopted this model for the electrical analysis [25].

2.3. Forward IV Characteristics

The IV curve of a solar cell is a graphical representation of the relationship between the current flowing through the cell and the voltage difference across it. The IV curve is used to characterize the electrical performance of a solar cell, as it provides important information about the cell's electrical behavior under different illumination conditions [26]. The IV curve is plotted by measuring the current flowing through the cell at a series of different voltage levels and plotting these values as a graph, as shown in Figure 2.4. The IV curve typically exhibits non-linear behavior deviating from Ohm's law when a voltage is applied, with different regions of the curve representing different physical processes occurring within the solar cell [27]. The fundamental electrical parameters of a solar cell that can be derived from its IV curve include the I_{sc}, V_{oc}, FF and the P_{mp}.

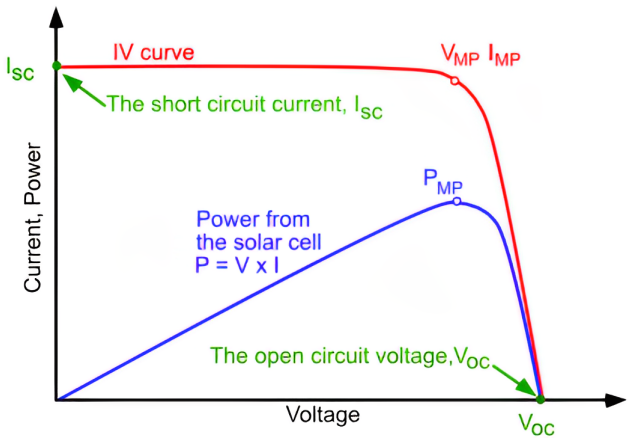

Figure 2.4: Typical IV curve of a solar cell operating under forward bias [26]

2.3.1. Solar cell parameters

The short-circuit current, I_{sc} is the current that flows through the cell of area A_{cell} under short-circuit conditions.

$$I_{sc} = qG(L_n + L_p)A_{cell} \tag{2.6}$$

where G denotes the generation rate, representing the rate at which electron-hole pairs are produced by incident light. Meanwhile, L_n and L_p signify the electron and hole diffusion lengths, respectively. They quantify the distance over which minority carriers can move before recombination, offering insights into the transport properties within the solar cell. The open-circuit voltage, V_{oc}, is the voltage across the cell when no current is flowing through it. This value represents the voltage that can be produced by the cell under open-circuit conditions [28].

$$V_{oc} = \frac{nk_BT}{q} ln\left[\frac{I_{sc}}{I_0} + 1\right] \tag{2.7}$$

Here the saturation current I_0 is given by the expression:

$$I_0 = qAn_i^2\left[\frac{D_N}{L_N N_A} + \frac{D_P}{L_P N_D}\right] \tag{2.8}$$

The fill factor, FF, is a measure of the efficiency of the cell and is defined as the ratio of the maximum power produced by the cell to the product of I_{sc} and V_{oc}. A higher fill factor indicates a more efficient cell [29].

$$FF = \frac{V_{mp} \cdot I_{mp}}{V_{oc} \cdot I_{sc}} \tag{2.9}$$

The maximum power, P_{max}, refers to the point on the IV curve where the product of the current and voltage is at its maximum value. This is the operating point at which the cell produces the maximum power under a given set of conditions.

$$P_{max} = V_{oc} \cdot I_{sc} \cdot FF \tag{2.10}$$

The IV curve is a valuable tool for characterizing the electrical behavior of solar cells and determining the fundamental electrical parameters that govern their operation. By analyzing the IV curve, it is possible to understand the performance limitations of a solar cell and to make informed decisions regarding its design and optimization [30].

2.3.2. Dark IV Characteristics

The I-V curve of a solar cell can be measured in dark by injecting carriers rather than using photo-generated carriers in illuminated measurements. A controlled power supply enforces electrical current, moving from the positive contact to the negative contact. Current and voltage are simultaneously recorded as the voltage increases incrementally up to a specified limit. Notably, this approach reverses the current direction compared to light-exposed conditions while maintaining the p-n junction in a forward bias configuration. This technique is effective in removing subtle variations in the irradiance intensity that can occur during measurements.

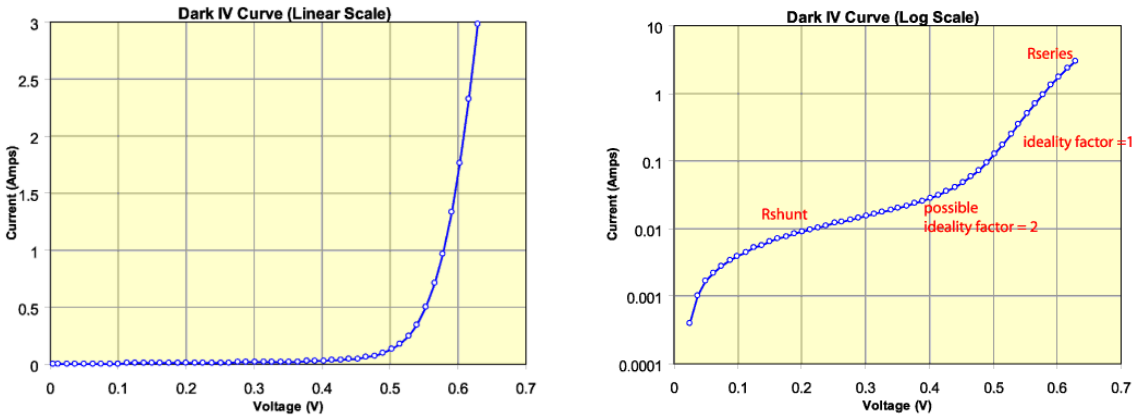

Figure 2.5: Dark IV curve with a (a) linear scale (b) Semi-log plot depicts loss mechanisms dominating different regions [31].

The Dark IV measurements are also useful for determining intrinsic features of a solar cell such as the diode ideality factor (n), a dimensionless parameter, signifies deviations from ideal diode behavior and dark reverse saturation current (I_0). Further, the series resistance (R_s) and shunt resistance (R_{sh}) are extracted from the slope and intersection points of the dark IV curve. These resistances quantify the impact of internal and external losses on the cell's performance. In the dark, light-induced effects are absent, and IV measurements aid in finding defects and non-idealities in solar cells, which benefits the understanding of the device properties that would otherwise remain obscured under illuminated conditions [32].

2.4. Series and Parallel connected cells

Solar cells connected in series have a total output voltage equal to the sum of the individual cell voltages, yet the current output is constrained by the current of the least performing cell. When a solar cell is briefly shaded, it experiences mismatched operating conditions due to varying levels of irradiance. A complex sequence of events occurs when the operating current of an unshaded cell in a string exceeds the short-circuit current of the shaded cell. The shaded cell cannot match the current produced by other cells, as the remaining cells continue to hold the shaded cell in reverse bias until the shading disappears or the cell is completely damaged. Operating under such reverse-bias conditions causes electricity generated by light to be converted to heat, resulting in hot-spots. These hot-spots only become dangerous when certain specific current, voltage, and temperature conditions are reached in order to create a breakdown.

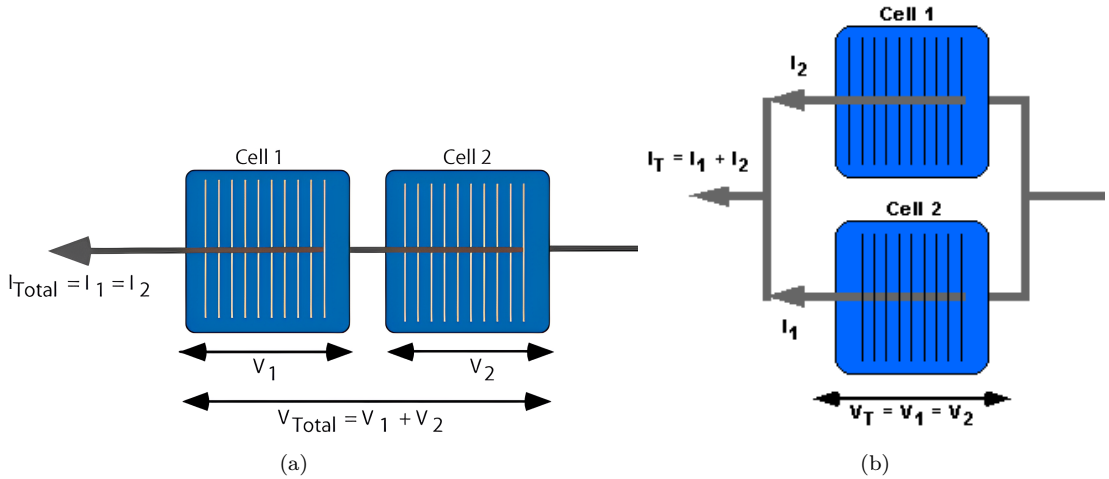

Figure 2.6: (a) Series connection [33] (b) Parallel connection [34].

When solar cells are connected in parallel, the current output of the module or array equals the sum of the currents of each individual cell, while the voltage output is limited by the voltage of the lowest performing cell. If one cell in the parallel string has a lower current output than the others, it reduces the overall current output of the module or array. If the cell in parallel has a lower voltage output than the rest, it will limit the overall voltage output of the module or array. Mismatches can reduce power output, cause hot-spots, and other reliability issues. The extent and nature of the mismatch and the system configuration determine this effect.

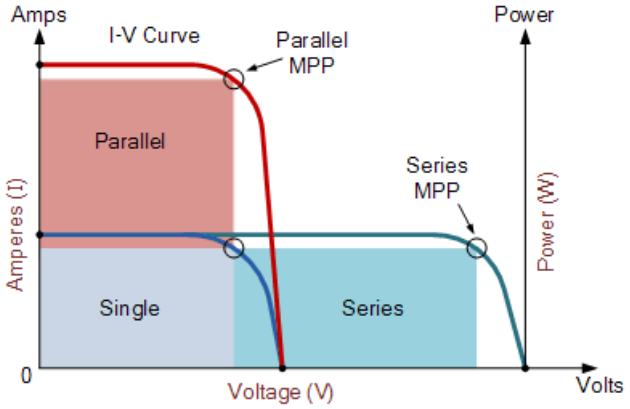

Figure 2.7: Series and parallel IV characteristic curves [35]

2.5. Temperature

Temperature is a critical parameter that has a significant influence on the electrical properties of a solar cell. As the temperature rises, the IV curve experiences a very slight increase in current and a more significant decrease in voltage, as shown in Figure 2.8. The change in I_{sc} with temperature is more dependent on the design of the cell than the semiconductor material properties. Conversely, V_{oc} depends largely on the band-gap of the material and is limited by the recombination processes, which are both temperature-dependent [36].

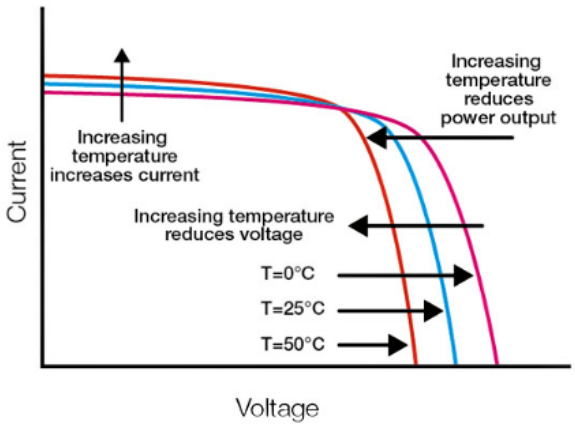

Figure 2.8: Effect of temperature on IV curves [37]

2.5.1. Bandgap

The bandgap (E_g) is the energy difference between the highest energy level in the valence band and the lowest energy level in the conduction band of a material, representing the energy required for an electron to transition from the valence band to the conduction band. The bandgap decreases at higher temperatures due to carrier excitation by thermal energy, allowing for greater absorption of photons with lower energy, leading to higher intrinsic carrier concentrations [38]. This intrinsic carrier concentration (n_i), a key property of the material, has a strong temperature dependence [2], resulting in an increased number of charge carriers available for photo-current generation (I_{ph}) as shown in equation 2.8.

$$n_i^2 = BT^3 \exp\left(\frac{E_g}{k_B T}\right) \tag{2.11}$$

2.5.2. Temperature Coefficients

Solar cells are typically designed for and characterized under standard test conditions (STC). STC refers to the standardized evaluation parameters employed in photovoltaic studies to assess the performance of solar cells and modules. These conditions encompass an incident irradiance of 1000 W/m², an AM1.5 spectral distribution, and a temperature maintained at 25°C [28]. However, in real-world applications, the operating temperature of solar panels can deviate significantly, up to 85°C. To account for the temperature effects on solar cell performance, temperature coefficients play a crucial role, denoted as alpha (α), beta (β), and gamma (γ). For example, typical values for these coefficients at 300 K for silicon are around 0.06% per °C for current (α), -0.43% per °C for voltage (β), and -0.4% to -0.5% per °C for power (γ) [36].

It's worth noting that these temperature coefficients are not fixed constants and can vary from one cell technology to another as well as among different cell designs. This inherent variability underscores the complexity of solar cell behavior under changing temperatures.

[2] B is a constant independent of temperature.

2.6. Effect of Partial shading

As discussed in section 2.4, solar cells need to be electrically matched in order to operate efficiently. When a string of cells contains one or more mismatched cells due to issues like a cracked or partially shadowed cell, an internal load is created by allowing the flow of reverse current. The power dissipation and hot-spot production brought upon by this internal load ultimately results in a reduction of the total array power output [39].

The architecture of a solar cell is complex, with an organized layout of front and back contacts, intricate conducting pathways known as fingers, and pivotal electrical conduits known as busbars. These components are critical in channeling and managing the flow of electric current within the cell as shown in Figure 2.10. The fingers, which are narrow conducting lines on the cell's surface, serve to distribute the collected current from the light-absorbing region across the surface area of the cell to the sides. Busbars, on the other hand, play an important role as larger conducting pathways that facilitate the transfer of accumulated current from the fingers to the external circuit [28].

Shading patterns have a significant impact on cell performance due to their effect on current flow through the busbars. When shading perpendicular to the busbar, the power loss is minimal, whereas when shading occurs parallel to the busbar, results in a drastic reduction in current as shown in Figure 2.9. This distinction arises from the way shading disrupts the electrical connections within the cell.

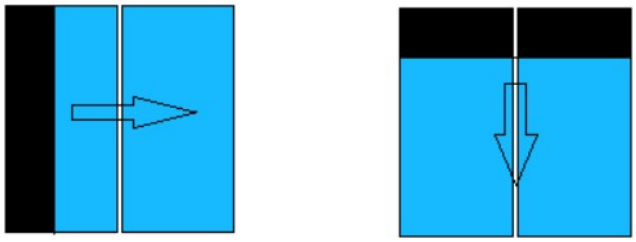

(a) (b)

Figure 2.9: Opaque shading direction (a) parallel to the busbar and (b) perpendicular to the busbar [40]

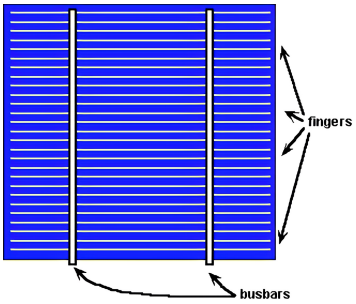

Figure 2.10: Schematic of cell contacts: busbars and fingers [41]

2.6.1. Illumination dependence

In a recent study [42], it was reported that the partial shading of a solar cell is indeed equivalent to reducing the irradiance of the entire cell by the same amount of light intensity, depicted in the Figure 2.11. This observation suggests that these two distinctive physical phenomena create identical changes in the electrical parameters of solar cells, assuming that light distribution is homogenous across the cell and the collections of carriers at the contacts are equal. The key variation between these two shaded and unshaded regions was their shunt resistances, which decreased linearly as the illumination increased [43].

Figure 2.11: Shaded cell and its equivalent circuit diagram using a modification of Bishop's model [44]

The split-cell model describes partial shading in cells with illumination-dependent leakage current behavior, causing hot-spots due to high reverse current densities. The cell is divided into parallel-connected light and dark sections under partial shading, and uses Bishop's equation to determine un-shaded I-V parameters by varying the shading rate (SR) from 0 to 1. The current flowing through a cell (I_{ph}) is proportional to the incident light intensity (G). Hence, the shading factor (x)% which is used as a mathematical notation instead of (SR), determines the amount of reverse current in the partially shaded cell and can be modeled by:

$$I_{rev} \approx I_{ph} \cdot (1 - x) \tag{2.12}$$

3 Literature study

This literature review is an important part of this thesis because it provides the necessary background knowledge and context for the subsequent research. Section 3.1 examines current market trends as they relate to the experiments' coverage of various cell technologies. Section 3.2 discusses the two most important topics of interest, namely the characteristics of hot-spots and power dissipation, followed by section 3.3, which discusses the reverse characteristics of a solar cell. Furthermore, section 3.4 thoroughly explains in depth the phenomenon of cell breakdown observed in reverse bias.

3.1. Cell technology

Current trends, such as new cell designs, larger wafer sizes, and higher module ratings with more interconnected cells as shown in Figure 3.1, make it a critical topic to ensure a long lifetime of the module [45]. One reason driving this change is the fact that manufacturing costs in the solar industry have been decreasing over the decades, and there has been a competitive push towards more efficient designs.

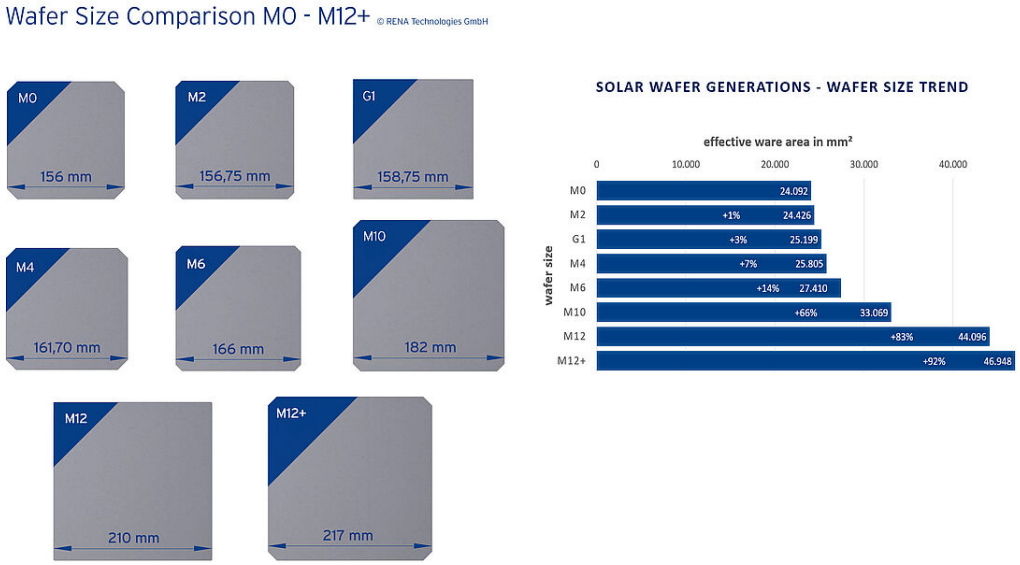

Figure 3.1: Wafer sizes of the current PV industry [46]

3.1.1. PERC Vs IBC Cell

PERC (Passivated Emitter Rear Cell) is an advanced solar cell design that has gained significant popularity in the industry. It features an additional layer of passivation at the rear, reducing recombination and enhancing light absorption, as shown in Figure 3.2a. This enhancement allows PERC cells to generate more electricity and operate with higher efficiency. As a result, PERC technology has been widely embraced and is now a dominant design in the industry [47].

Similarly, the interdigitated back contact (IBC) cell has captured considerable attention due to its potential to achieve high efficiency. The cells feature continuous p+ and n+ contact regions interdigitated on the rear side, as illustrated in Figure 3.2b. A recent development, known as ZEBRA technology, which has been under development for several years at ISC Konstanz, is a bi-facial cell concept that is currently the most cost-effective IBC technology on the PV market. It uses a standard industrial, low-cost manufacturing process without passivating contacts. Moreover, ZEBRA cells have been reported to reduced light-induced degradation and can convert light to electricity more effectively than PERC cells [48].

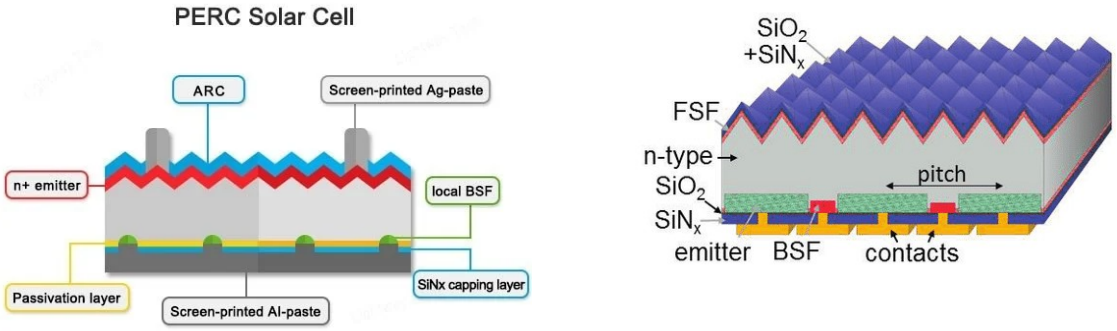

(a) (b)

Figure 3.2: (a) Schematic of a PERC cell design [49] (b) Schematic of IBC cell architechture [50]

Table 3.1: Overview of cell technologies

Cell Design	Configuration	Busbars	Manufacturer	Remarks
P-type Mono PERC Full-cell	M10-182mm	10	AIKO [51]	Cut-edges
	M6 – 166mm	9		
	G1 -158.75mm	5	DMEGC [52]	Square-edges
P-type Mono PERC Half-cell	G1 -158.75mm			
	M10-182mm	10	AIKO [51]	Cut-edges
N-type IBC Full cell	M6 – 166mm	Inter-digitated	SPIC [53]	Zebra technology
	125 mm		SUNPOWER [54]	Hot-spot-resistant Design
N-type IBC Half-cell	M6 – 166mm		ISC KONSTANZ [55]	Zebra technology

As cell technology has advanced in complexity, manufacturers have focused on producing cells with evenly distributed leakage currents as a deliberate design choice to avoid hard breakdown and other mismatch issues that lead to degradation. Section 3.4 provides a detailed explanation.

3.1.2. Half-cell Vs Full-Cell

In recent years, solar cells have undergone a significant transformation in their manufacturing process, with the ability to increase power output without significant alterations. One of the latest advancements is the development of half-cut cells with PERC and IBC technology, which are created by dividing conventional cells in half. This results in a single module with 120 or 144 cells instead of the conventional 60 or 72 cells. Despite producing the same voltage as a standard cell, half-cut cells generate half the current over half the area, giving them the same current density as a full cell. To compensate for this configuration, the cells are arranged in parallel strings to match the voltage and current ratings of a conventional full-cell module [56].

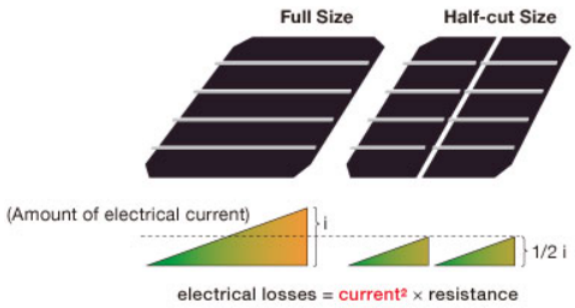

Figure 3.3: Schematic of a full-cell vs half-cut cell depicting when the area of a solar cell is cut in half, the power losses are reduced by a factor of four [57].

The manufacturing process of a Half-cut cell involves cutting a full cell into two halves using a laser scribe and cleaving (LSC). However, this introduces mechanical stress at the cut edge due to pressure and thermal effects, potentially impacting structural integrity and electrical performance like conductivity, shunting and recombination losses [58]. Half-cut modules are more resistant to hot-spots and shade-tolerant than conventional solar cells. Due to the topology used to connect half-cut cells in a panel, with cells in a string in series and half of the module in parallel with the other, a single shaded cell can isolate a sixth of the total power output produced by the panel by limiting current, rather than one-third of the loss in a traditional full-cell module, as depicted in Figure 3.4.

Table 3.2: Comparison of parameters for half-cut modules [57].

Parameter	Half-cut cells
Voltage	Same as full cells
Power losses	Reduced by 75%
Current density	Same as full cells
Efficiency	1.5-3% efficiency increase
Cost	About 5-10% higher due to additional manufacturing steps
Hot-spot risk	Lower risk due to reduced shading losses and lower heat dissipation

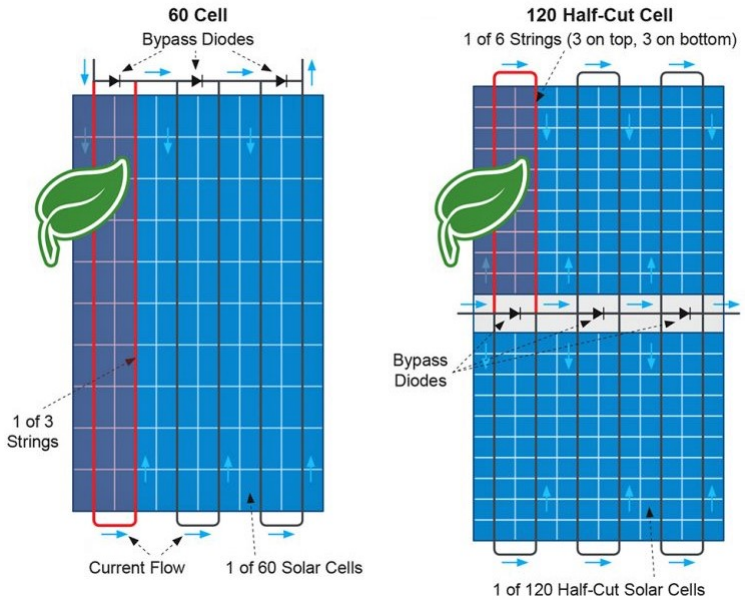

Figure 3.4: The partial shading module arrangement for half vs full cell modules [59]

3.2. Hot-spots

Hot-spots typically form as a result of photo-generated current distribution imbalances in the module, which are frequently caused by mismatch or partial shading of the module by an external object. In the context of heat transfer, hot-spots can be defined as localized areas that generate heat but cannot dissipate it quickly enough to the surroundings, resulting in rising temperatures due to an uneven thermal balance. Several factors influence hot-spot behavior in cell technologies such as: size, area, location, intensity, power dissipation, heat conductivity, cooling mechanisms, material properties, operating conditions, design, and layout.

The relationship between shunts and hot-spots is also well documented in literature, yet what constitutes a shunt is still under discussion [23]. Shunts are essentially non-idealities that degrade the electrical characteristics of solar cells. They can be either ohmic or non-ohmic in nature, as they cannot all be identified or accounted for. However, ohmic shunting occurs frequently by acting as a trap states for recombination, resulting in thermalization and in some conditions, even light emissions have been observed from tiny, randomly distributed points from these shunts [60]. More information is provided in the section 3.4.2.

3.2.1. Power dissipation

While overall power dissipation P_{diss} is important, it is the concentration of power dissipation per unit area $\dot{Q}(x)$ within localized regions that leads to the emergence of hot-spots. Under short-circuit conditions in a string of cells in series, the voltages are added as mentioned in section 2.4 and the heat dissipation from the current limiting cell comes from three sources of power [61], which are as follows:

$$P_{diss} = P_{illum} + P_{ph} + P_{rev} \tag{3.1}$$

P_{illu} is the power from the illumination source that cannot be converted to electricity and has to be dissipated as heat, which is equivalent to a cell in open-circuit state when illuminated [62]. This portion of power is calculated as follows :

$$P_{illum} = G \cdot A_{effective} \cdot a \tag{3.2}$$

where G is the irradiation intensity (W/m^2), $A_{\text{effective}} = A_{\text{cell}} \cdot (1 - x)$ is the effective area that receives light, and a is the cell absorption coefficient[1]. P_{ph} is the power dissipated by the photo-generated current that is dumped by the un-shaded cells to flows through the reverse-biased cell. It can be computed as :

$$P_{ph} = I_{ph} \cdot (1 - x) \cdot (S - 1) \cdot V_{ph} \tag{3.3}$$

Finally, P_{rev} is the power contributing directly to the "hot-spot" effect as shown in Figure 3.5. It can be calculated as:

$$P_{rev} = I_{rev} \cdot V_{rev} \tag{3.4}$$

where I_{rev} is the reverse current flowing through the shaded cell, as described in equation 2.12. The rest of the (S-1) cells in series force the shaded cell to operate in a reverse voltage V_{ph} due to the short-circuit condition. Therefore, by substituting equations 3.2 to 3.4, the total power dissipation (P) is given by [2]:

$$P(x) = (1 - x)\left[G \cdot A_{cell} \cdot a + P_m\right] \tag{3.5}$$

Finally, after simplification, the total power dissipation $\dot{Q}(x)$ is divided by the effective area $A_{\text{effective}}$ and can be expressed as:

$$\dot{Q}(x) = \frac{P}{A} \implies G \cdot a + \dot{Q}_m \tag{3.6}$$

The function P(x) heavily relies on shading rate, while Q(x) exhibits a weaker dependence. When a cell experiences shading by a factor of (x%), the effective area similarly reduces by the same factor. Consequently, reverse current flow and incident illumination decrease by the same factor, meaning the reverse current density remains the same. This linear relationship ensures a consistent $\dot{Q}$ value, irrespective of shading rate. However, incorporating illumination effects on voltage introduces an additional ln(1-x) term, meaning the linearity no longer holds true.

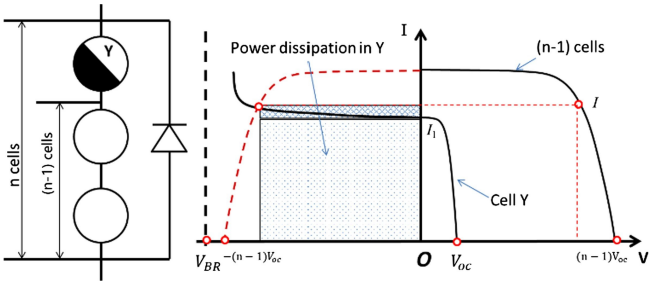

Figure 3.5: Shading of a cell in a string of n unshaded cells in series holding the current in reverse (left), reverse bias dissipation (right) [63]

[1] Assumed to be around 0.81 for the front sheet

[2] The power of the un-shaded part of the module is denoted as $P_m = S \cdot V_{\text{ph}} \cdot I_{\text{ph}}$.

3.3. Reverse IV characteristics

The investigation of reverse IV characteristics has significance, particularly in the context of hot-spots. During reverse bias, which involves applying a voltage opposite to the natural current flow, increases the width of the depletion region as shown below in Figure 3.6. In contrast to forward bias, where the relationship between current and voltage follows relatively straightforward conduction mechanisms, reverse bias presents distinct challenges. Understanding the complicated nature of reverse IV characteristics is critical when dealing with a wide range of phenomena such as leakage current, the influence of thermally generated minority carriers, and other currents associated with breakdown phenomena.

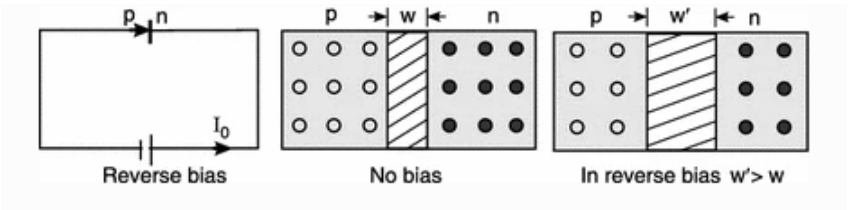

Figure 3.6: The thickness of depletion layer w increases in reverse biasing

In theory, a reverse IV curve even in the absence of light would have a very small magnitude of saturation current (I_0)[3] leaking through the width of the depletion region given by the equation 2.8. This current is caused by the diffusion of minority charge carriers is produced by thermally generated electron-hole pairs [64]. Although the minority charge carriers are strongly temperature-dependent, in theory they are almost completely independent of the applied bias voltage as shown in Figure 3.7.

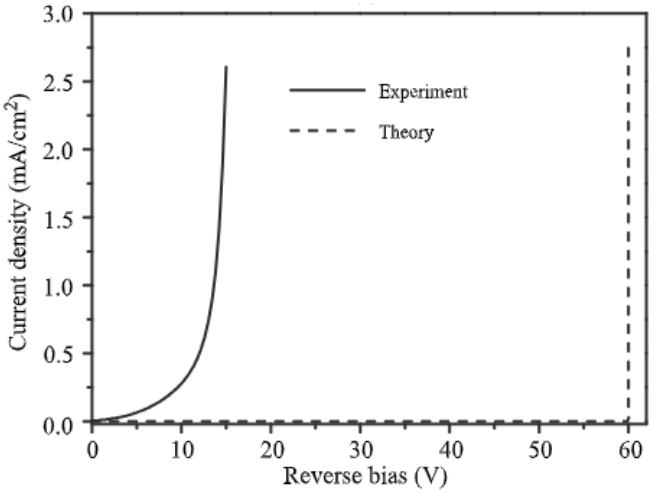

Figure 3.7: Comparison of theoretical vs experiment measured dark reverse IV curves [65]

But in reality, as the applied bias voltage increases nearing breakdown of the cell, the leakage term develops a drastic exponential relation earlier than presumed due to certain reverse phenomenon that are further elaborated in the following section 3.3.1.

[3]Leakage differs from reverse saturation current which can be much larger nearing breakdown as leakage solely depends on V and becomes significant as it approaches breakdown V_{br}.

3.3.1. Leakage current

The most widely used model for avalanche breakdown is Bishop's equation, which is a modification of the single diode model that includes an excess leakage current (I_{Leakge}) term through the shunt resistance and can be depicted as shown in Figure 3.8.

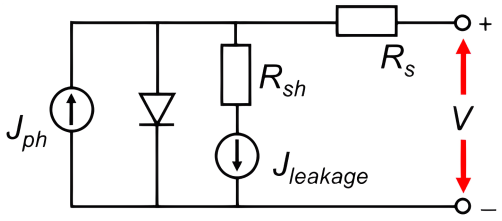

Figure 3.8: Equivalent circuit from the Bishop diode model during reverse breakdown [66]

From Equation 2.4, we observed the current flowing through the cell I denoted by:

$$I = I_{ph} - I_0 \cdot \exp\left[\frac{q(V + IR_s)}{nk_BT} - 1\right] - I_{leakage} \tag{3.7}$$

But the leakage term during the reverse breakdown conditions change depending on the type of the breakdown characteristic given by [4] :

$$I_{leakage} = \frac{V + IR_s}{R_{sh}}\left[1 + \dot{a}\left(1 - \frac{V + IR_s}{V_{br}}\right)^{-m}\right] \tag{3.8}$$

Here the additional parameters denoted are : breakdown voltage V_{br}, fraction of ohmic current involved in the leakage, $\dot{a}$ and the avalanche multiplication factor m which is discussed more in section 3.4.6.

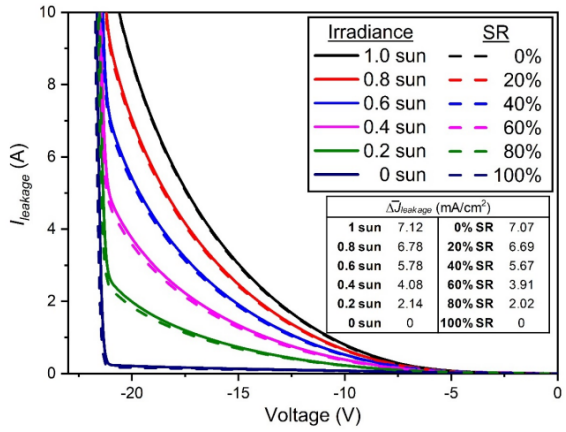

Figure 3.9: IV curves of leakage at variable irradiation and shading ratios [66]

A concept that was re-iterated from the previous section 2.6.1 also suggests the leakage current of a cell under partial shading is similar in terms of a cell experiencing low irradiance as shown in Figure 3.9. But it must be noted that not all the leakage was accounted for in the study suggesting further investigations required to correlate the relationship to account for deviations from the experimental findings.

[4]The bishop model cannot be used to predict leakage as Zener breakdown has a probability of tunneling

3.3.2. Series and Shunt resistance

The presence of series resistance (R_S) in a fully illuminated solar cell is attributed to material properties and contact resistances. This resistance contributes to an ohmic loss that intersects with the cell's IV characteristic curve, thereby defining the operating point [28]. The resulting voltage drop across the solar cell's terminals, due to R_S, influences the cell's performance within the context of its characteristic curve. Minimizing series resistance is critical for improving solar cell power output. Similarly, shunt resistance (R_{sh}) refers to the presence of shunts that allow the intended current to flow through alternate conductivity paths. It influences parasitic current distribution and cell performance, with higher (R_{sh}) restricts leakage current diversion and minimizes losses.

High-shunt resistance cells are voltage-limited, meaning that the voltage across the cell limits reverse current flow and heats the cell up, with the highest shunt resistance cell dissipating the most power. Because the heating is uniform throughout the cell, it may take longer for the cell to heat up to the point of causing damage. Meanwhile, low-shunt resistance cells are current-limited and more susceptible to hot spots as they heat up quickly. These cells allow a significant amount of reverse current to flow in small, localized areas, similar to the current observed under illumination conditions. As a result, when subjected to reverse bias, they are at a higher risk of operating at excessively high temperatures, particularly in localized areas [67].

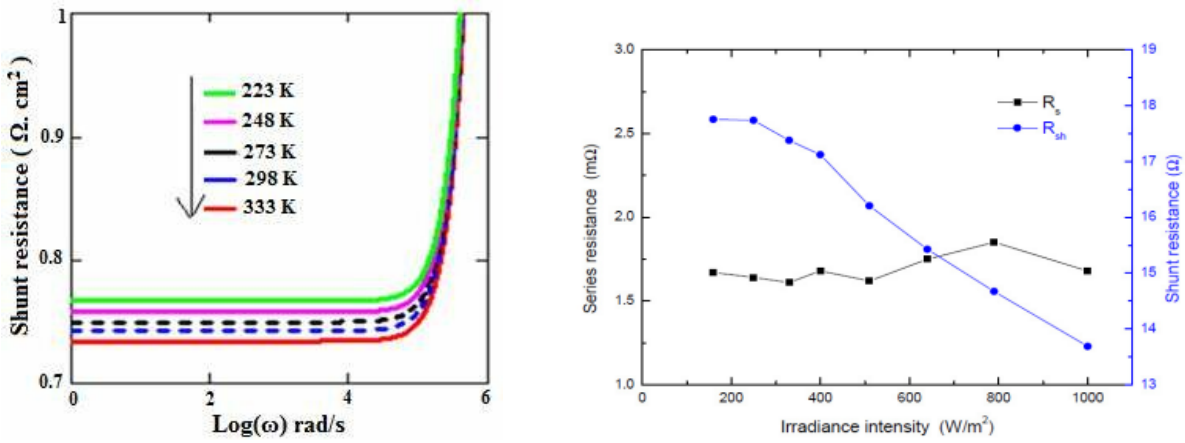

(a) (b)

Figure 3.10: (a) Shunt resistance versus the logarithm of frequency Log(ω) for different values of the temperature [68] (b) series resistance and shunt resistance as a function of irradiance [43].

As the temperature rises in Figure 3.10a, the charge carriers within the solar cell gain kinetic energy, resulting in chaotic motion and increased collisions. As carrier activity increases, leakage current increases, reducing shunt resistance. This temperature-dependent IV characteristic may lead to an even more pronounced breakdown. In contrast, the absence of photo-generated current in a shaded cell reduces the impact of R_s, making it less significant and dependent on illumination as shown in Figure 3.10b. The R_{sh} plays a more significant role by providing an alternative route through which current predominantly passes and eventually dissipates as heat.

3.3.3. Capacitance and J-V curve Hysterisis

A solar cell behaves as a capacitor, storing charge in the depletion region of a PN junction diode under various operating conditions [69]. Under forward bias, the depletion width decreases, reducing the diffusion capacitance. As the bias voltage is increased in the reverse direction, the width of the depletion region increases, causing the transition capacitance to decrease [5]. The amount of capacitance in the depletion region is dependent on the doping concentrations and applied voltage [71].

The capacitance of a solar cell can affect its ability to store charge, which is critical for maintaining a stable output voltage during IV sweeps. If the capacitance is too high, the solar cell will be slower to respond to changes in illumination or load conditions, resulting in decreased efficiency as shown in Figure 3.11. The capacitance is also affected by temperature and illumination. Because the thermal energy of the charge carriers increases at higher temperatures, the capacitance of the diode increases. Similarly, as the carrier generation rate increases, the capacitance of the diode increases [71].

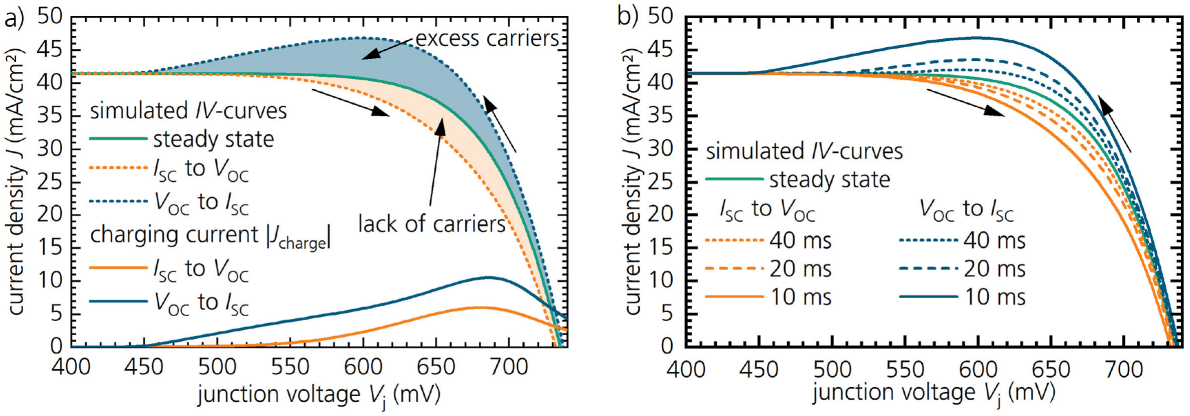

Figure 3.11: Hysteretic region in the IV-sweep highlighting (a) the role of the charge carriers and (b) the charging current [71].

The breakdown voltage is dependent on the thickness of the depletion region in the solar cell, which is directly related to the doping concentration of the material as discussed in subsection 3.3.4. At breakdown voltage, the capacitance of the solar cell can cause a phenomenon called capacitance-induced instabilities. This occurs when the capacitance of the solar cell causes charge carriers to build up near the edges of the depletion region, leading to localized regions of high electric field strength. These regions can cause the breakdown voltage to drop, leading to further current flow and potentially damaging the solar cell [72].

[5] The reverse-biased P-N junction has transition or space-charge region capacitance, while the forward-biased has diffusion capacitance [70].

3.3.4. Breakdown Voltage

Breakdown voltage (V_{br}) is the highest reverse bias voltage that a solar cell can safely apply without damaging the p-n junction. Different cell technologies exhibit a wide range of breakdowns owing to variations in their characteristics and designs. Breakdown occurs in three distinct phases [72]:

1. Initiation: The first stage begins with the emergence of a conductive channel within the dielectric material as a result of the applied electric field surpassing the dielectric strength of the material. This high electric field induces localized breakdown, leading to the formation of a conductive path.
2. Propagation: Once the conductive channel is established, stored charges within the dielectric material begins to discharge through this pathway. As charge is released, the conductivity of the channel increases, facilitating the propagation of the breakdown process.
3. Dissipation: The discharge of stored charge triggers a self-sustaining cascade effect, reducing the internal resistance of the material dramatically leading to a positive feedback loop, eventually resulting to a complete breakdown or failure of the material.

High-breakdown cells ($>$ 13 volts), such as PERC, are designed to be more resistant to breakdown and to withstand higher reverse voltages. However, due to defects, they experience significant power dissipation prior to breakdown [14]. These cells use expensive materials,but also minimize bypass diodes, and reduce complexity, costs, and additional structures to improve breakdown voltage capabilities and operate in harsh conditions [73].

Low breakdown ($<$ 6 volts), as seen in IBC cells, is desired for reliable operation as it ensures consistent and predictable performance. Since the breakdown is at a lower voltage, the power dissipation can safely be minimized [74]. However, designing low breakdown cells poses challenges in achieving desired voltage thresholds while balancing performance parameters like efficiency and size, requiring careful optimization to address these design constraints. Material properties such as doping, manufacturing processes and depositions, device design such as barrier width and layer thickness all have an effect on breakdown volatility.

Temperature Dependence

Operating conditions such as temperature have demonstrated that the breakdown voltage temperature dependence in p-n junctions can be described using the relation [75] :

$$V_{br} = V_{b0}\beta(T - T_0) \tag{3.9}$$

where V_{b0} is the breakdown voltage at ambient temperature T_0 and β is the breakdown voltage-temperature coefficient. Following the cited reference, β should be constant with a value of $8.8{*}10^{-4}/°C$ in a temperature range of 15 to 196°C for silicon. This would indicate that the breakdown can vary with a slight yet noticeable difference depending on the type of breakdown.

3.4. Breakdown

The breakdown of a p-n junction is caused either by a temperature rise (thermal breakdown) or by an electric field, which includes impact ionization (avalanche breakdown) and tunneling (zener breakdown). Thermal and electric breakdown are competing processes, with their relative importance depending on factors such as temperature and band gap energy [39]. These differ in the mechanism that initiates the process of increasing electrical conductivity, but the end result is the same: destruction by excessive joule heat dissipation.

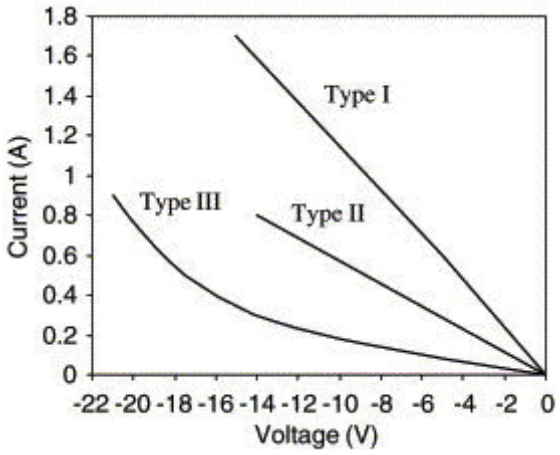

Figure 3.12: Different curves of types of breakdowns [76]

In reality, silicon solar cells have a pre-breakdown (Type-I) voltage region through which some current flows before complete breakdown and exhibit a linear (ohmic) reverse characteristic at low bias, even in the absence of ohmic shunts. When the reverse bias exceeds 10 V and beyond, the relationship becomes super-linear with a higher slope, and a significant breakdown may occur as shown in Figure 3.12.

3.4.1. Thermal Breakdown

Thermal breakdown is characterized by "thermal runaway," which occurs when the junction exceeds its maximum stable operating temperature and the semiconductor reverts to intrinsic conduction. Power dissipation in the device then increases exponentially, while heat losses to the surroundings only increase linearly with temperature over time [72]. Hence, above the maximum stable operating temperature, the device heats up rapidly until it is permanently destroyed by melting. Microscopic examinations of failed solar cells revealed that failure was caused by the formation of "point shorts," which were melted zones contaminated with metals used in cell contacts. Thermal breakdown occurs at weak spots or uniformly over the whole area of the specimen. The specimen can be made uniform with respect to breakdown by eliminating the weak spots with self-healing, non-shorting breakdowns. When a large reverse current flows through the cell, specific sections may overheat (creating hot-spots), resulting in the thermal degradation of the module [39].

3.4.2. Early Breakdown

The most common and trivial reverse current sources in solar cells are defects and shunts. The history and impact of ohmic shunts on hot-spots have been extensively studied [77], [78]. However, due to their linear increase in reverse current, localized shunts rarely result in dangerous hot-spots. Defect-induced early breakdown (Type-II), on the other hand, is more uniformly distributed across multiple breakdown sites in the cell. They can be caused by insufficient edge junction isolation, cracks, etch pits, Al contamination of the emitter, or material defect-induced failure. These defects act as charge carrier recombination centers, resulting in localized heat generation. Nevertheless, these reverse characteristics exhibit pre-breakdown processes that do not necessarily result in hot-spots unless the cell has significant ohmic shunting or a significant number of defects, which in turn reduces the shunt resistance.

3.4.3. Zener Breakdown

The Zener breakdown phenomenon occurs in a p-n junction with high doping and a thin junction (the depletion layer width is very narrow $\sim$ 100nm). At normal temperatures, electrical junction breakdown is initiated by impact ionization or tunneling [64]. When an external voltage is applied, the electric field across the junction increases, driving electrons and causing them to break free from their covalent bonds and move into the conduction band as depicted in Figure 3.13. As the bias voltage increases, more electrons are released, leading to more electron-hole recombination and a rapidly growing reverse current. The Zener breakdown voltage (V_z) depends on band-gap energy and decreases with increasing temperature. It is given by the following equation [69]:

$$V_Z = \frac{\varepsilon_0 \varepsilon_s . \xi_{cr}^2}{2e} \left(\frac{N_a + N_d}{N_a N_d} \right) \tag{3.10}$$

3.4.4. Tunneling

As the doping concentration profiles increase, narrowing the band-gap of the material, band-to-band electron tunneling [6] occurs [74]. For tunneling to become predominant, there should be a field sufficiently greater than a certain critical value ξ_{cr} in the order of 3×10^7 V/cm. Then the tunneling probability of electrons increases causing higher currents across the junction.

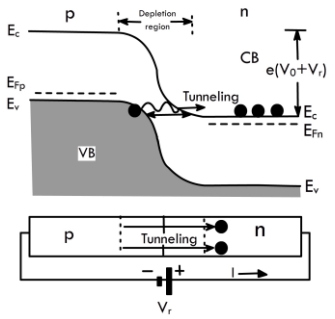

Figure 3.13: Band-to-band tunneling of electrons from valence to conduction band [79]

[6] Tunneling is a quantum mechanical process in which charge carriers tunnel through the energy band-gap of a semiconductor, even when they do not have enough energy to overcome the barrier classically.

3.4.5. Avalanche Breakdown

Avalanche breakdown (Type-III) occurs in moderately doped, thick PN junction diodes (depletion layer width is high). Avalanche breakdown takes place when a strong reverse voltage is applied across the junction, causing an exponential increase in the electric field.

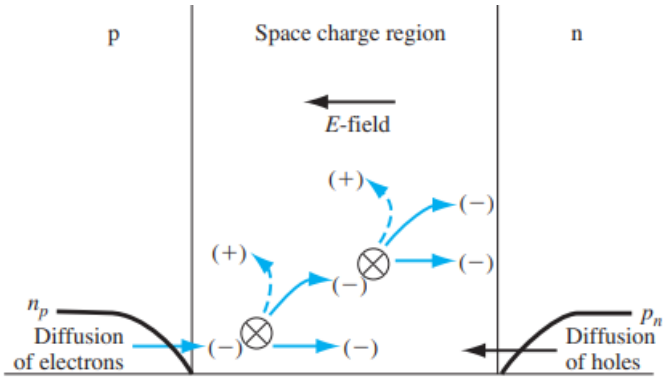

Figure 3.14: Avalanche breakdown in a P-N Junction [80]

In contrast to the zener breakdown, charge carriers driven by the electric field obtain enough energy to ionize lattice atoms, resulting in secondary charge carrier pairs in an avalanche that are accelerated to high energy levels to produce additional ionization, and so on. Depending on doping concentrations, electric field strengths in the range 0.3-0.8 V/cm are required to cause avalanche breakdown in abrupt silicon p-n junctions [39]. The avalanche breakdown voltage (V_{AB}) of an abrupt P-N junction may be then expressed emperically as follows:[7]

$$V_{\mathrm{AB}} = 60 \left(\frac{E_g}{1.1} \right)^{3/2} \cdot \left(\frac{N_I}{10^{16}} \right)^{-3/4} \tag{3.11}$$

Avalanche breakdown voltages increase with temperature, since the mean free path between scattering events decreases with increasing temperature. Higher applied voltages are therefore required to accelerate carriers to the threshold energy for further impact ionization. Avalanche currents then proceed to raise the junction temperature until the semiconductor reverts to intrinsic conduction, leading to thermal breakdown as mentioned in section 3.4.1. This temperature dependence coefficient (β) mentioned in equation 3.9 is observed to be opposite in sign to that of zener breakdown, which is a key indication used to distinguish between these two competing processes [72]. A brief overview of the characteristics of breakdown is provided in table 3.3.

IBC cells incorporate a fourth reverse breakdown mechanism through clever engineering of the cell architecture. The design consists of p+ and n+ regions fabricated to be in contact with each other to form a zener diode, which are passive devices synonymous with zener breakdowns at constant voltages. They are designed to operate in reverse bias, regulating current flow when the voltage across the cell exceeds a certain threshold (V_z) as shown below in Figure 3.15. Tunneling currents across the locally abutted p+ and n+ regions on the rear side could be a cause of the soft breakdown characteristic [74]. A brief explanation is provided in section 6.1.

[7] N_I denotes the doping concentration on the low-doped side of the P-N junction.

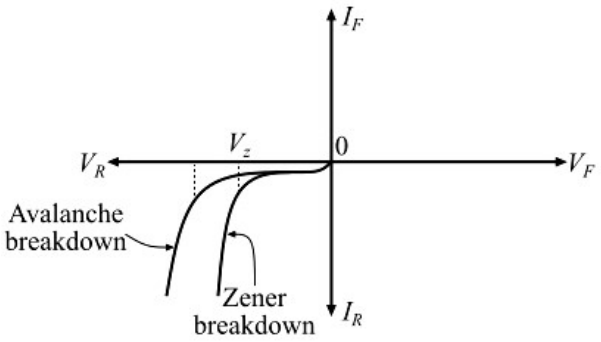

Figure 3.15: Zener and Avalanche breakdown characteristics [81]

3.4.6. Multiplicaion factor (M)

The Miller's coefficient in avalanche multiplication is a parameter that quantifies the extent to which the impact ionization of initial numbers of electrons leads to a cascade of additional electron generation [65]. This phenomenon of multiplication is depicted in the Figure 3.14. The formula for breakdown can be expressed in terms of multiplication factor, M given by :

$$|M(V)| = \left| \frac{1}{1 - (\frac{V}{V_{Br}})^n} \right| \tag{3.12}$$

Where $2 < M < 6$ and the breakdown criteria is $V \to V_{Br}$ and $M \to \infty$. In this context, when the applied voltage approaches the cell breakdown threshold, the multiplication of charge carriers amplifies significantly, causing an avalanche that ultimately leads to the breakdown.

Table 3.3: Overview of criteria for distinguishing between Zener and Avalanche Breakdown [81]

Parameters	Zener Breakdown	Avalanche Breakdown
Reverse breakdown voltage (V_{br})	5 to 8 volts.	Greater than 8 volts
Depletion region width	Thin	Thick
Destruction of junction	Temporary	Permanent
Electric field	Strong	Relatively weak
Doping level	Heavily doped	Any level of doping
Multiplication Factor (M)	$\|M\| > 1$	$\|M\| = \infty$
Relation between (V_{br}) vs T	Inversely proportional	Directly proportional
Change in voltage after breakdown	Constant	May vary after breakdown
Temperature coefficient of voltage (β)	Negative	Positive
Charge carrier generation	Electrons	Electron-hole pairs
Effect on junction	Regains original state	Does not regain original state

The breakdown characteristics will provide insights into the hot-spot testing and guide experimental design, identifying which breakdown phenomena occurs in the sample of cell technologies and qualitatively assessing the nature of the phenomenon.

4 Methodology

The subsequent sections of this chapter present a comprehensive outline of the methodology employed in the research study. The experimental techniques, inspection criteria, and data collection procedures are elaborated upon in section 4.1, highlighting existing methodologies and standards employed in the study of hot-spots in section 4.2, respectively. The formulation of a robust design criteria for polymer-based lightweight modules, which is one of the main objectives presented in section 4.3. Finally, the chapter ends with a discussion on the validation of the methodology in section 4.4, acknowledging any limitations encountered during the research.

4.1. Experimental Techniques and Data Collection

The methodology combines quantitative characterizations with qualitative inspections, as mentioned in sections 5.2 and 5.3. Experiments in this thesis are specifically designed to investigate the effects of temperature, illumination, and shading rate on the breakdown characteristics. The process is as follows:

1. Quantitative analysis is performed by correlating measured IV curve data with observed hot-spot characteristics mentioned in section 3.2. This can also be used to make assumptions and explain observed trends and behaviors in results.
2. Combining qualitative and quantitative data for comprehensive interpretation of results.
3. Comparing experimental results with literature to assess breakdown characteristics and validity.
4. Summarize key findings for designing hot-spot endurance tests and establishing a safety threshold in module configuration.

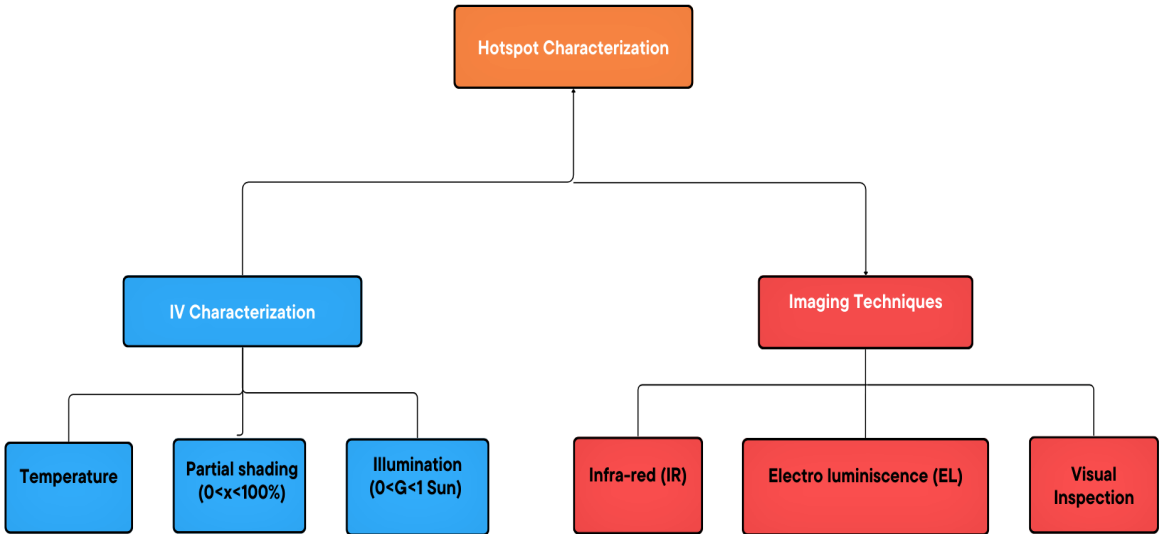

Figure 4.1: Flow chart of methodology

During the experimental phase of hot-spot testing and characterization, a variety of current cell technologies with various wafer shapes and sizes, busbar configurations, and layouts were investigated for Solarge. This was critical in the investigation of hot-spot effects in order to provide a general understanding because the findings would be most impactful when independent of cell size for the same technology. A summary is provided in table 3.1. The testing with various samples of solar cell technologies and configurations, the timeline of the thesis is divided into 3 distinct phases namely:

- Phase - 01: Testing of single-cell Laminates
  This phase investigates cell laminate properties and behavior under various illumination, temperature, and shading conditions. IV sweeps ranging from V_{oc} to V_{br} reveal breakdown characteristics, providing valuable reference for future hot-spot tests, providing accurate values for when, how, and under what conditions breakdown occurs, and determining the safety limit that can be used to design guidelines.
- Phase - 02: Testing of string of cells without bypass diodes
  This phase focuses on incorporating phase-01 findings and conducting research into string performance and safety. String topology and connection architecture, organized in series of laminated cell samples, each play a role in hot-spot testing. However, the goal of this testing is to rank cells according to their leakage and identify any defective cells.
- Phase - 03: Testing of Modules
  It is the final experimentation phase at the module level, carried out in accordance with the standard guidelines. To assess the impact and damage caused by hot-spots, as well as to determine whether the predictions and insights from phases 01 and 2 were valid and coherent. The intended outcome is to pass the hot-spot endurance certification test.

4.2. Hot-spot IEC 61215 Test

The design of a PV module or system is intended to provide safe conversion of solar energy into useful electricity and must take into consideration the possibility of partial shadowing of the module(s) during operation. Hence, this test describes a procedure for verifying that the design criteria and construction of the module provide adequate safety protection against the potential harmful effects of hot-spots during normal use and installation.

As explained in section 3.3.2, there are two types of cells: high and low shunt resistance cells. These classifications in order of leakage provide an overview of which cells to test for hot-spot endurance. Typically, low shunt resistance cells are more likely to heat up quickly due to localized heating caused by higher leakage currents.

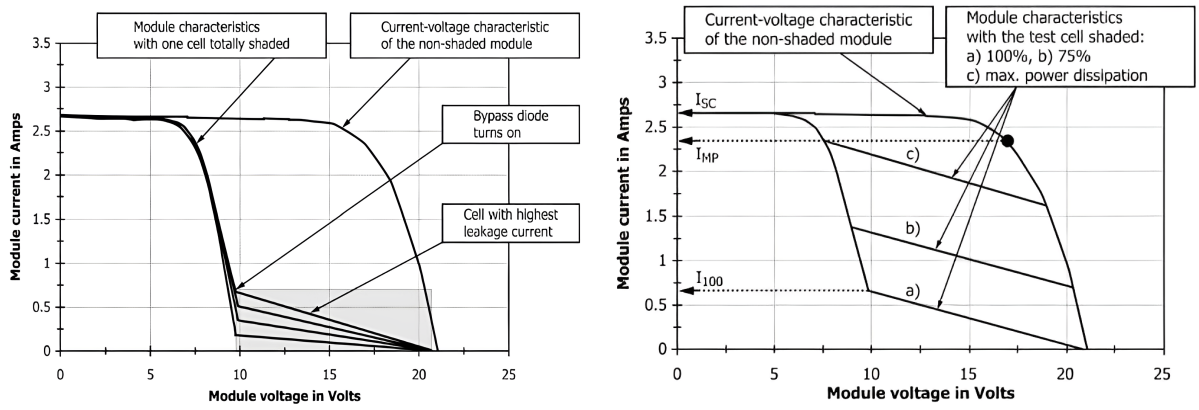

(a) (b)

Figure 4.2: (a) Module I-V characteristics with different cells completely shadowed (b) The test cell is shadowed at different ratios [82].

The module IV characteristic is measured without shading at STC for reference and then with shading for comparison. More details on the experimental setup used for hot-spot endurance testing is provided in chapter 5. The methodology has been slightly updated based on recent versions of the IEC standard [83], but the procedure remains the same as follows:

4.2.1. Selecting the defect cells

a.) Expose the un-shaded module to source at 800 - 1000 W/m^2. This can be done using a pulsed simulator where the module temperature will be close to room temperature (25 $\pm$ 5)°C.

- Before measurements may begin, the temperature of the module in the steady-state simulator must settle.
- After thermal stabilisation is attained, measure the module I-V characteristic and determine the maximum power and current (initial performance) P_{max} and I_{max}. Correction to the value to STC after is not necessary.

b.) Shadow each cell completely in turn, measure the resultant I-V curve and prepare a set of curves like figure 4.2a.

c.) Select the three highest and lowest shunt resistance cells respectively.

4.2.2. Setting the worst-case shading scenario

d.) Shade each of the selected test cells in turn with 5%, 10% ... 25% (increment in steps of 5%) and measure I-V curves. Shadow each of the test cells and determine what shadow level results in the current through the shadowed cell being equal to the un-shaded I_m. This is the worst-case shadowing for that cell as shown in figure 4.2b.

4.2.3. Endurance Testing

e.) For selection of the defect cell, use the IR camera to determine the hottest spot on the cell when it is shaded 100% individually in step b). For a precise selection, shadow that cell on the exact location where the hot-spot on the chosen cell was observed to the worst case condition as determined by the shading ratio (x%) as determined in step d).

f.) Ensure the module is short-circuited and expose the module in the steady-state simulator to (1000 ± 100) W/m^2 illumination. Thermocouples should be pasted to the cell's selected hot-spot in both shaded and unshaded regions to monitor the highest temperature in comparison to the original. This test shall be performed at a stabilized module temperature in the range of (50 ± 10)°C.

4.2.4. Exposure

g.) Maintain the worst case shading condition determined in step e) when using the steady-state simulator, and take the module out for a minimum of 1 h for every 5 h of exposure.

4.2.5. Diagnostics

h.) Perform an electrical IV characterization on the module.

i.) Perform a visual inspection practice to check for hot-spots.

j.) Check the hottest cell and record the highest hot-spot temperature among the selected cells.

4.2.6. Report

The report shall include the following items as a specified :

1. Module manufacturer and complete test specimen identification.
2. Description of electrical measurement equipment.
3. Module I-V measurement results before and after the hot-spot exposure.
4. Ambient conditions during the test.
5. Measured values of module current and temperature.
6. A description of any noticeable changes as a result of the testing. Identification of affected areas, such as shorting, arcing, excessive heating, damage to module materials, or other failures that allow access to live parts.
7. Any deviations from the test procedure.

4.3. Development of design criteria of PV modules

Cell manufacturers lack information on the behavior of their cells under reverse-biased conditions exceeding -10V, making it important to gain insights into the characteristics of hot-spots and the reverse IV behavior of the cells, particularly in the dark. This will help to assess cell performance and the potential risks associated with reverse-biased operations [83]. Hence, it is necessary to establish a design criterion that considers the module's reverse characteristics.

4.3.1. Identifying the worst performing cell

The notion of eliminating environmental stress to identify the lowest-performing cell purely based on lower electrical performance, hinting towards material properties, offers an intriguing perspective. However, quantifying this through techniques like EL and IV characterization faces challenges due to defects and shunts. Instrument sensitivity can play a role in minor voltage fluctuations. Yet, it's crucial to highlight that finding a highly defective cell with a significant measurable voltage drop in a casual inspection of a PV module is improbable. It introduces intricacies into the ongoing discussion about whether identifying the lowest-performing cell in the module truly leads to the highest temperature or if, due to constantly changing environmental conditions and cell material properties, the endurance test can fairly be conducted at random. Validation of this methodology of identifying the worst cells is described in section 4.4.

4.3.2. Worst case shading scenario

Solar cell design significantly impacts shading susceptibility, with busbar configuration and interconnection methods being crucial factors. Optimizing busbar arrangement ensures uniform current distribution and minimizes shading losses. Although larger cell dimensions pose higher risks and complexities as discussed in section 3.1, but self-shading losses from metallization are typically negligible both in front and rear. In practice, the worst-case shading scenario occurs when a significant portion of the solar cell is shaded, resulting in non-uniform power dissipation. This causes localized current concentrations to deviate, resulting in the previously mentioned non-linearity between $\dot{Q}$ and shading rate in section 3.2.1. Most full-cells report a worst-case shading percentage between 10-20%, with some reporting an even narrower range of 15–18% observed [84]. Similarly half-cut cells report a worst shading ratio between 30-40%. But this holds true only when there are bypass diodes attached to the string and they turn on at this point, as shown previously in figure 4.2a. Meaning that a different bypass diode configuration can result in a different worst-case shading scenario independently of cell dissipation.

4.3.3. Hot-spot Temperature (T)

The heat transfer in the shaded module is directly proportional to reverse current flow, resulting in a higher dark-reverse current density. In order to determine the thermal design limit, it is imperative to establish a guideline that accounts for the properties of the polymer materials used in module construction and their limited heat dissipation capabilities. It is recommended to adhere to a maximum temperature threshold of 160°C to mitigate the risk of de-lamination. Exceeding this threshold would render the module inoperable in the long run.

4.3.4. Power dissipation (P)

According to [84], non-uniform power dissipation above 100 watts can cause localized heating and thermal imbalances, increasing the risk of exceeding hot-spot temperature limits or initiating a complete cell breakdown.

4.3.5. String Length (S)

Common string lengths of 12 cells often record temperatures of 100 °C, but this is a conservative estimate from simulations that do not account for ambient heat sources (P_{illum}) during operation. Further, the string length of a PERC module already approaches the design safety limit with a 24 cell configuration or more in series [85]–[87]. The product of the reverse current, voltage drop across the cell and the string length determine the power dissipation. As a result, the string length restricts the voltage range under standard illumination to avoid dangerous breakdown. The maximum reverse bias that can safely be applied to a single solar cell in a module of S cells in series while still having bypass diodes is given by :

$$S_{string,max} = \left[\frac{V_{br} - V_{to}}{V_{oc}} + 1\right] \tag{4.1}$$

Where V_{to} is the bypass diode turn-on voltage, which is typically 0.6 V for a normal Schottky diode. To put it simply, reducing the number of cells in the string can ensure that V_{rev} has a smaller magnitude than the breakdown voltage of the individual cell for safe operation [88].

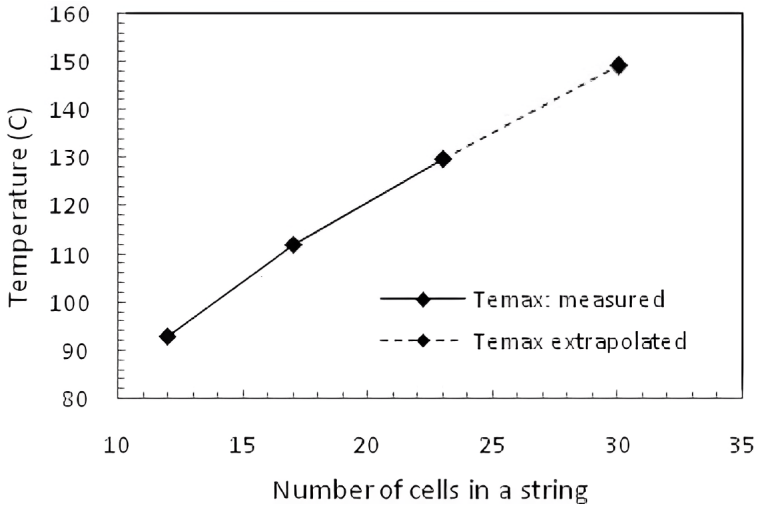

Figure 4.3: String length vs hot-spot temperature plot [85]

It is important to note that certain defects may induce or trigger an early breakdown across various breakdown voltages for different cell technologies. Especially when low V_{br} cells are barely shaded, the drop in cell voltage may not be enough to activate the bypass diode V_{to}, and the cell starts to passively operate in the pre-breakdown region carrying the entire module's current. The pre-breakdown region may cause partial current flow through the shaded cells, as the bypass diode handles the remaining current. This causes moderate heating in both the shaded cell and the bypass diode, which, if left unnoticed, can degrade the module components over time.

Moreover, low V_{br} cells claim to be inherently safe due to their self-bypassing nature, which reduces the risk of excessive current flow [54]. High V_{br} cells, on the other hand, still necessitate the use of bypass diodes in the string, with some approaches recommending one for every 1 or 2 cells to reduce power loss and increase overall system costs [89].

4.4. Validation and limitations

The current hot-spot standards described in the previous section 4.2 assume cell homogeneity and uniform performance within a PV module but do not account for variations in the batch of cells during manufacturing or the possibility that these samples of selected cells do not represent the worst-performing cells. To address this limitation, another approach is to consider performance variation and incorporate parameters unique to each cell, such as voltage drop and shunt resistance. This method tries to ensures that the worst-performing cells are accurately identified for hot-spot analysis and systemically ranked to predict which cells will become hot in which order.

The module must be subjected to STC in order to identify and rank hot-spot susceptible cells based on voltage drop analysis. By fully shading each cell individually, a distinct voltage drop is created for each cell, providing insight into its leakage and reverse characteristics. Because each cell's voltage is individually added in series as mentioned in section 2.4, finding the cell with the highest voltage drop in open circuit compared to the full module or the un-shaded string would provide a relative ranking of which cells are likely to dissipate heat quickly when operating in reverse bias.

4.4.1. Voltage drop method

Identifying the cells with the highest and lowest shunt resistances and quantifying shadowing effects are important during hot-spot testing . While certain methods exist for modules with removable bypass diodes or accessible electrical circuits to measure through IV curves as described in section 4.2.1, a non-intrusive approach is required for PV modules lacking these features.

$$\Delta V_{drop} = V_m - V_{sh} \tag{4.2}$$

By utilizing high-precision voltmeters and infrared cameras, we can accurately measure the voltage drop of shaded cells and observe potential hot-spots without disturbing the module's existing configuration [1][90].

- Hot-spot Index (HSI) : Rank the cells in the order of the index, with defect cells ranking high and ideal cells ranking low.
- Emperical Validation : Conduct empirical validation to establish a quantitative relationship between the HSI and temperature increases. This involves experimental testing to confirm the correlation between HSI values and actual hot-spot occurrences.

[1] In this case, there is no direct access to individual cells in the string rather the entire string itself.

5 Experimental setup

This chapter outlines the experimental setup used for testing, beginning by detailing the specific cell technologies including technical specifications in section 5.1. IV characterization is then explained for cell and module performance assessment in dark and illuminated conditions in section 5.2. Imaging techniques, particularly EL & IR imaging for hot-spot analysis,along with visual inspection methods are discussed in section 5.3. The partial shading technique is introduced as a methodology in section 5.4, emphasizing on material selection. Finally, the chapter concludes with hot-spot endurance test setup explained in section 5.5.

5.1. Pre-characterization

Solarge's preference for the larger PERC M-10 cells over the standard G1 cells meant that only five of the initial eight cell configurations could be chosen for pre-characterization mentioned in table 3.1. Since the focus of this thesis does not include investigating the correlation between cell size, metallization, and hot-spots, it was decided to avoid the repetition of experiments for various industry wafer sizes, especially when dealing with the same cell technology (PERC) and only minor differences [1] in cell dimensions and number of busbars. Although there have been varying observations regarding hot-spot characteristics while using half-cut cells of the same technology, making it worthwhile to investigate further. IBC cells, on the other hand, present a challenge when it comes to manually soldering the intricate interdigitated design. As a result, pre-soldered samples were chosen from a batch provided by the manufacturer, and the contacts were then connected to a metal busbar on both sides before the sample was laminated at Solarge and then brought to TU Delft for phase-01 & 2 characterization.

Table 5.1: Summary of characteristics of cell technologies measured at STC

Cell Technology	I_{sc} (amps)	V_{oc}(volts)	Area (cm^2)	V_{br}(volts)
PERC G1 - Full cell	10.14	0.678	250	-20.4
PERC M-10 Full cell	13.4	0.691	330	-19.6
PERC G-1 Half-cell	5.2	0.65	125	-20.3
PERC M-10 Half-cell	5.7	0.685	165	-19.8
6 INCH IBC Full-cell	6.11	0.713	150	-5.6
M-6 IBC Half-cell	5.8	0.7	135	-5.6

[1] PERC M-10 & IBC Half-cut cells have a bi-faciality design.

5.2. IV characterization

The Enlitech steady-state simulator at the Esp lab, TU Delft was used for the entirety of phase-01 characterization because none of the module IV flash testers were built to handle single-cell sweeps. The equipment used in the characterization is mentioned in table 5.2.

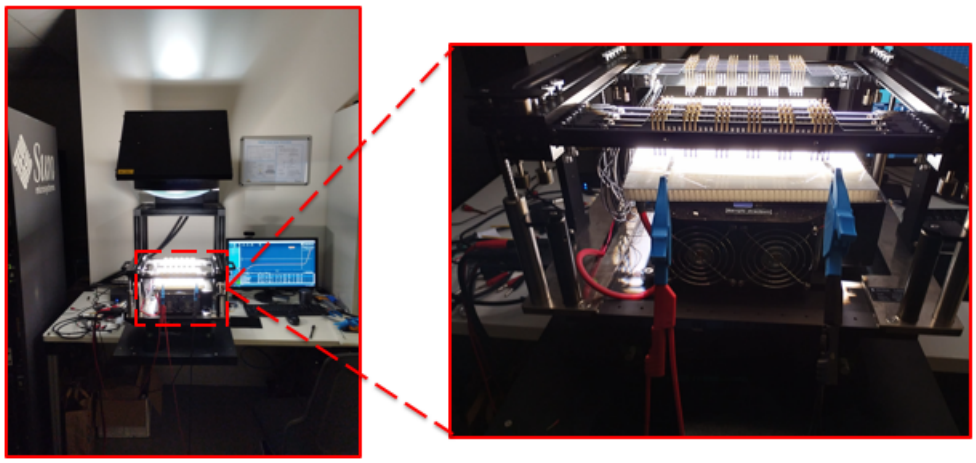

Figure 5.1: Enlitech solar simulator (left) along with the cell (enlarged image on the right),TU Delft

Table 5.2: Overview of set-up parameters

Equipment	Specification
Solar simulator	Enlitech SS-X220R_V1.00
Measurement	4-point sensitivity resistance probes
lamp source	Xenon-Halogen Arc
Illumination	1000 W/m^2 steady source
Temperature control by fan	Not valid as laminated cell is not in contact with chuck
Scanning Measurement Device	Keithley Model 2651a

Figure 5.2: Keithley SMU Model 2651A [91].

The Keithley SMU model 2651a was used in this setup as it is designed to be flexible and characterized in high-power electronic applications, along with having a wide measurement range. The sweep range is an important parameter that was manually tuned because most SMUs are not specifically used for reverse sweeping [2]. However, to successfully complete a breakdown sweep within the range of the SMU's safe operation posed a limitation to overcome in the initial stages of phase-01. Further details are discussed about the sweep range in Appendix B.1.

[2]Sweep starts from V_{br} to V_{oc} reducing temperature effects on the IV curve mentioned in table 5.2

5.2.1. Dark

In the absence of light, testing was done to characterize the leakage among cells for phase-02 in the EL chamber mentioned in section 5.3.3. Alternatively, cells were either completely shadowed or covered to eliminate photo-generated currents, as understanding only dark reverse characteristics is crucial for predicting leakage among a string of cells and identifying which cell in a series string would be likely to hot-spot first.

5.2.2. Outdoor IV

To mimic real-life situations, measurements were taken outdoors under ambient light and temperature conditions. This outdoor set-up was particularly convenient for the phase-03 pre-characterization of modules, as the setup in Solarge was not suitable for the voltage drop method mentioned in section 4.4.1. Yet the ever-changing weather posed difficulties, making it a challenge to wait for stable conditions. As a result, the values were relative measurements and not entirely accurate or valid, as they depended on the conditions from moment to moment.

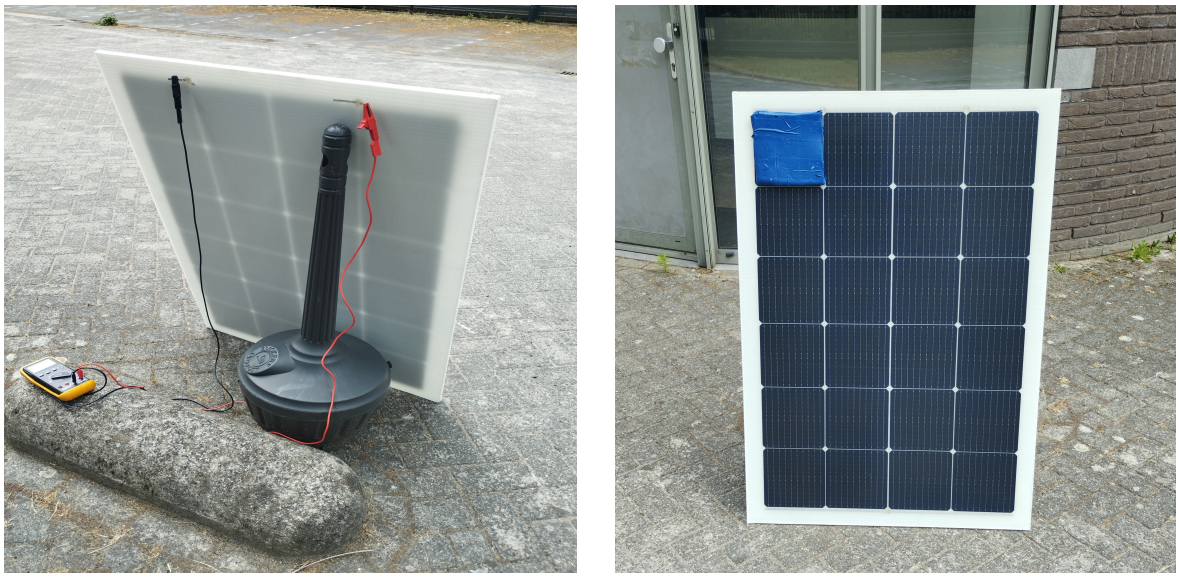

(a) (b)

Figure 5.3: (a) Multi-meter to measure voltage drop in open-circuit condition (b) Outdoor shading set-up

The rationale behind this approach is to identify highly defective cells with non-homogeneity in a batch by trying to eliminate external influences as much as possible. This enables the detection of cells with higher voltage drops, which may indicate defects or shunts that cause leakage. A comparison with EL images of the module can reveal whether or not predicted cells have defects. Furthermore, the instrument's sensitivity and ambient conditions may influence the ranking of cells based on their relative voltage drop in the string. Specifically, the cell's bifacial characteristic posed challenges in reducing the photo-current to zero, even with complete shading at the front surface and the sides as well. With sunlight entering in from the back, it was clear that the voltage drop of completely shaded cells was actually partially shaded and therefore could not be compared.

5.3. Imaging techniques

IEC standards recognize imaging techniques as an effective tool for detecting electrical and thermal failures. These techniques provide a quick and non-intrusive evaluation of module health and integrity with outdoor compatibility. They capture and visualize key parameters, enabling qualitative analysis of hot-spot detection and identifying degradation [92].

5.3.1. Visual inspection

Visual inspection plays a crucial role in the detection of hot-spots within modules by providing a simple, non-intrusive technique for identification of visual anomalies on module surfaces. One significant advantage is the ability to provide real-time qualitative information about the presence and severity of hot-spots.

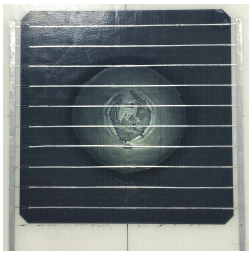

Figure 5.4: Visible hot-spot mark - discoloration, de-lamination from indoor endurance testing

Not all hot-spots are noticeable through visual inspection alone, limiting its effectiveness. Furthermore, hot-spots buried deep within the module or occurring in areas with limited surface accessibility may go undetected. Despite these limitations, the standards establish the widespread acceptance and adoption of visual inspection as a hot-spot identification criterion due to its practicality [93].

5.3.2. IR imaging

IR imaging can capture and visualize quantitative, 2-D spatial, high-resolution thermal data, enabling precise hot-spot identification, heat pattern, location, size, and detailed contour profiles. The FLIR C3-X camera has a wide range of thermal imaging modes, catering to different sensitivity levels for ambient emissivity finely tuned to a specific temperature limit constrained at 160°C. It provides accuracy within this range, ensuring reliability. With the addition of software tools and remote monitoring, IR imaging has become the most recommended practice for characterizing hot-spots. This method has limitations in using IR imaging as a tool, such as its inability to detect sub-surface hot-spots [65].

Figure 5.5: Flir C3-X camera used for IR imaging [94]

5.3.3. EL imaging

Electro-luminescence (EL) imaging is a diagnostic technique that uses the radiative inter-band recombination of excited charge carriers under forward bias to identify and characterize areas of extrinsic defects induced during manufacturing. The intensity of the EL signal is related to the material properties, such as the surface recombination velocity. Recombination in indirect band gap materials, such as silicon, predominantly occurs through a phonon-assisted mechanism as depicted in figure 5.6. This recombination is vital for EL characterization, which involves utilizing an excitation current to capture images of the emitted photons with a high-spatial-resolution camera [95].

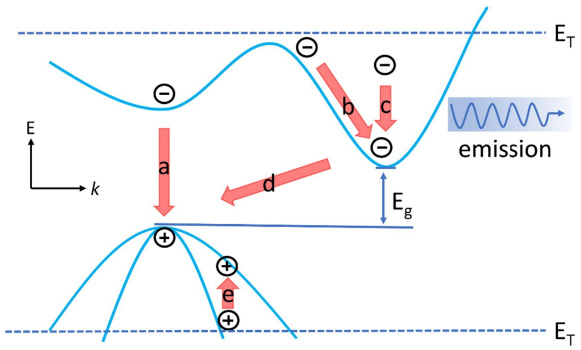

Figure 5.6: The schematic is the energy band structure for silicon. Arrows a and d represent phonon-assisted inter-band recombination, which can only occur at energies above the ionization threshold (E_T). Arrows b, c, and e represent the processes of indirect intra-band transitions below 2.3eV [96].

The camera used for this setup is the Nikon D7200 as shown in figure 5.8. To avoid interference, lenses must be free of absorption filters or coatings that reduce near-IR wavelengths near the band-gap of the semiconductor material. Long-pass IR filters are useful for imaging near band-edge EL in silicon because they block out unnecessary background noise ranging from 850 - 950 nm, some crystalline materials having emission peaks at 1150 nm, as shown in figure 5.7b. To capture high-resolution images of the PV module, the camera must be sensitive to this range, fixed at a predetermined distance, and mounted in a stable position in a completely dark environment for a long enough exposure (15-30 seconds), as illustrated in figure 5.7a.

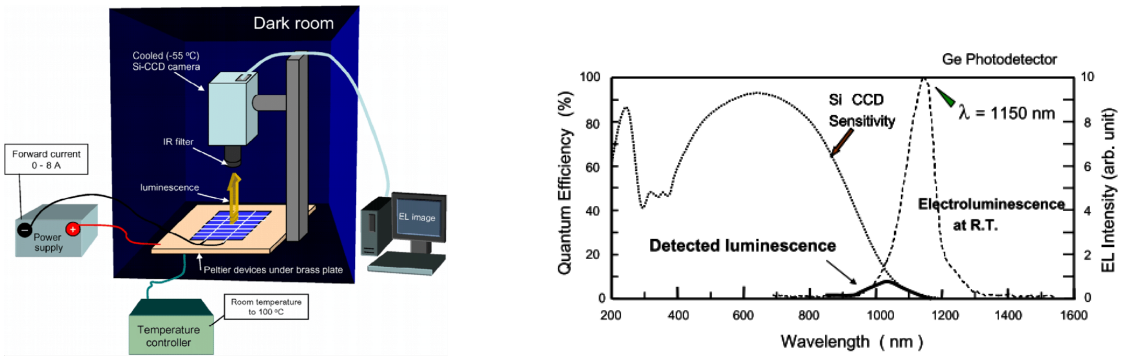

(a) (b)

Figure 5.7: (a) Schematic of the EL test setup (b) Typical emission spectrum and the sensitivity of the Si-CCD camera [97].

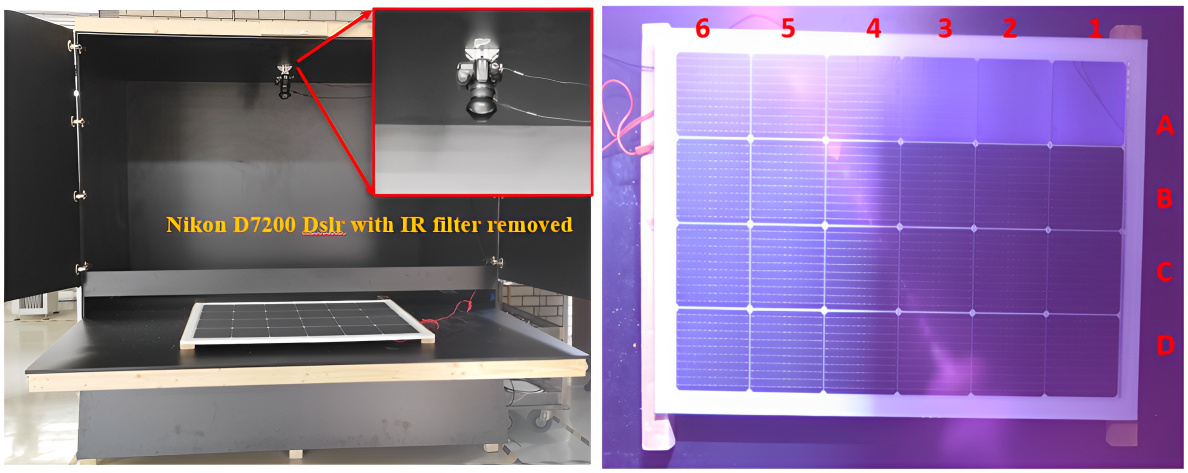

(a) (b)

Figure 5.8: (a) EL Dark chamber set-up with Nikon D-7200 camera mounted on top without IR filter (b) Orientation of the module from the camera perspective. The above image is a hybrid representation of an EL image with visible wavelength, created by opening the dark room chamber door before the timed shutter exposure (30 seconds). It demonstrates the camera's ability to pick up visible and IR wavelengths, as shown in cell (A1) on the top right corner with a defect.

5.4. Partial shading

When completely shading a cell, a general rule of thumb is to shade 5% more area than necessary to prevent diffuse irradiance from entering in from the sides. The material used to shade must also be carefully considered in terms of opacity, as the results are sensitive to variations in illumination that can cause bias in the experiments. The purpose of shading indoors is to make the cell area smaller and reduce the amount of light received. The only drawback with this setup is that when the light source is not perpendicular, it can create shadows on nearby cells, blocking the incident light. Moreover, the covering material reflects light and traps heat, insulating the shaded portion of the cell from receiving P_{illum} power from the light source.

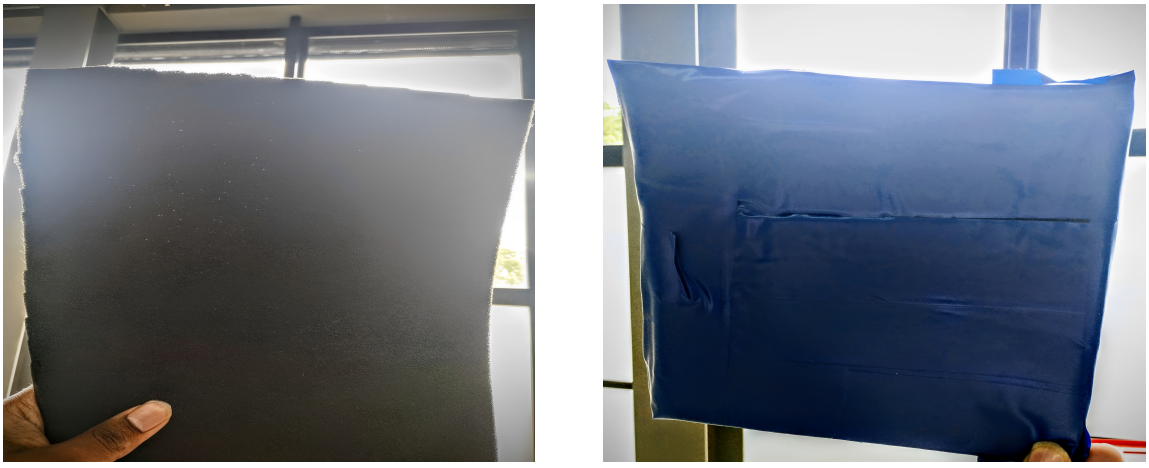

(a) (b)

Figure 5.9: (a) The shading setup is not opaque because it has holes that let sunlight through. (b) The shading is covered with tape all around, and this tape helps attach the cover on top of the shaded cell using double-sided tape without causing any damage to the front surface.

5.5. Hot-spot test set-up

This setup was used for phase-03 characterization as it is a prototype designed and modified by TNO,Solliance. The data specifications of the set-up shown in Figure 5.10 are confidential. The IV tracer set-up could not produce the required curves as shown in Figure 4.2b due to device limitations, hence multimeter had to be used to manually take data during the experiment. The objective is to clearly see whether Solarge's PV modules would actually pass the Hot-spot endurance test. Intended outcomes include certain key parameters to establish the design criteria, such as String Length (N), Maximum Hot-spot temperature (T), heat flux $\dot{Q}$ (W/m^2) and finding the lowest-performing cell.

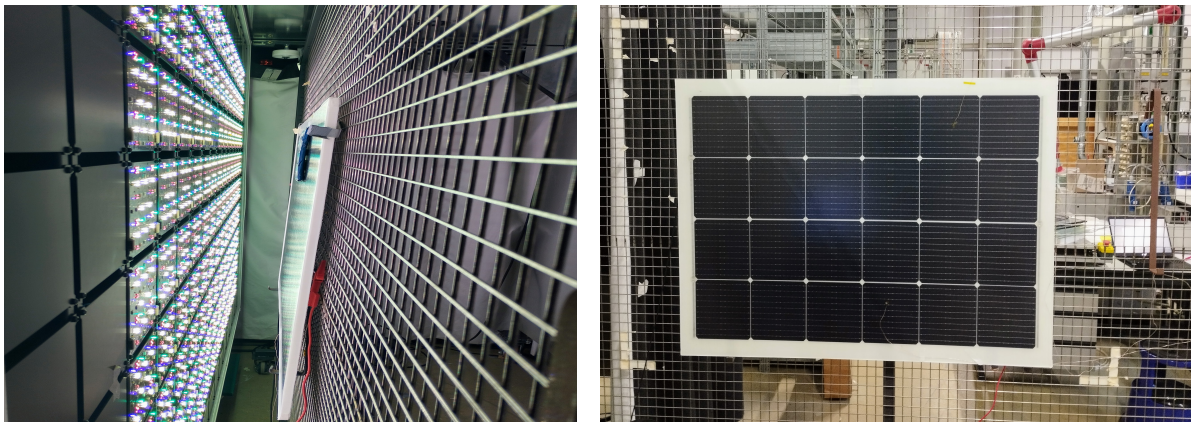

(a) (b)

Figure 5.10: (a) Module facing the eternal sun spire vertical steady state LED bulb solar simulator (side-view) (b) Orientation of module (top-view)

(a) (b)

Figure 5.11: (a) Digital Industrial Multimeter [98] (b) Thermocouple attached to a data logger that records temperature in real time [99].

Table 5.3: Overview of set-up parameters

Equipment	Specification
Solar simulator	Vertical Steady-state
Measurement	4-point sensitivity resistance probes
lamp source	LEB bulb
Illumination	970 W/m^2 steady source
Temperature control by fan	Ambient
Scanning Measurement Device	Digital Multimeter

6 Results

This chapter aims to provide a detailed analysis of the findings from this comprehensive study. Section 6.1 opens with an overview of all the results from the bulk of experimental phase-01. Following that, section 6.2 shows the comparison of the hot-spots observed between the different types of cells. Section 6.3 explains the observed pattern of hot-spots and their distinct characteristics at the string level of phase-02, while section 6.4 wraps up with the results of the hot-spot endurance test carried out according to IEC 61215 standards in phase-03.

6.1. Phase- 01

Understanding single-cell laminants under varying illumination, temperature, and shading reveals individual safety limits for cell types. IV characterization identifies breakdown limits in cell types due to unique characteristics such as busbar number, bi-faciality, current flow, carrier collection, and contact positioning, which affect hot-spots and safety concerns. These results are intended to serve as a reference when multiple cells or strings are chosen for hot-spot testing.

6.1.1. IBC Half-cut cells

As mentioned in section 3.1.2, half-cut cells carry half the rated current of a full cell. Hence, the sweep parameters were adjusted accordingly not to damage the cell by injecting high currents that the cell cannot handle, which, when exceeded, essentially turns into power dissipation in reverse, which is not advisable. The sweep parameters of the cell are provided in the table 6.1.

Table 6.1: (a) Conditions of the full-sweep of IBC Half-cells and (b) Temperature values of IV sweeps

Sweep Parameters	Values
Cell Area (cm^2)	138
Sweep Range (V)	{-5.6,0.7}
Step (V)	0.23
Delay (ms)	150
Sweep time (s)	20
Temperature (°C)	24.92

Sweep	Temperature (°C)
1	30-37
2	37-43
3	43-47
4	47-50
5	50-54
6	54-57
7	57-60
8	60-63
9	63-66
10	66-70

It can be observed in Figure 6.1, the intensity of the incident illumination is directly proportional to the photo-generated current of the cell. The measured current increases uniformly as the cell is subjected to varying illumination from $(0-1)$ sun in increments of 0.1 sun. The influence of R_{sh} is evident in dark conditions, while R_S dominates under illumination, leading to increased power dissipation shown in Figure 6.1b. Here, the worst shading condition is where the cell faces 1 sun illumination and operates in the high reverse bias. However, real-world scenarios involve partial shading, and this scenario appears unrealistic, where $\dot{Q}(W/m^2)$ depends on the shading rate (x) and the effective un-shaded area exposed to lower light conditions.

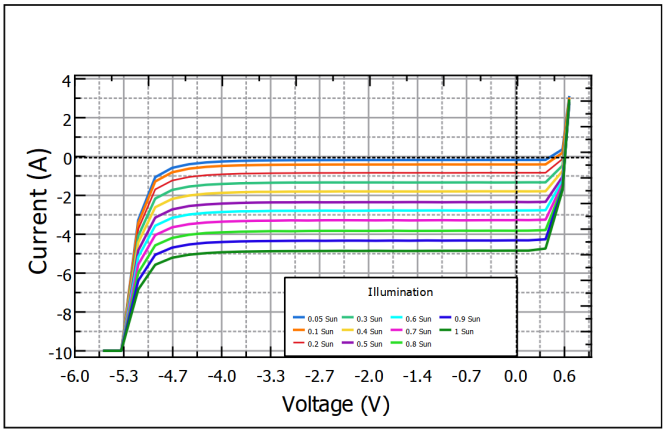

(a)

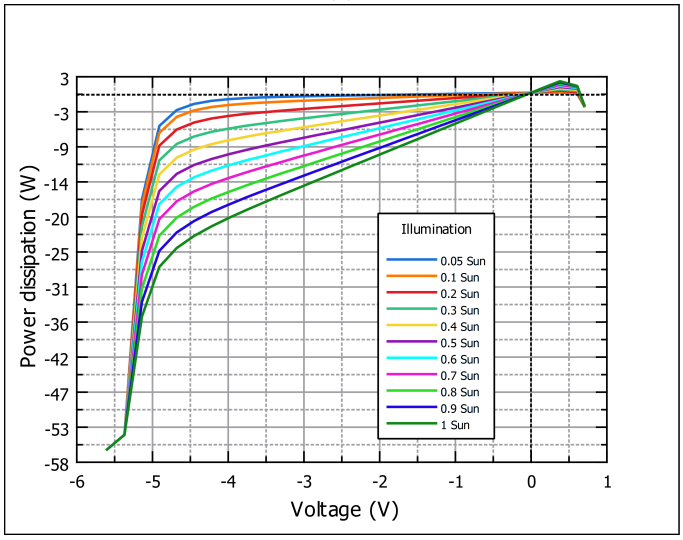

(b)

Figure 6.1: (a) IV curve of the IBC half-cut cell under varying illumination, demonstrating a soft breakdown at (V_Z) = -5.2V (b) The P-V curve of the cell during the sweep shows that power dissipation is much higher under illumination conditions, reaching a maximum of 56 W.

According to the theory discussed in section 2.6.1, breakdown should occur earlier under illumination than in the dark. However, the zener breakdown voltage (V_Z) shows little variation. Further examination reveals that the IBC cell's breakdown voltage remains independent of illumination. This feature is a deliberate design choice to ensure the cell's breakdown occurs at low voltages, reducing the risk of high power dissipation [74].

As a result, IBC cell operate differently in reverse from conventional PERC cells, where internal field emissions arise predominantly from band-to-band tunneling of charge carriers as detailed in section 3.4.4. Furthermore, IBC cells also exhibit a more controlled and predictable behavior, characterized by a soft breakdown mechanism, in contrast to the conventional carrier multiplication (hard breakdown) observed in PERC cells. This inherent behavior makes IBC cells less susceptible to changes in light exposure, reducing the likelihood of thermalization due to recombination. In simpler terms, IBC cells have a stable breakdown that is not easily influenced by varying light intensities, enhancing their resilience to shading.

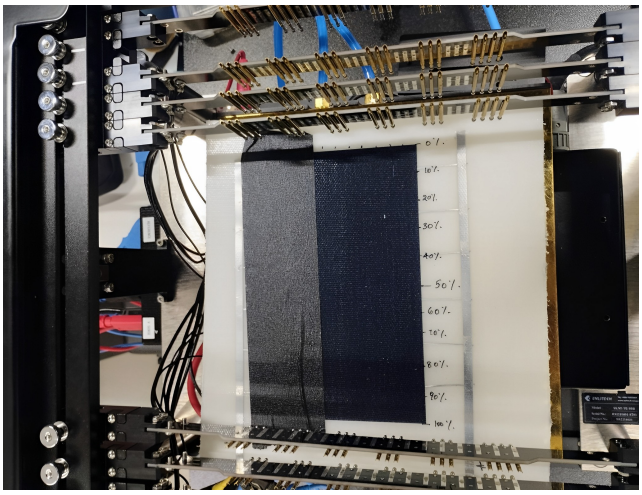

Figure 6.2: Shading set-up of IBC Half-cut cell using non-conductive black tape

Both full and half-cut IBC cells have their metal contacts on the backside of the cell design, while the front surface is completely dedicated to light absorption. When shading occurs, the orientation of the shading, whether parallel or perpendicular to the busbars, has no significant effect on carrier collection because it is uniform in both directions as shown in Figure 6.3. As a result, it appears that the current is proportional to the shaded and unshaded areas of the cell rather than the orientation.

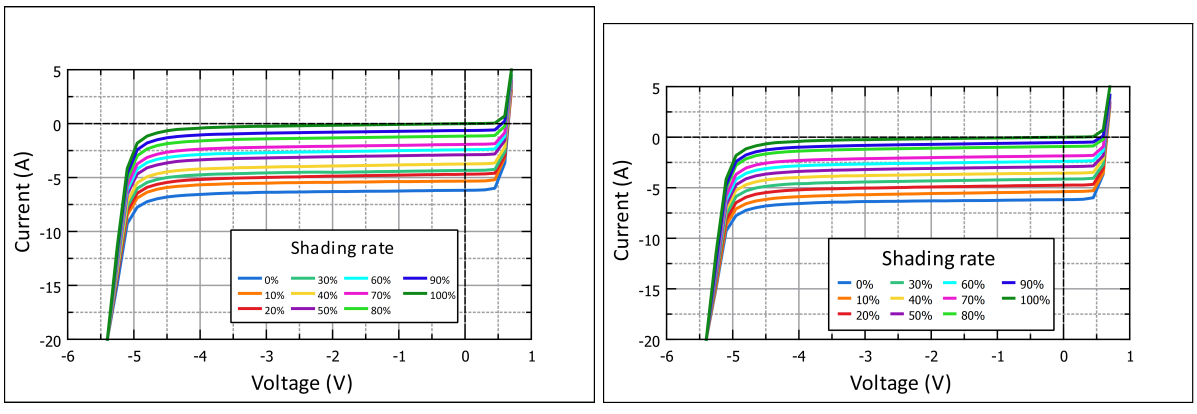

(a) (b)

Figure 6.3: IBC half cut cell shading (a) across the direction of the busbar (b) along the busbar

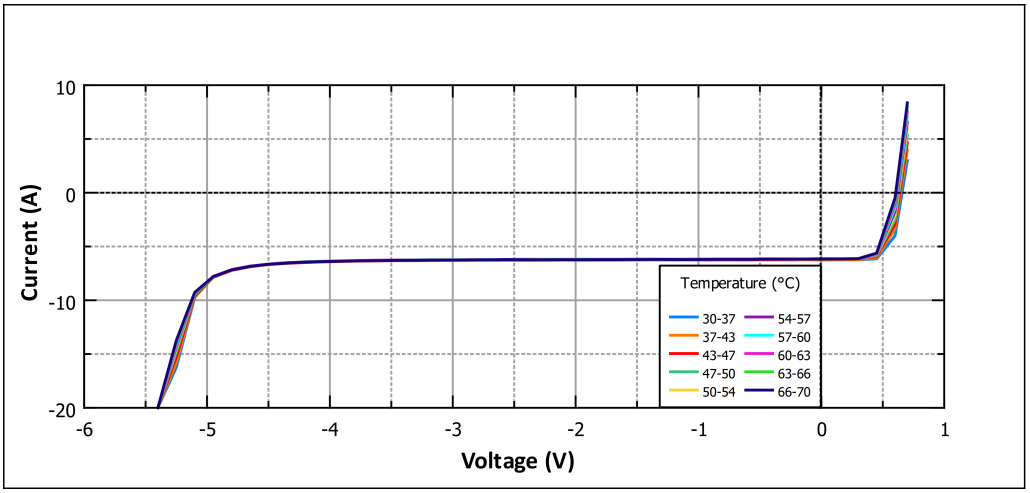

Figure 6.4: Temperature variations of IBC Half-cut cell during a full IV sweep

As mentioned previously in the experimental set-up table 5.2, cell temperature increases significantly yet uniformly up to 70°C, due to temperature control not being applicable during continuous sweeps. Despite the flash having a programmable shutter that opens and closes after each measurement to reduce heating effects from the source, it is inevitable for heating to occur from exposure nonetheless. The recorded temperature rise indicates that both P_{illu} and P_{ph} contribute to power sources in this setup. Another distinctive feature of Zener breakdown is observing temperature changes across multiple IV sweeps to assess its impact. Notably, a negative temperature coefficient (β) was observed during the breakdown in Figure 6.4, indicating that an increase in temperature is likely to lead to an earlier occurrence of the zener breakdown voltage V_z. This trend aligns with the literature discussed in section 3.4.

6.1.2. IBC Full-cells

IBC full-cells were also characterized, with slight differences such as the cell area and current ratings being higher, requiring specific sweep considerations mentioned in table 6.2. Surprisingly, IBC full cells exhibit the same reverse characteristics as the half-cut cells, implying that the observed nature of breakdown and V_{br} are not dependent on cell area but, as previously discussed in section 3.3.4, are an intrinsic material property.

Table 6.2: (a) Conditions of the full-sweep of IBC full-cells and (b) Temperature values of IV sweeps

Sweep Parameters	Values
Cell Area (cm^2)	150
Sweep Range (V)	{-5.6,0.7}
Step (V)	0.23
Delay (ms)	150
Sweep time (s)	15
Temperature (°C)	25

Sweep	Temperature (°C)
1	32–42
2	42–50
3	50–58
4	58–66
5	66–70
6	70–78
7	78–82
8	82–86
9	86–90
10	90–94

It can be observed in the IBC full cells subjected to varying illumination from (0–1) sun that similar IV characteristics emerge as observed in half-cut IBC cells. Full-cells have higher current ratings and a larger cell area, meaning they can conduct or consume at higher sweep ranges beyond the device limit,which results in a flattening of the curve shown in Figure 6.5.

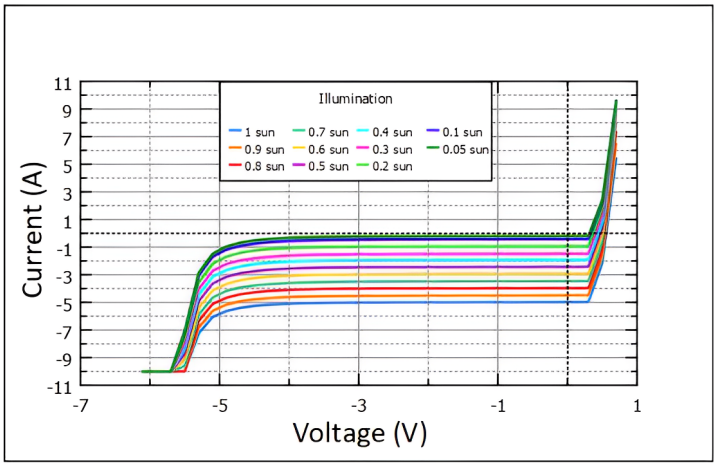

(a)

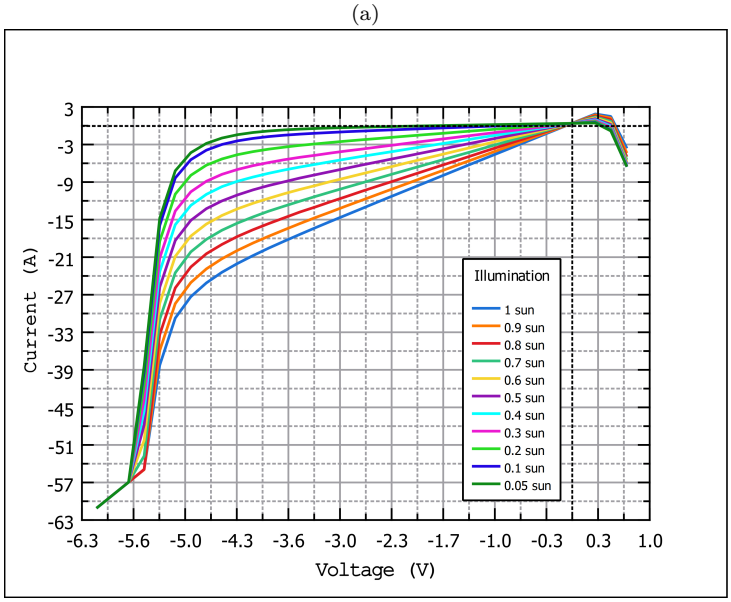

(b)

Figure 6.5: (a) IV curve of the IBC full cell under varying illumination, demonstrating a soft breakdown at (V_Z) = -5V (b) The PV curve of the cell during the sweep shows that power dissipation is much higher under illumination conditions, reaching a maximum of 63 W.

The SUNPOWER IBC full cells were shaded with an opaque cover in both directions as shown in Figure 6.6. However, no distinguishable variation in the drop of the electrical parameters was observed in either shading pattern in Figure 6.7 as presented earlier in the ZEBRA half-cut IBC cells, as the instrument's sensitivity does not allow for a much more accurate sweep in the specified range. This could indicate that the assumption that IBC cell carrier collection is uniform across the cell area holds true or that further analysis must be carried out to explain this observation. More context is provided in section 7.3.

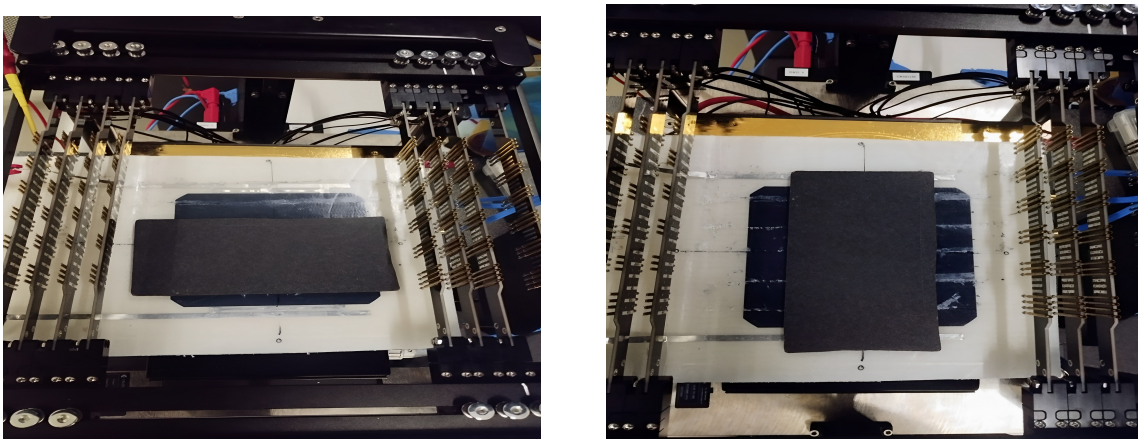

(a) (b)

Figure 6.6: Shading setup during IV sweep of the IBC full cell (a) Parallel (b) Perpendicular to the busbar.

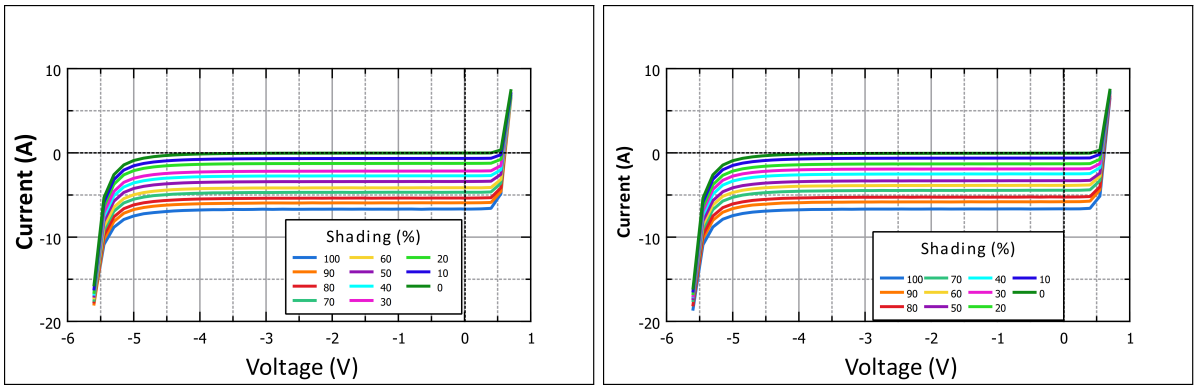

(a) (b)

Figure 6.7: IBC full cell (a) Shading along the direction of the busbar (b) Shading across the busbar

As previously discussed, IBC full-cells also exhibit slight temperature variation, but a full sweep is not possible because the cell's I_{sc} is beyond 10 amps, thereby exceeding the sweep range. Hence a partial sweep only in the breakdown region is depicted in Figure 6.8, as the forward sweep temperature variation is interesting to look into but not needed during reverse characterization. Another observation is the range of temperature rise up to 90°C which is measured using IR camera during the IV sweeps in the table 6.2 shows a higher rise than the IBC half-cut cells.

It was previously discussed in section 6.1.1 that IBC display a negative temperature coefficient (β) until -5V. A closer look suggests that (β) actually switches from negative to positive at around -5 V and beyond. This switching nature is clearly visible in Figure 6.8, where V_z shift is supposed to occur earlier yet the trend is delayed. A simple explanation is that Zener and avalanche processes are both competing, and the magnitude of (β) value depends on which breakdown mechanism dominates, either tunneling or carrier multiplication [72]. Furthermore, the assumption that Zener breakdown occurs in a distinct region is incorrect, as it can be observed that these two processes always co-exist, and a zener breakdown may have a positive or negative temperature coefficient depending on the magnitude of the zener voltage [100].

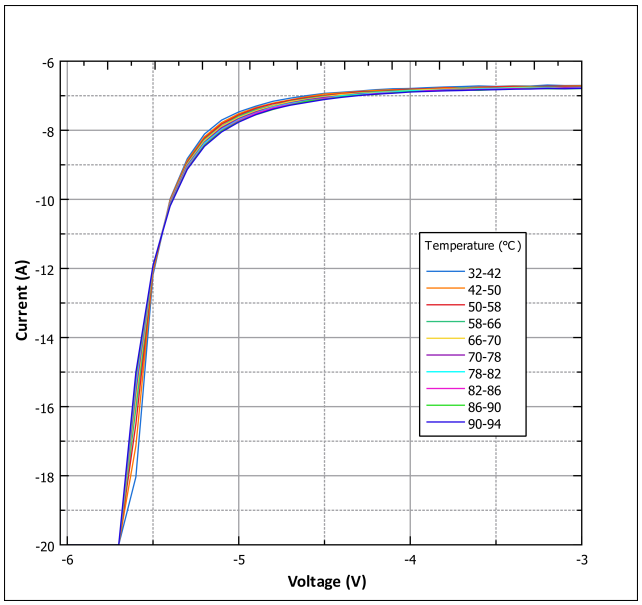

Figure 6.8: Temperature-induced variation in an IBC full cell breakdown behavior

6.1.3. Half-cut PERC

PERC cell technology breakdown is designed with a specific focus on robust operation under high reverse bias, as elaborated earlier in section 3.4. Since half-cut cells only have half the standard current rating, they pose no limitation in characterization. Yet the sweep range has been expanded to exceed -20V as listed in table 6.3, limiting characterization to partial sweeps in breakdown regions due to device constraints mentioned in Appendix B.

Table 6.3: (a) Conditions of the full-sweep of PERC half-cut cells and (b) Temperature values of IV sweeps

Sweep Parameters	Values
Cell Area (cm^2)	125
Sweep Range (V)	{-20.6,0.7}
Step (V)	0.23
Delay (ms)	150
Sweep time (s)	19
Temperature (°C)	25

Sweep	Temperature (°C)
1	25-27
2	27-29
3	29-31
4	31-33
5	33-35
6	35-37
7	37-39
8	39-41
9	41-43
10	43-45

Firstly, the limited sweep range allows a forward sweep, showcasing the expected even influence of illumination (ranging from 0.1 to 0.9 Sun) through reduction of photo-generated current respectively. Secondly, a reverse sweep is feasible only under restricted illumination up to 0.5 sun (SMU cannot manage 1 sun) as shown in Figure 6.9. Moreover, reverse sweeps are subjected to additional heating contributed by P_{rev} for the duration of the sweep which is not observed during forward sweeps in Figure 6.11. Finally, the shading analysis of the M-10 half-cut cell revealed that shading along the perpendicular axis of the busbar(on the side) results in a more significant decrease compared to the parallel direction, as depicted in Figure 6.10.

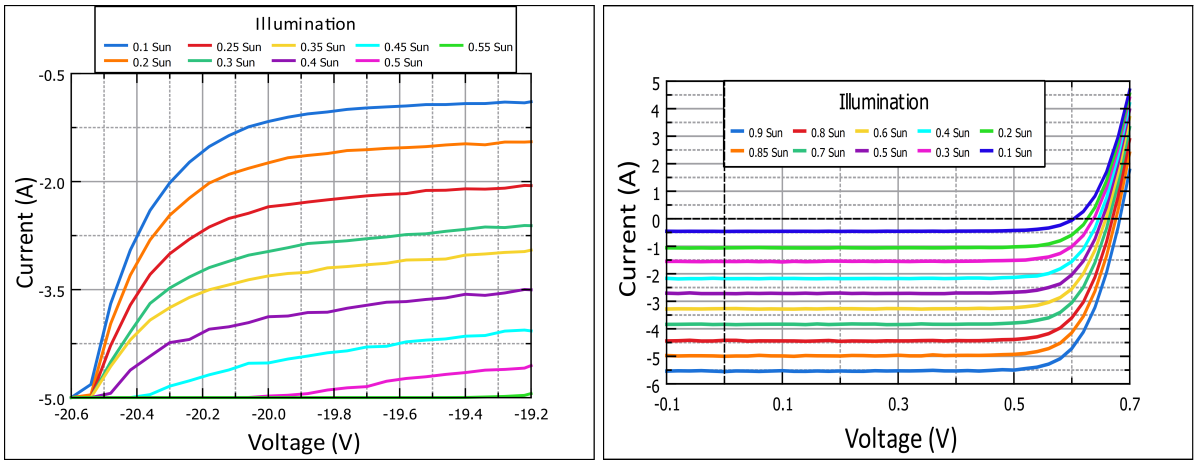

(a) (b)

Figure 6.9: Illumination variation of M-10 half-cut cell (a) reverse bias (b) forward bias

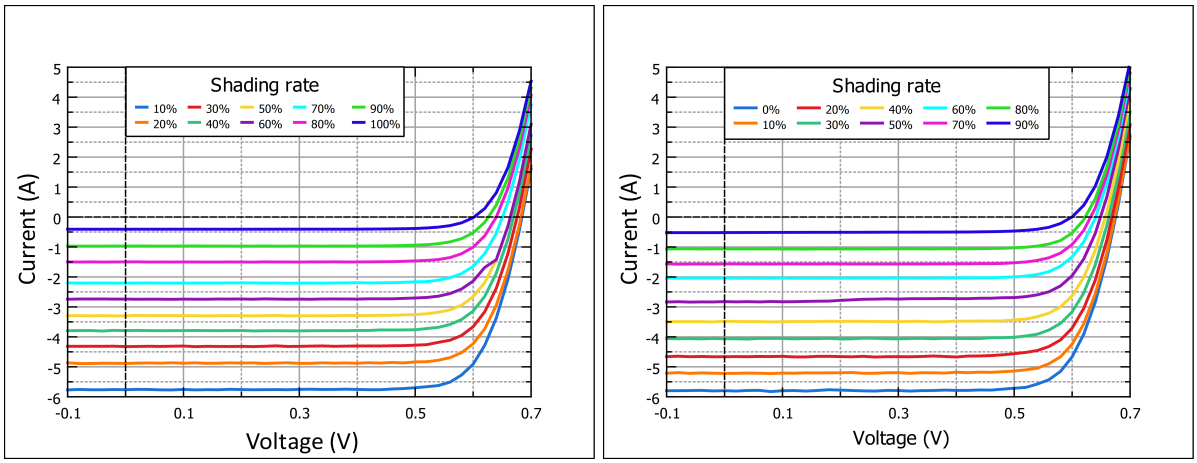

(a) (b)

Figure 6.10: PERC M-10 Half-cut cell shading orientation w.r.t busbars (a) Parallel (b) Perpendicular.

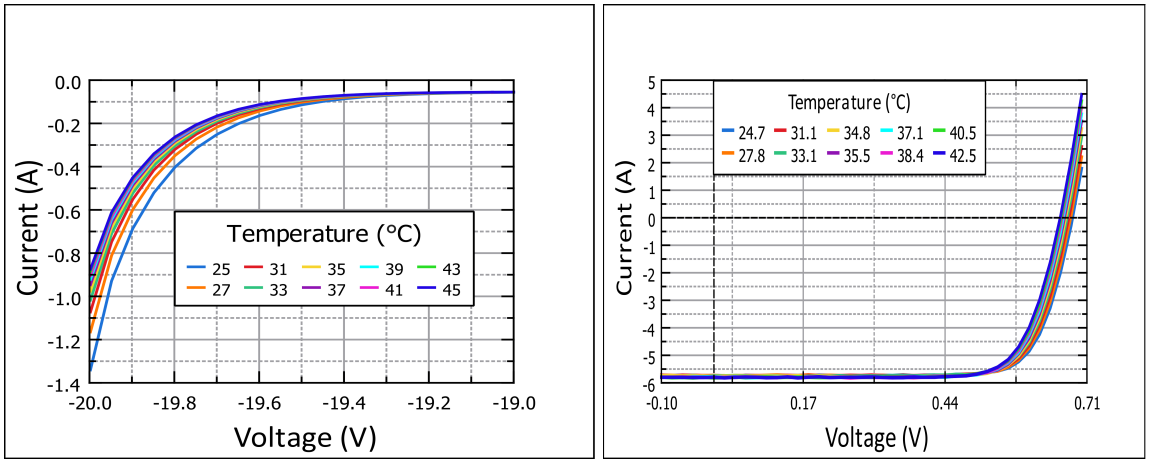

(a) (b)

Figure 6.11: PERC M-10 Half-cut cell temperature variation in (a) reverse bias (b) forward bias.

6.1.4. PERC Full-cells

The widely used PERC full-cell technology, a prevalent industry standard with the highest market share, is also studied for its reverse behavior. Unlike half-cut cells, full cells exhibit higher current limits, driven by larger wafer sizes. Consequently, this prompts a re-evaluation of string lengths, particularly as we approach cell breakdown. To reduce temperature effects observed in half-cut PERC cells, sweep times were reduced per sweep, and single-cell laminates were allowed to cool to room temperature before consecutive readings.The sweeps appear to be less smooth due to the step-voltage limitations discussed in appendix B and the parameters during characterization are provided in the table 6.4 below.

Table 6.4: (a) Conditions of the full-sweep of PERC Full-cut cells and (b) Temperature values of IV sweeps

Sweep Parameters	Values
Cell Area (cm^2)	250
Sweep Range (V)	{-20.6,0.7}
Step (V)	0.2
Delay (ms)	150
Sweep time (s)	12
Temperature (°C)	25

Sweep	Temperature (°C)
1	25-35
2	35-40
3	40-45
4	45-50
5	50-55
6	55-60
7	60-65
8	65-70
9	70-75
10	75-80

As the temperature rises, lattice vibrations become more pronounced, slowing electron-hole mobility [101]. This has an impact on avalanche breakdown, which occurs when electrons driven by a high electric field ionizing atoms upon collision by releasing additional electron-hole pairs. As a result, higher temperatures require higher voltages (electric field) for avalanche breakdown to start demonstrating a positive temperature coefficient (β) as shown in Figure 6.12. This explanation is in accordance with the literature in section 3.4.5.

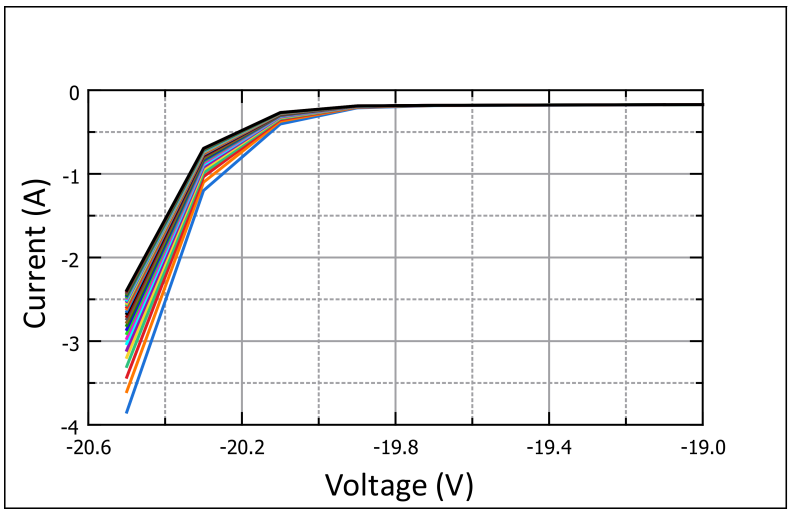

Figure 6.12: Temperature fluctuations of PERC G1 full-cell at V_{br} = -20.3 V during consecutive IV sweeps reveal the positive temperature coefficient trend, causing a leftward shift of V_{AB}.

Figure 6.13a highlights the PERC G1 Full-cell, exposed to different illumination levels (0-0.45 Sun), in steps of 0.05 Sun, experiences earlier and more critical avalanche breakdowns as the sweep progresses. Due to SMU device constants of -5 Amps, the sweeping pattern intentionally reveals the beginning of an onset of avalanche breakdown at around -20.3V. This trend is evident as the curve flattens earlier than anticipated, indicating the sweep's inability to continue beyond this value. Meanwhile, the PV curve in Figure 6.13b reveals a potentially hazardous maximum power dissipation exceeding 102 watts. However, it's important to recognize the cell's I_{sc} sets the threshold for reverse power dissipation as discussed in section 3.2.1. In reality, it may operate at -10 Amps rather than -5 Amps during short-circuit, doubling the potential risk and implying the un-shaded cells can actually hold the weaker cell at 202 watts in reverse.

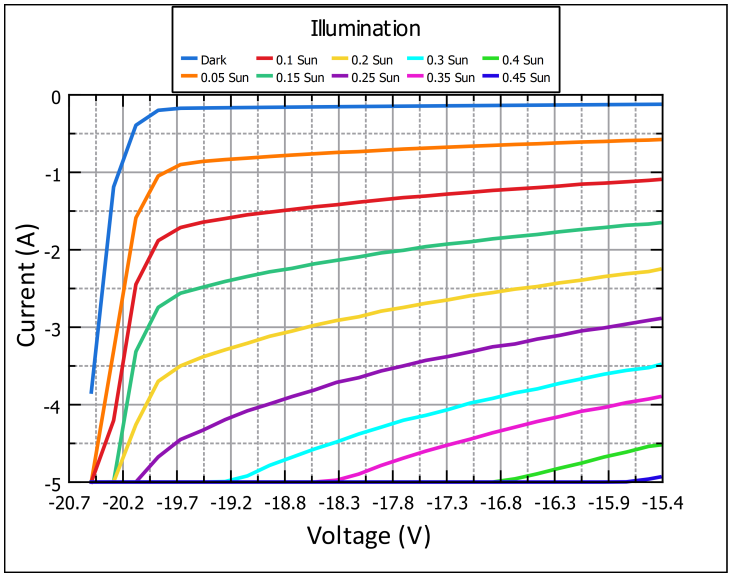

(a)

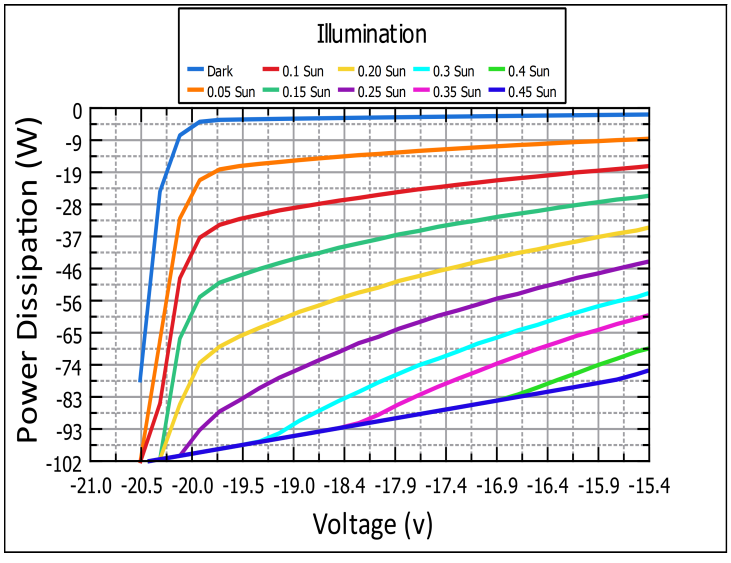

(b)

Figure 6.13: (a) IV curve of the G1 PERC full cell under varying illumination, demonstrating a hard breakdown at (V_{AB}) = -20.3V (b) The PV curve of the cell during the sweep shows that power dissipation is much higher under illumination conditions, reaching a maximum of 102 W.

6.2. Comparision of Hotspots

The heat map with different contours depicts the thermal gradient of the hot-spot, with the hottest part in the center [1]. Since the dissipation is constant and uniform from a point source in the center, it forms a circular pattern shown in Figure 6.14a. According to Newton's law of cooling, heat transfer takes the path that offers the highest thermal gradient with the least resistance [102]. Hence, the center is geometrically the farthest point for cooling [2] as the edges are closer to the metal that have a higher heat conductivity than silicon.A hot-spot near an edge reaches much higher temperatures than a hot-spot in the middle because the heat conductivity in the silicon cell is higher than in the laminated materials made of polymers. Therefore, the heat is distributed over a larger area if the hot spot is in the center [103].

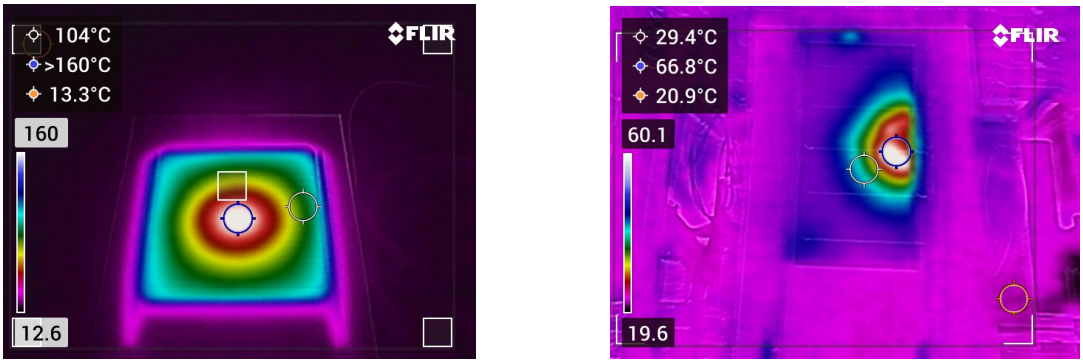

(a) (b)

Figure 6.14: Typical IR image captured of a PERC cell with localized breakdown $V_{\text{br}} = -18.78 \sim 21.2\,\text{V}$ in a complete dark-reverse setup using a FLIR camera with conditions specified in table 6.5: (a) Full-cell; (b) Half-cell with a shunt on the top edge during an IV sweep.

Ideally, due to the rectangular shape of the half-cut cell, the hot-spot would appear as a stretched or elongated circle, resembling an elliptical oval. But in reality, the half-cell dissipates heat in a semi-circular pattern as shown in Figure 6.14b, starting alongside the cut-edge and spreading radially towards the geometric center, following the least path of thermal resistance. This is explained in the previous section 3.1.2, where the cut-edge has stresses induced, making it the point of origin of the hot-spot, which determines its shape, size and location. In contrast to

Table 6.5: Comparison of hot-spots in PERC Full-cell vs. Half-cut cell

Characteristics	Full-cell M10	Half-cut cell G1
Temperature	$> 160°C$	$66.8°C$
Power dissipation	187.8 watts	93.9 watts
Time	30 minutes	5 minutes
Location of origin	Centre	Centre of the cut-edge
Area of cell affected	$127.5\,\text{cm}^2$	$63.36\,\text{cm}^2$
Busbars	10	5

[1] Temperature scale is adjusted to a highly sensitive mode corresponding to the ambient emissivity; The colors are inverted and may not be accurately depicted. A detailed explanation is given in section 5.3.2.

[2] Thermal management of the system plays a role in the shape; predominantly conduction, convection (turbulent) while radiation effects are neglected [63].

PERC cells, where reverse current frequently accumulates in localized regions near the front, most IBC cell designs exhibit a more even breakdown distribution across their entire surface [74]. The placement of interdigitated contacts at the rear, typically made with metals such as silver (Ag) and aluminum (Al) paste, is one significant factor contributing to this non-destructive breakdown behavior [104]. Metals, in general, have a higher thermal conductivity that aids in the redistribution of heat. Another notable advantage of this feature is that it minimizes optical shading losses. By strategically placing contacts at the rear, the front surface remains free from shading, allowing the cell to fully utilize its width for carrier collection. This optimized area reduces contact resistance and enhances carrier collection efficiency.

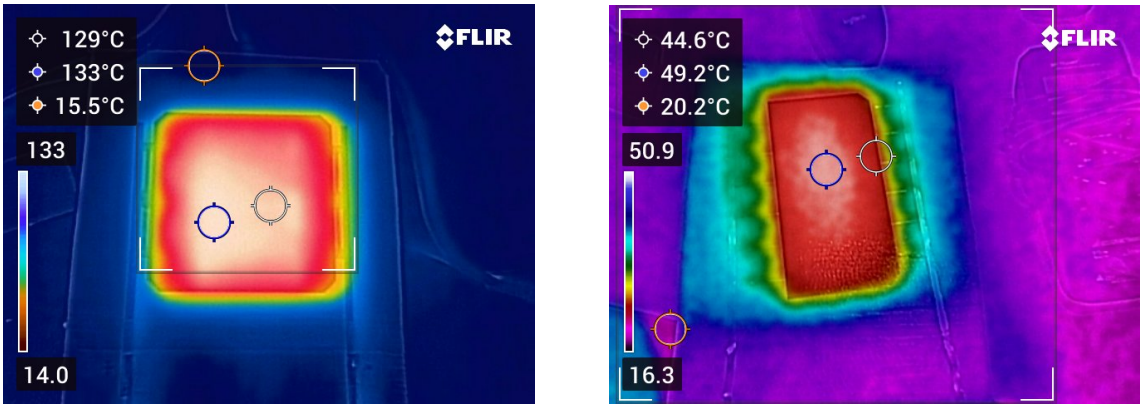

(a) (b)

Figure 6.15: IR image of an IBC cell with homogenous breakdown V_{br} = -5.6V in complete dark-reverse set-up on a FLIR camera with conditions specified in table 6.6 : (a) Full-cell; (b) Half-cut cell with visible heat propagating through the busbars on both sides.

Furthermore, the interdigitated design aids in preventing hot-spot formation within the bulk of the silicon material, as seen in other crystalline cells. Instead, localized p+/n+ junctions are formed at the contacts, where tunneling occurs, limiting the multiplication of charge carriers as discussed in the previous section 3.4.4. All of these features contribute to the IBC cell's hot-spot-resistant design. In simpler terms, IBC cells are not completely free of hot spots, but they significantly reduce the risk of their occurrence.

Table 6.6: Comparison of parameters in IBC Full-cell vs. Half-cut cell

Characteristics	Full-cell	Half-cut cell
Temperature	133°C	49.2°C
Power dissipation	56 watts	33.6 watts
Time	60 minutes	5 minutes
Location of origin	Whole cell	
Area of cell affected		
Busbars	Interdigitated	

Now that the cell technologies have undergone IV sweeps analysis, a natural step of progression was to validate the hypotheses behind these observations. In both figures 6.27d and 6.15a, the PERC and IBC experiments were conducted under dark conditions using a DC power supply to induce a reverse current exceeding the cell's operational breakdown voltage. This accelerated testing disclosed that the IBC full cell exhibited a uniform temperature rise of 2.3°C/min recorded by the thermocouple over a one-hour period as shown in Figure 6.16, with no visible damage observed in Figure 6.17a, aligning with the findings from the sweeps.

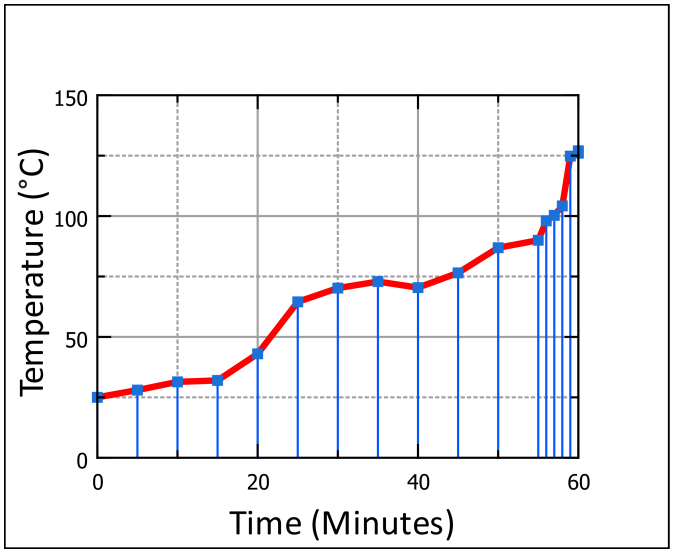

Figure 6.16: Temperature vs time trend map of IBC full cell under dark reverse for one hour reaching a maximum temperature of 133°C.

In contrast, the PERC cell had surpassed the temperature threshold within 30 minutes, displaying visible damage that substantiated the validation of hard breakdown characteristics in Figure 6.17b. However, the temperature increase was not recorded due to a loose thermocouple that, in certain cases, even fused with the front sheet.

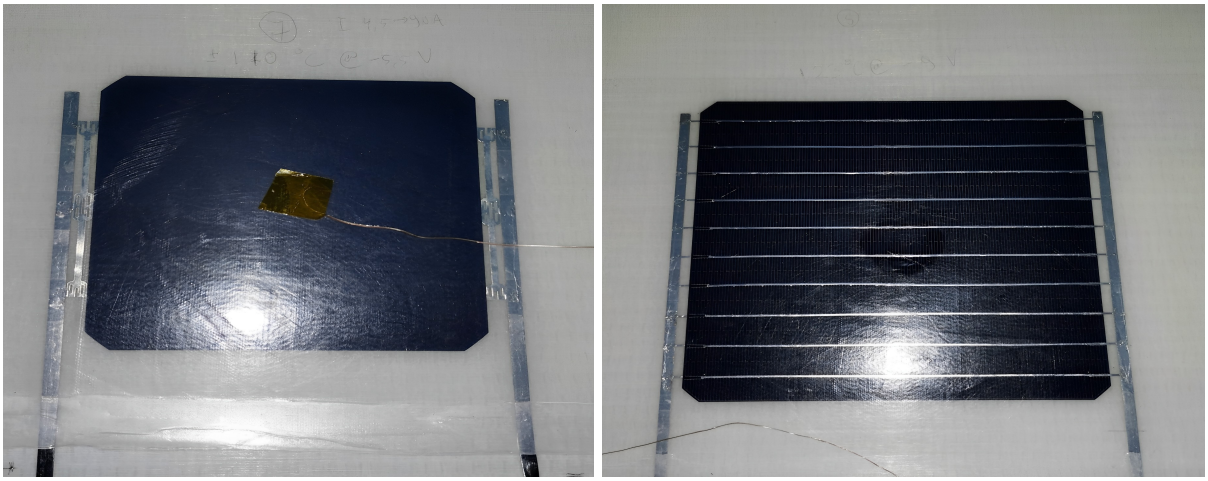

(a) (b)

Figure 6.17: (a) IBC Full-cell with no visible damage (b) PERC M-10 Full-cell has visible damage in the centre.

6.2.1. Illuminated Vs Dark

A question that often intrigues researchers is, "Which specific location of the partially shaded cell contains the hot-spot , the illuminated or the dark portion?". It has been observed that almost always the part of the solar cell that is exposed to light while still producing electricity consumes the power it generates, resulting in the highest temperature given that the cell is defect-free and has optimal carrier collection and uniformity [85].

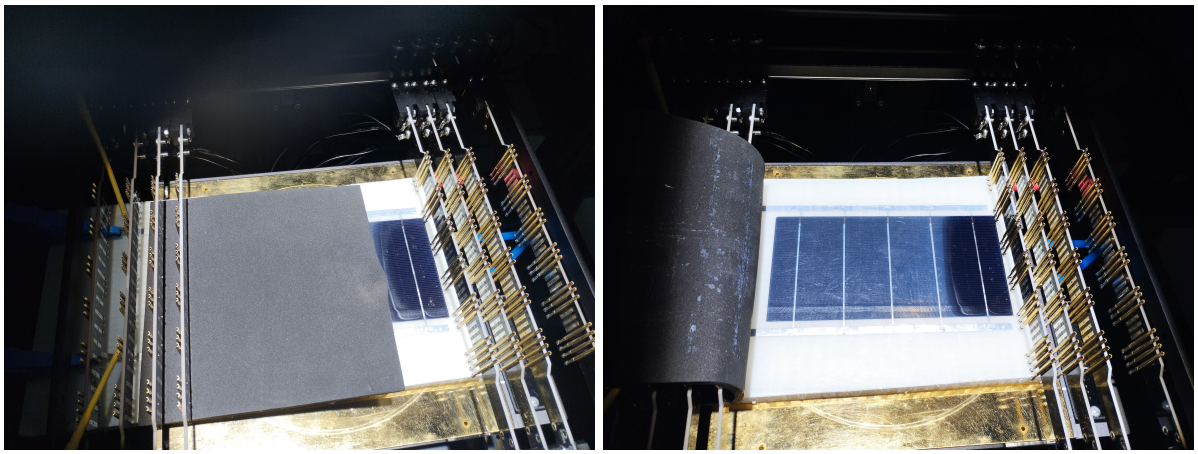

(a) (b)

Figure 6.18: G1 half-cut (PERC) cell under reverse sweep (a) Partially covered with opaque material (b) Uncovered part reveals the shaded area remains unaffected, while only the illuminated region has visible damage.

Notably, the shaded area experiences a lesser impact of power dissipation due to its lack of generation. Therefore, in a practical scenario where one were to inspect a solar cell, partial shading caused by external objects, such as when a leaves casts a shadow, would make the hot-spot readily visible, in contrast to prevailing expectations that hot-spots would remain concealed beneath shading objects. This phenomenon is recreated specifically during an IV sweep to demonstrate this behaviour as shown in Figure 6.18 and verified by the hot-spot pattern coinciding with the IR camera image in Figure 6.19.

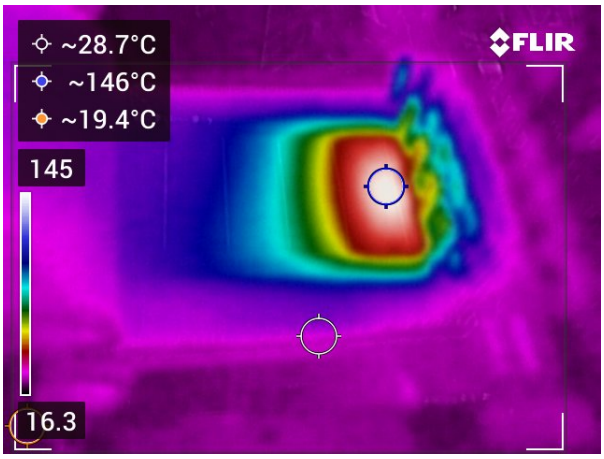

Figure 6.19: The IR camera reveals the heat dissipation pattern with a maximum temperature of 146°C.

6.3. Phase-02

Moving on to a series of cells, it became clear that a larger DC power supply is required to create electric fields across not just one cell but multiple cells in a string. Applying Kirchhoff's law, reverse breakdown voltages are added cumulatively as well [88].

6.3.1. 3 cells in series

Three single-cell laminates were chosen from the same batch and used for this experiment. These cells were ranked based on open-circuit voltage measured by a multi-meter in ambient illumination. They were then connected to a DC power supply in reverse in a dark room setup to assess if the predicted cells heated up as shown in Figure 6.20a. After applying a breakdown voltage three times the original up to -60V, the cells operate in -10Amps which then progressively heated up with a total 600 Watts of power dissipation in the string. The parameters are specified in the table 6.7. Notably, cell-1 with the lowest V_{oc} heated up first and reached the highest temperature in Figure 6.20b. This indicates that the weakest cell restricts power dissipation until it reaches its limits. It then redirects the generated heat to the next cell in line, causing it to emerge as the center of power dissipation—essentially becoming a hot-spot. This act of cells sacrificing themselves highlights the dynamic interaction within the string.

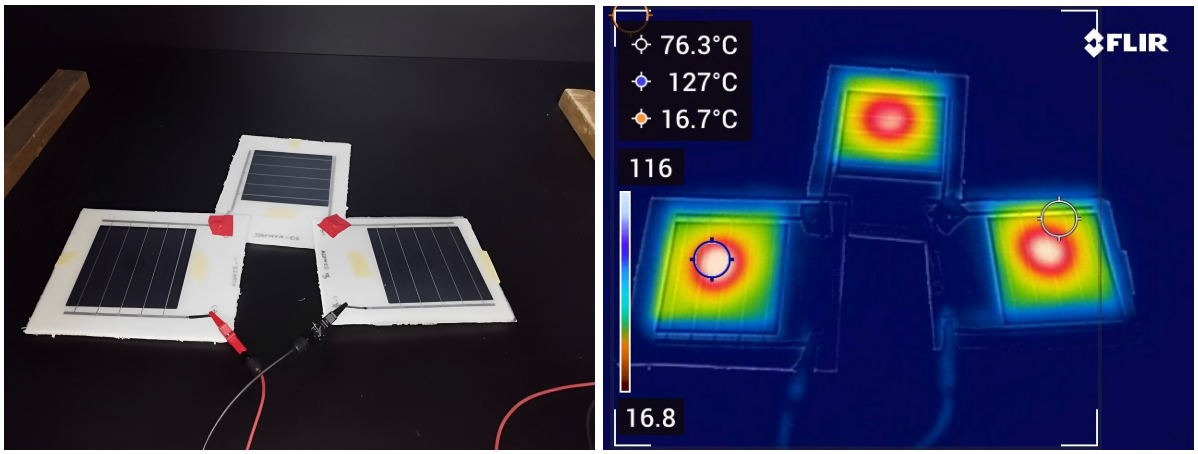

(a) (b)

Figure 6.20: (a) PERC G1 Full Cell-1 (left), Cell-2 (right), Cell-3 (middle) in series in a dark reverse for 10 minutes (b) Cell-1 shows the highest temperature at 127°C

Table 6.7: Breakdown Parameters

Configuration	V_{oc} (V)	V_{br} (V)	$T_{hotspot}$ (°C)	P_{diss} (W)
Cell 1	0.453	19.6	127	196
Cell 2	0.456	19.7	119	197
Cell 3	0.466	20.3	93.6	203

Here, in the above mentioned setup, the power dissipation (P_{diss}) in each cell is given for the duration of the experiment. Meanwhile, $T_{hotspot}$ was the maximum temperature reached and finally, V_{br} is the voltage recorded when the cells started to show a significant rise in current.

6.3.2. 4 cells in series

The same experiment was repeated with four cells, yielding the same consistent results as previously discussed in section 6.3.1. While avoiding repetition in testing, it's worth noting an interesting observation made while monitoring a hot-spot and how it forms over time. As discussed earlier in the section 3.2, the main difference between a shunt and a hot-spot is how they affect the localized reverse current flow. A shunt highlights certain areas of vulnerability on the cell but has a smaller impact on temperature compared to a hot-spot. A hot-spot, on the other hand, forms after a significant breakdown occurs in the cell. In this phase, the shunt disappears as the hot-spot begins to intensify as shown in Figure 6.21, with higher current densities accumulating in the region. Thus, while both are driven by the same magnitude of reverse current, they occur at different stages, meaning that a hot-spot is much more severe than a shunt formation and the temperatures recorded for a hot-spot are much significantly higher than localized shunts.

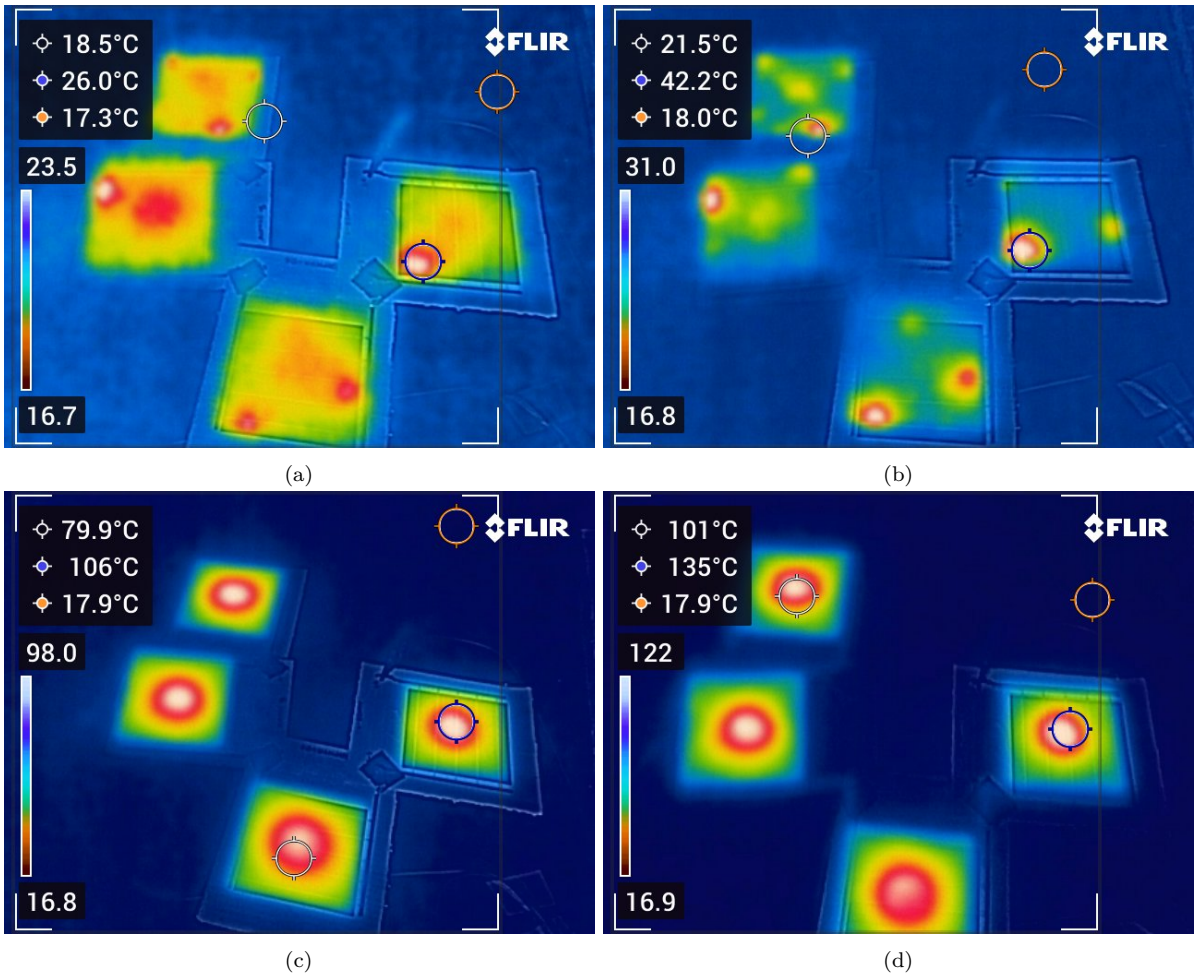

Figure 6.21: Formation of shunts across the all cells indicating defects: (a) Initial shunt formation (b) Shunt intensity increases in specific regions (c) Emergence of a distinct hot-spot pattern (d) Maximum temperature reached at 135°C.

6.3.3. 6 cells in series

Finally, the experiment was extended to a 6-cell string architectures. The breakdown occurs at around -120V, but the DC power supply limit is at -105V, yet it still manages to drive enough currents in reverse to observe hot-spots across all six cell strings. However, with the increased number of cells, individual cell behaviors emerge, making it complex to anticipate the sequence of hot-spots. To address this, EL imaging alongside an IR camera proves valuable, as it helps correlate some cells that exhibit similarities to defects and hot-spots as shown in Figure 6.22.

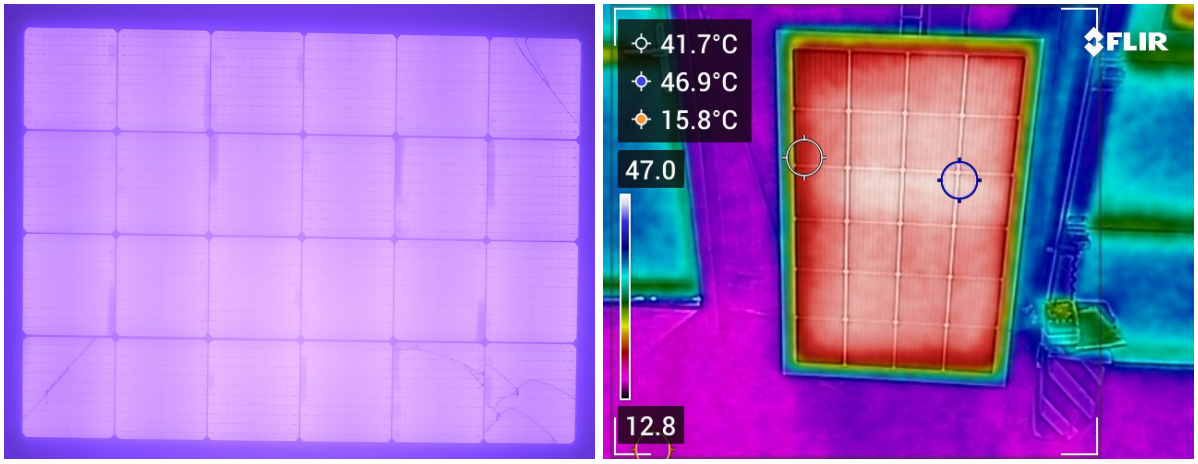

(a) (b)

Figure 6.22: (a) EL image of a 24 cell module showing major cracks and defects. Orientation starts with cell A-1 (Top-right) for reference (b) IR image of the module for reference in open-circuit under outdoor conditions.

With 24 cells, the study is conducted string-wise as follows. The voltage drop method is performed on the module with reference of defected cells [3] obtained from comparing the EL image above. The predicted order is mentioned in table 6.8 below.

Table 6.8: Voltage drop Index $\Delta V = V_0$-V with predicted and measured cells with the highest temperature among the string of cells.

String/cell	6	5	4	3	2	1	Predicted Cell	Measured Cell
String A	0.09	0.09	0.09	0.08	0.09	0.10 *	A4	A3
String B	0.09	0.08	0.09	0.09	0.10	0.09	B2	B3
String C	0.08	0.09	0.09	0.08	0.09	0.07	C1	C1
String D	0.09*	0.09	0.09	0.09	0.09*	0.10**	D1	D1

The relationship between defects, voltage drop, and temperature is complex. Defective cells with notable voltage drops don't always exhibit the highest temperatures. For example, while C1 lacks defects, it experiences elevated temperatures. Conversely, heavily defected D1 shows high temperatures. Despite some success in C and D cell strings, relying solely on the voltage drop method for predicting hot-spots remains inconclusive due to these variations. For more information of the schematic of the module, refer to Figure 6.23.

[3] *- Defect cells **- Highly defect cells

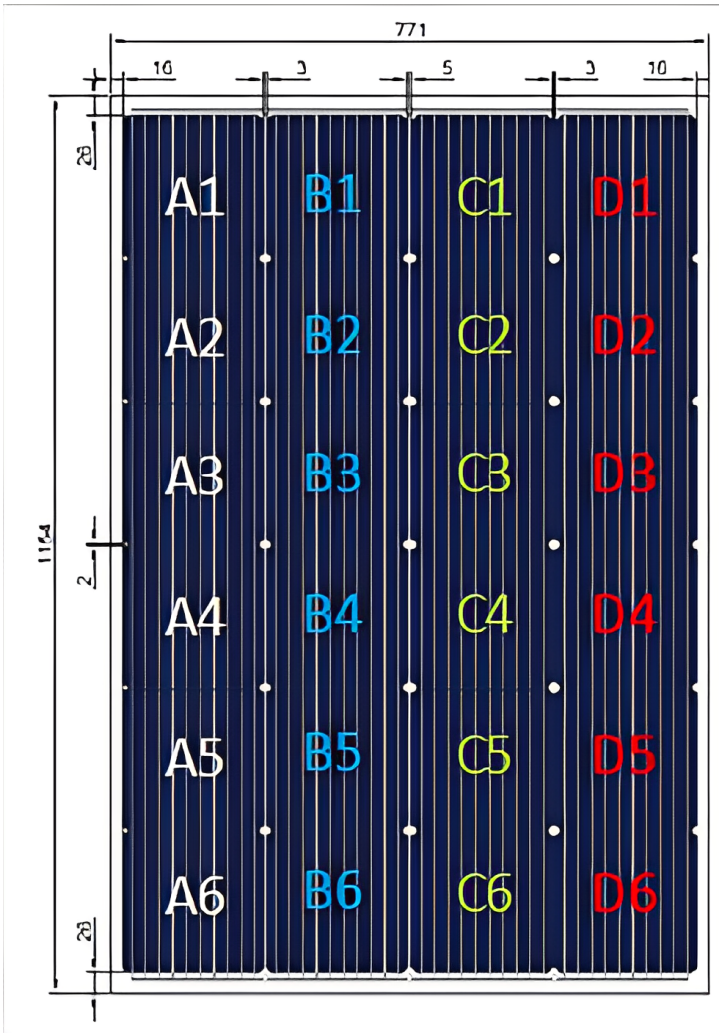

Figure 6.23: Schematic of PERC M-10 Full-cell 24 string module with cell order in vertical orientation for reference. The design of this R & D module is for testing purposes only.

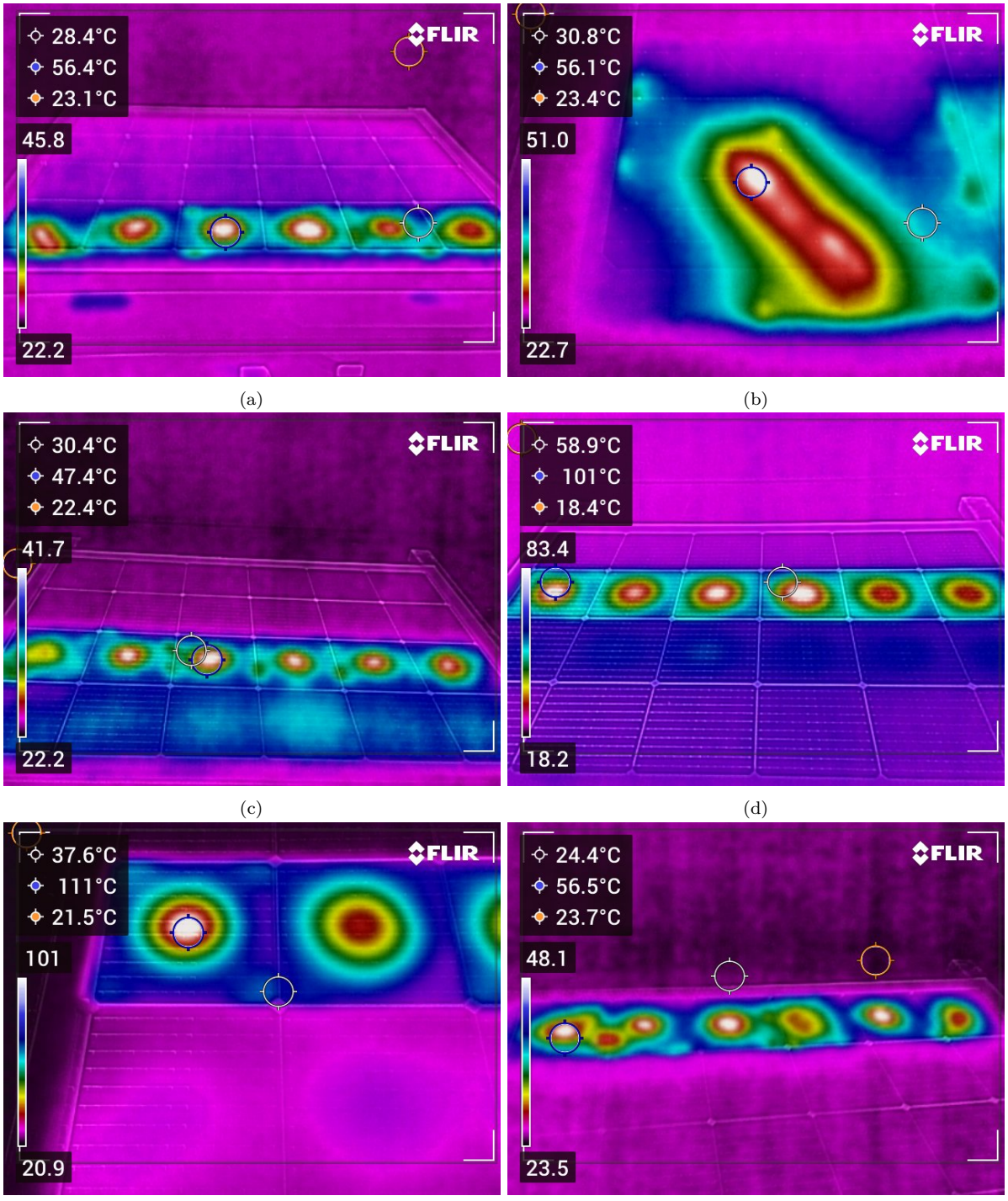

Figure 6.24: (a) String A: Cell A-3 records the highest temperature. (b) Cell-A1's enhanced image reveals a hot-spot propagating along a defect, altering its shape. (c) String B: Cell B-3 exhibits the highest temperature. (d) String C: hot-spot temperature recorded in all strings at Cell C-1. (e) Enhanced image of Cell C-1 at 111°C. (f) String D reveals pronounced defects, influencing multiple cells with distorted hot-spots.

6.4. Phase-03

As the voltage drop approach lacked conclusive results, phase-03 employs a similar configuration of M-10 PERC 24-full-cell string module without bypass diodes for rigorous hot-spot testing under the IEC standard for a better understanding of hot-spots. The setup specifics are detailed in section 5.5, which covers the equipment, and in section 4.2 which covers the methodology. The objective of Solarge is closely aligned with this core thesis goal: achieving passing the certification test while determining optimal string lengths and temperatures. The outcomes of these experiments hold significant weight in shaping the design parameters for Solarge modules. Additionally, the R&D prototype module used in phase 02 cannot be reused for phase 03 experiments. To mitigate the risk of recurring defects in hot-spots, a new module without cracks was fabricated as shown in Figure 6.25.

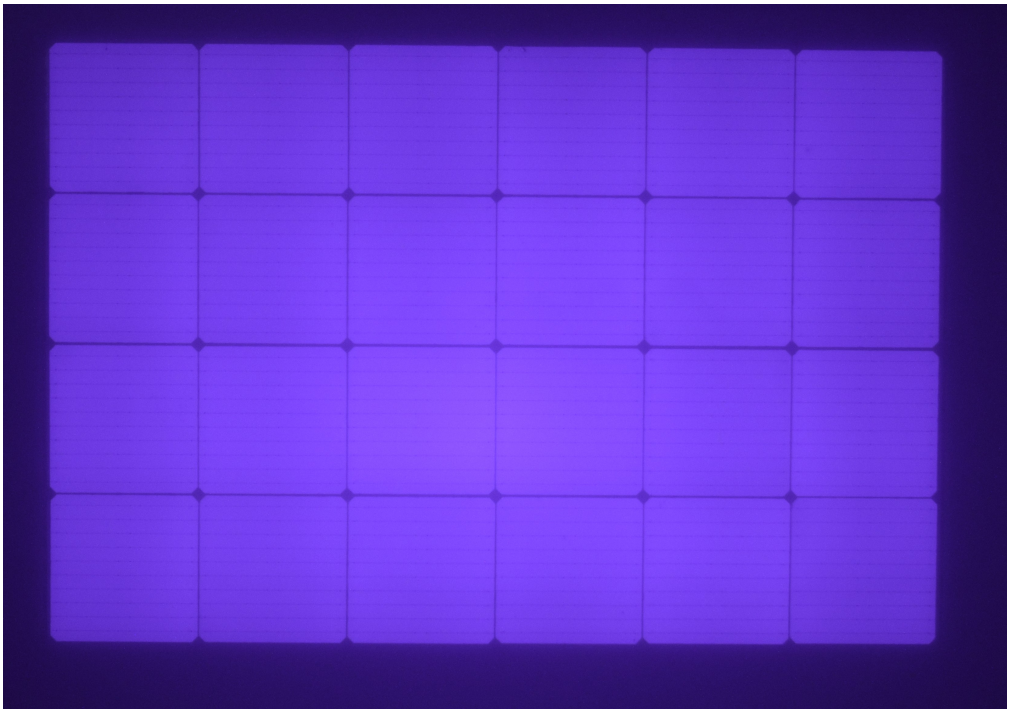

Figure 6.25: EL image of the new module with no cracks

Subsequently, the focus shifted exclusively to PERC, primarily M-10 cells. To summarize the progression, the initial phase encompassed 8 different cell types, which were subsequently reduced to 5 due to device constraints, and finally narrowed down to a single configuration for the hot-spotting investigation. Another compelling reason for this choice is the practical availability of samples at Solarge's disposal; given the hazardous nature of hot-spot testing, a surplus of cells is required for testing and discarding, demanding substantial resources for each experiment. Firstly, it was crucial to allow the module to reach steady-state in open-circuit condition for temperature and voltage stabilization as shown in in Figure 6.26. This preliminary step was followed by manual data collection using a thermocouple and multimeter to ensure accurate measurements could be replicated and used as a reference for future readings. Then the module was short-circuited to identify the hottest cells string wise as shown in Figure 6.27.

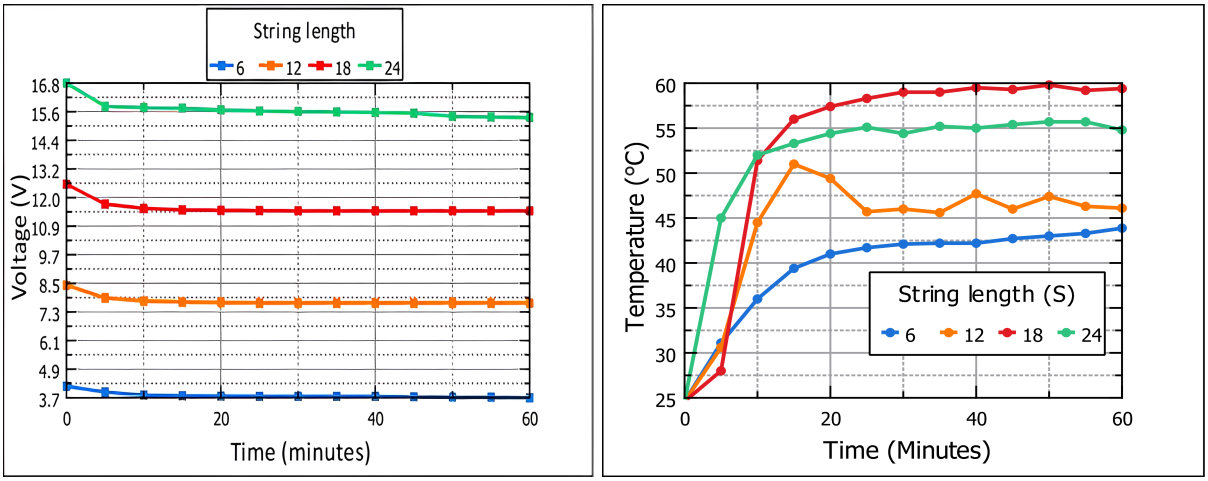

(a) (b)

Figure 6.26: (a) The voltage stabilizes within 20 minutes under 1 sun illumination (no shading) in open-circuit conditions (b) while the module temperature reaches a steady state of 50°C. Thermocouple came loose during string length (S) = 12 configuration.

Different shading rates (x) were achieved using various cover sizes, including 0, 10, 15, 20, 25, 50, 75, and 100 percent. However, only 18 cell-strings were tested across all these levels, as it was more logical for Solarge to focus on 12-cell configurations and above, which align with their current string length. Other string lengths underwent shading under specific conditions: 0, 20, and 100 shading for short-circuit, worst shading, and open circuit scenarios, respectively. Moreover, because of time limitations, the other shading rates were not included in the study. Each endurance test itself is quite time-consuming, lasting for an hour, and the various combinations of the matrix are extensive.

Table 6.9: Overview of Hot-spot endurance test paramters

String Length	Max T (°C)	Worst shading rate (x)	P (W)	Q (W/cm2)
6	81.50	20	62	0.192861
12	108.2	20	106	0.376655
18	134.40	10	150	0.529
24	165. 8	20	193	0.6963

Table 6.9 presents an overview of the measurement results. In this context, P(W) and $\dot{Q}$ (W/m^2) were computed using equations 3.5 and 3.6 respectively. These calculations offer a reference for understanding the amount of power dissipation and temperature rise associated with each string length. It's important to highlight that these values are approximations, as there isn't a standard power dissipation vs hot-spot temperature rise relationship available. Yet still, a clear trend emerges, illustrating a direct relationship between string length and temperature, as demonstrated in Figure 6.38. This is due to the linear increase of voltage due to increase of string length. However, a detailed investigation into the module's thermal properties falls outside the scope of this thesis.

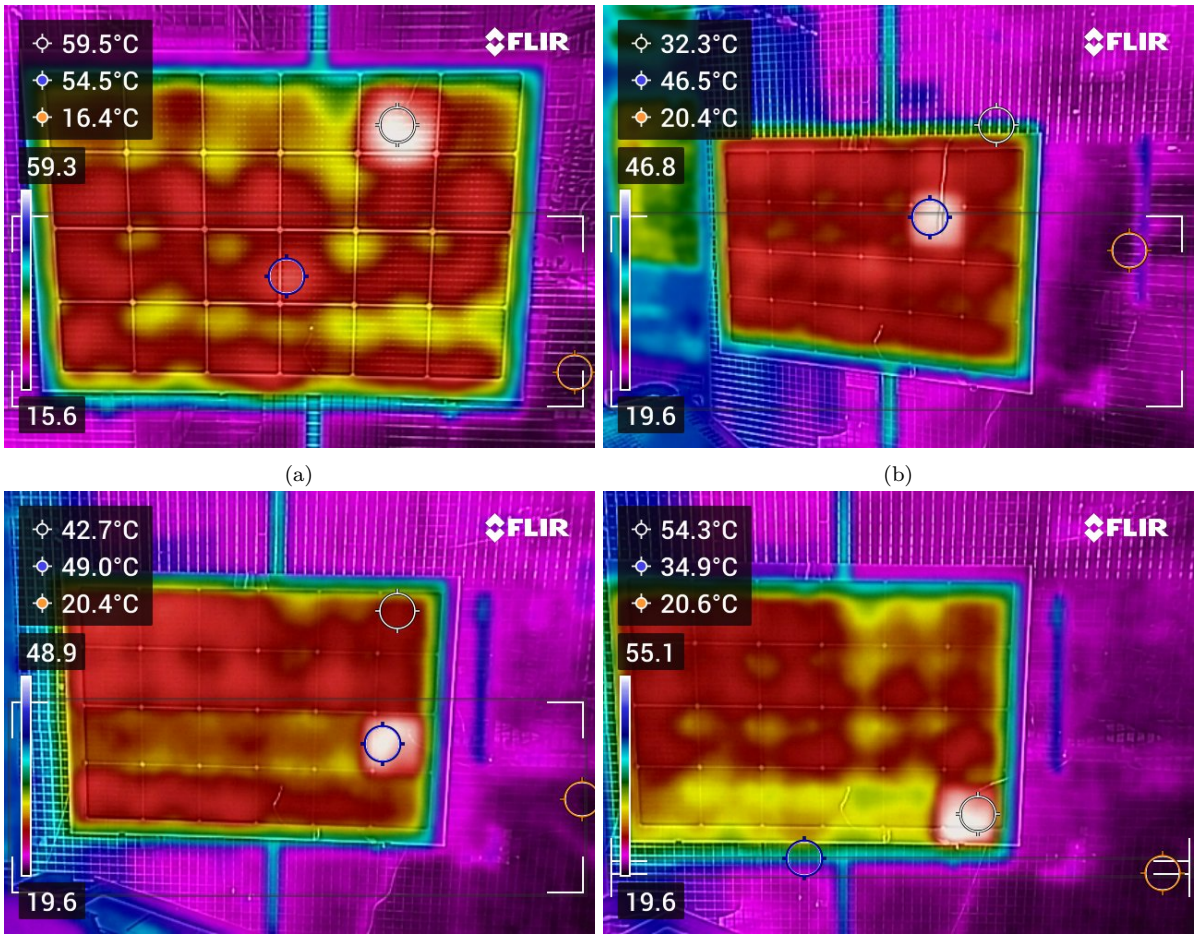

(a) (b)

(c) (d)

Figure 6.27: Highest temperature recorded in each string (no-shading): (a) String A: Cell-A2, (b) String B: Cell-B2, (c) String C: Cell-C1, (d) String D: Cell-D1.

6.4.1. 6 cell string

Previously in phase-02, the study observed the emergence of hot-spots in a series of six cells. This current phase introduces a different method where the external DC supply is eliminated. Instead, the cells create their own short circuit by utilizing the unshaded strings for power. Having identified cell A-2 as the one attaining the highest temperature during short-circuit, it is now selected for in-depth hot-spot analysis.

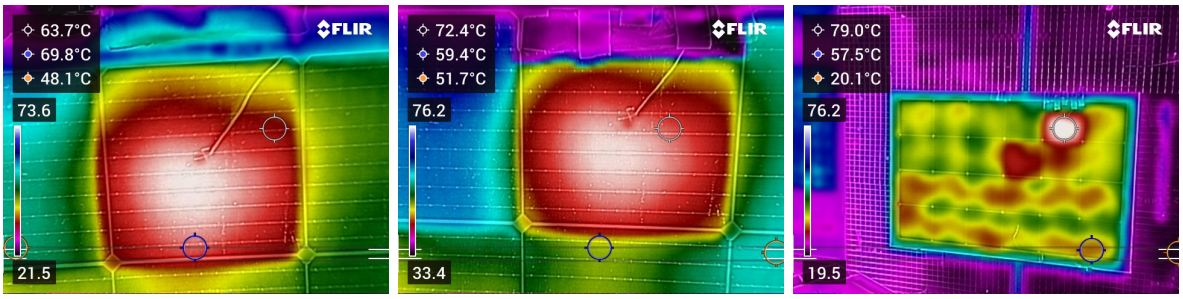

(a) (b) (c)

Figure 6.28: 6-cell string under 20 shading: (a) Zoomed image without shading cover, revealing the complete hot-spot pattern underneath. (b) Zoomed image with intact shading cover. (c) Wide shot view.

The temperature shown in Figure 6.28 is consistent with the measured value of 81.50°C as detailed in table 6.10. It's worth noting that the thermocouple readings provides a closer approximation within the same range for the experiments. Additionally, the IR camera is constrained in its ability to monitor temperature continuously, restricting its operation to capturing images only once the experiment has concluded. It's important to note that the distance of an object from the IR Camera can affect the recorded temperature due to changing emissivity scales. Close-up shots are less susceptible to errors compared to wide shots, which can be influenced by ambient background noise, potentially altering the scales used for temperature measurement.

Table 6.10: Temperature vs time values measured for 6 cells at x=20 percent.

Time (Minutes)	Hot-spot temperature (T1) °C	Module Temperature (T2) °C
0.00	26.50	26.30
5.00	65.70	37.40
10.00	73.90	42.30
15.00	76.00	43.40
20.00	76.00	44.90
25.00	77.40	46.70
30.00	76.80	46.20
35.00	78.50	44.20
40.00	78.90	45.60
45.00	80.90	44.50
50.00	81.50	45.00
55.00	81.20	46.50
60.00	80.00	44.70

6.4.2. 12 cell string

Currently, Solarge utilizes a string length of 12 cells, indicating that this setup is not yet approaching its maximum capacity, but rather aligns with current standards. However, as the use of half-cut modules continues to expand, with configurations requiring up to 144 cells per module as mentioned in section 3.1.2, it is inevitable that string lengths will also increase accordingly. To facilitate this, the junction boxes are split and additional bypass diodes are added to avoid overheating [56].

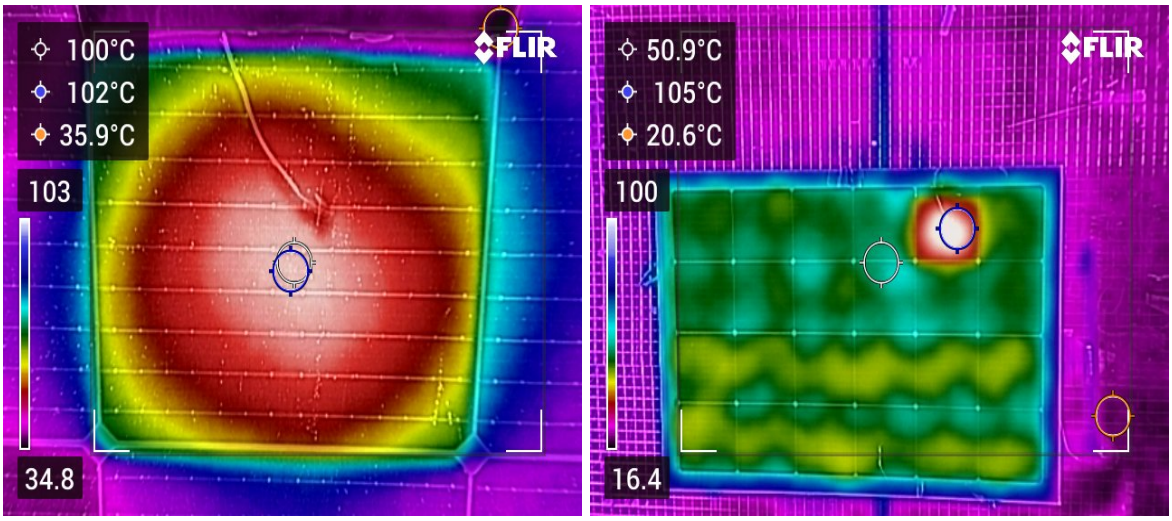

(a) (b)

Figure 6.29: 12-cell Series at no-shading: (a) Uncovered, (b) Covered, (c) Wide View of Module with maximum temperature of 105 °C.

The temperatures depicted in figures 6.29 and 6.30 align with the recorded temperatures of 108°C as indicated in table 6.11. The temperature profile exhibited a rapid surge during the initial 10 minutes, essentially defining the temperature range the string length would achieve. Subsequently, over the span of 1 hour, the temperature gradually climbed, eventually reaching stability as mandated by the IEC test standard. This rapid initial increase serves as a crucial indicator for predicting the temperature range that the string length is likely to encounter.

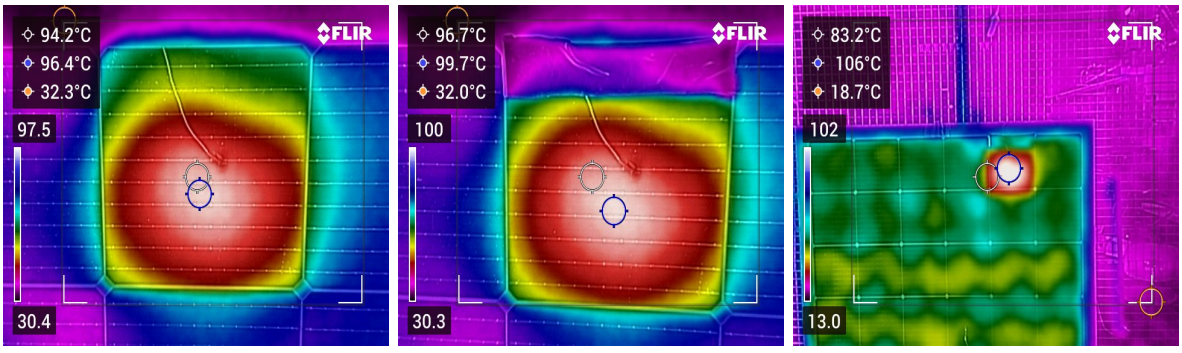

(a) (b) (c)

Figure 6.30: 12-cell Series at 20 percent Shading: (a) Uncovered, (b) Covered, (c) Wide View of Module with maximum temperature of 106°C.

Table 6.11: Temperature vs time values measured for 12 cells at x=20 percent.

Time (Minutes)	Hot-spot temperature (T1) °C	Module Temperature (T2) °C
0.00	33.00	28.00
5.00	90.30	42.10
10.00	102.80	46.80
15.00	105.20	47.80
20.00	106.10	47.10
25.00	107.40	51.00
30.00	103.90	52.40
35.00	104.70	52.80
40.00	103.00	53.00
45.00	107.20	53.90
50.00	108.20	53.50
55.00	107.60	52.90
60.00	107.30	52.60

6.4.3. 18 cell string

After observing that the 6-cell and 12-cell setups reached a maximum temperature range of 110°C, still comfortably below the 160°C failure limit for testing, the focus shifts to an 18-cell string. However, this step brings us closer to the safety threshold as this particular string length offers an ideal opportunity to explore different shading rates for Solarge's investigation. In doing so, certain thermal effects started to wear of cell-A2 in Figure 6.31, hence cell-A3 which was next in line in the order was chosen for the remaining endurance tests. Furthermore, the analysis of various shading rates in string length of 18 was of interest for Solarge to determine the worst case scenario for the modules.

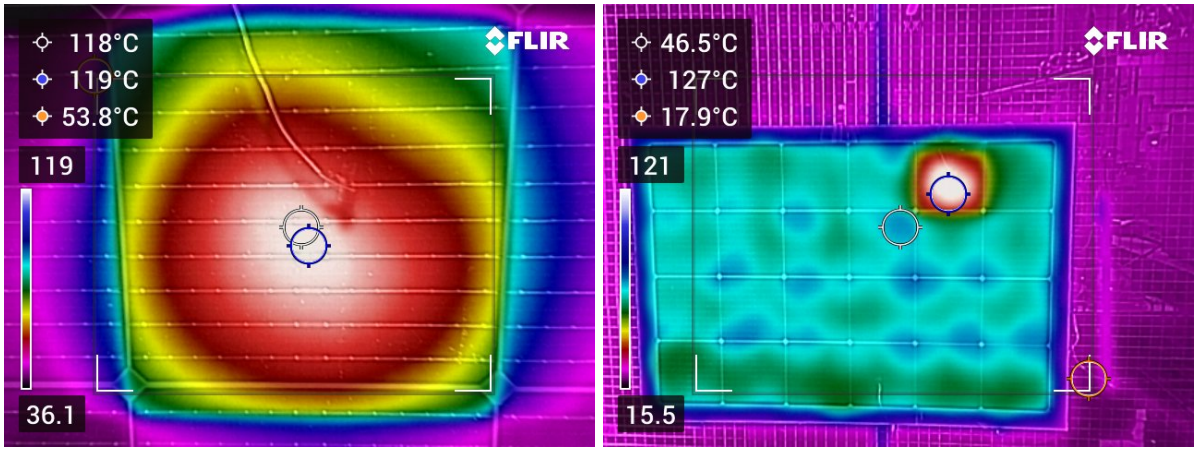

(a) (b)

Figure 6.31: 18-cell Series no-shading: (a) Uncovered, (b) Wide View with maximum temperature of 127°C.

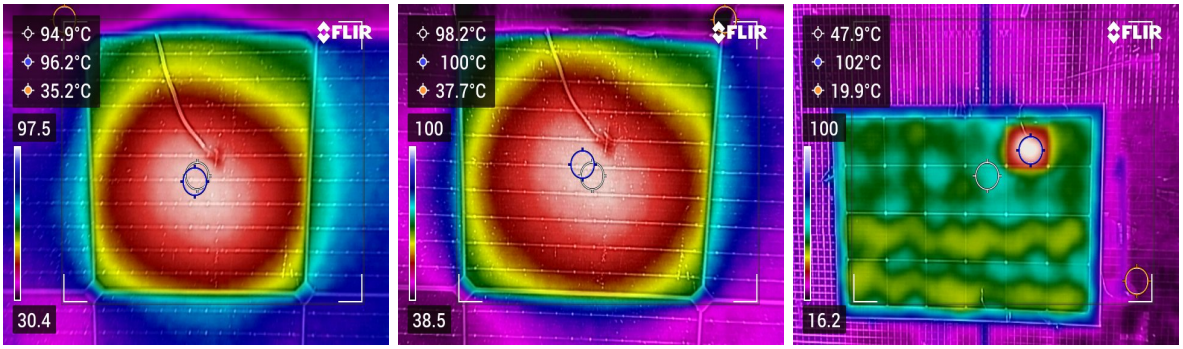

(a) (b) (c)

Figure 6.32: 18-cell Series at 10 percent shading: (a) Uncovered, (b) Covered, (c) Wide View of Module with maximum temperature of 134°C.

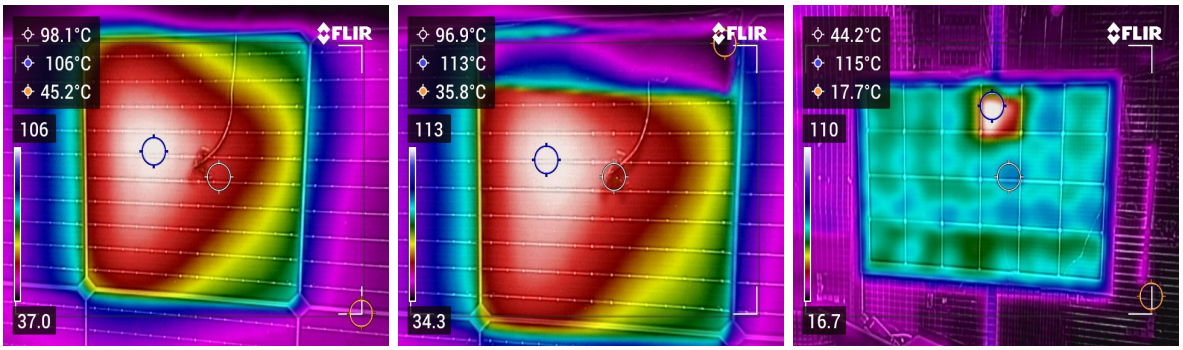

(a) (b) (c)

Figure 6.33: 18-cell Series at 15 percent shading: (a) Uncovered, (b) Covered, (c) Wide View of Module with maximum temperature of 115°C.

The location of the hot spot varies with different shading levels. In some cases, the observed hot spot location may not align with the assumed geometric center of the thermocouple's position, potentially leading to temperature readings that appear relatively low in Figure 6.32. Another intriguing observation is the transformation of the hot-spot shape from a circular pattern to a stretched ellipse within the illuminated section of the shaded cell in figures 6.33, 6.34 and 6.35 respectively. Moreover, capturing cell images post-hot-spot testing using the IR camera, following removal of the shade cover, serves to showcase that the shaded portion remains comparatively less impacted than the illuminated region in figures 6.36 and 6.37, thereby confirming the hypothesis stated in section 6.2.1 that the hot-spot occurs in the illuminated region of the cell. However, it's worth noting that the shading cover also contributes to insulating the cell from source light and heat, which plays a significant role in these outcomes.

Moreover, it's crucial to capture a wide shot of the entire hot-spot area immediately with IR camera after the experiment ends before cooling effects alter the results. The vertical simulator set-up has been intentionally designed for easy access of the module, a feature lacking in both TU Delft and Solarge setups, which employ horizontal steady-state simulators. This design enables the quick removal of the entire module without causing harm to the cells or equipment.

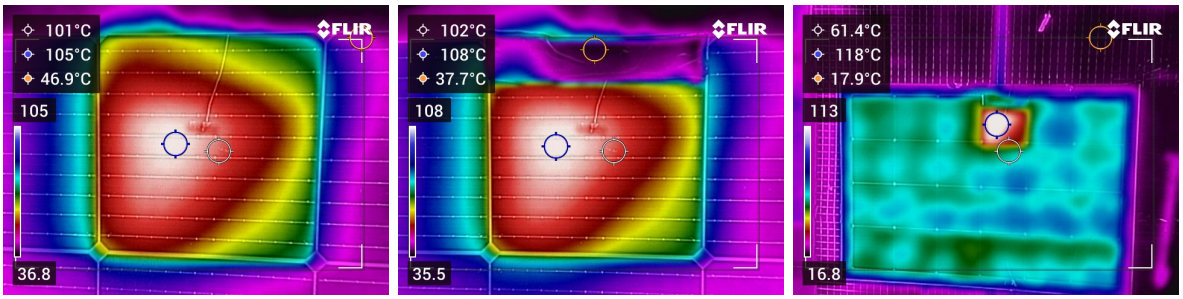

(a) (b) (c)

Figure 6.34: 18-cell Series at 20 percent shading: (a) Uncovered, (b) Covered, (c) Wide View of Module with maximum temperature of 118°C.

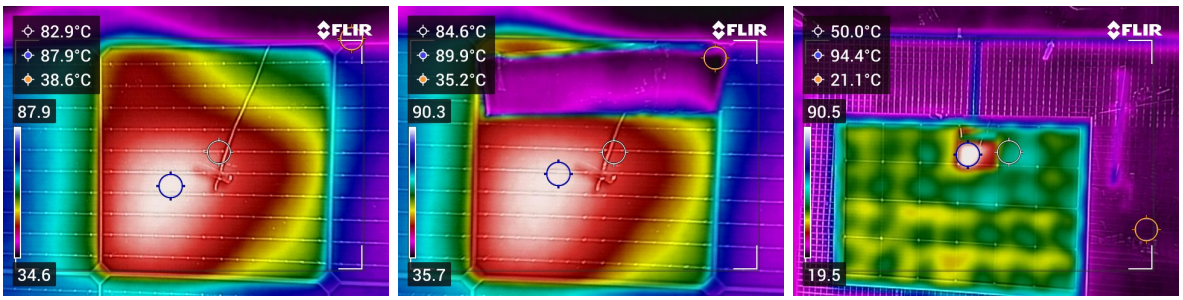

(a) (b) (c)

Figure 6.35: 18-cell Series at 25 percent shading: (a) Uncovered, (b) Covered, (c) Wide View of Module with maximum temperature of 94°C.

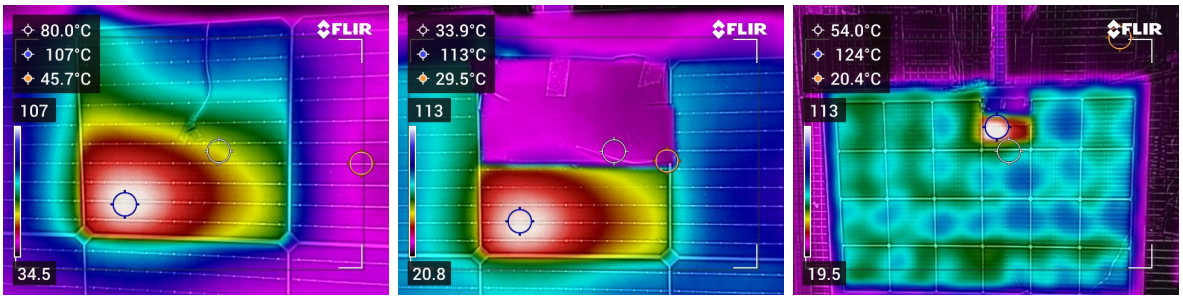

(a) (b) (c)

Figure 6.36: 18-cell Series at 50 percent shading: (a) Uncovered, (b) Covered, (c) Wide View of Module with maximum temperature of 124°C.

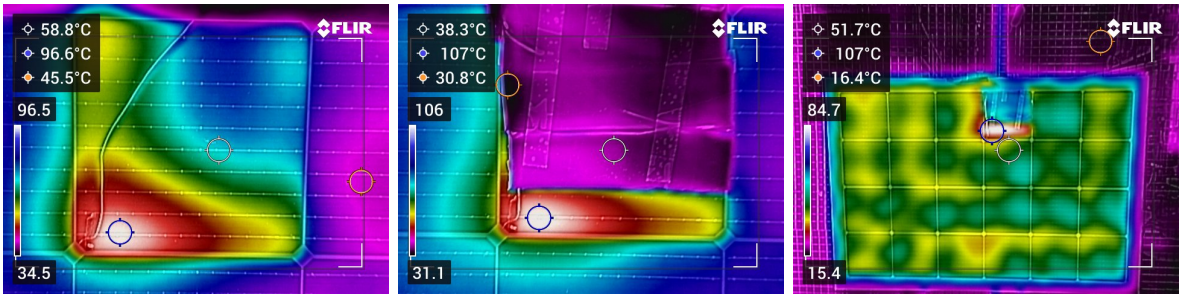

(a) (b) (c)

Figure 6.37: 18-cell Series at 75 percent shading: (a) Uncovered, (b) Covered, (c) Wide View of Module with maximum temperature of 107°C.

The hot-spot evaluation for the 18-string configuration revealed a maximum temperature (T1) of 134°C after 1-hour, described in Table 6.12. The thermocouple accurately monitored the temperature rise, while the IR camera reported lower readings. It approached the polymer front sheet's melting point but did not exceed the safety threshold of 160°C.

Table 6.12: Temperature vs time values measured for 18 cells at x=10 percent.

Time (Minutes)	Hot-spot temperature (T1) °C	Module Temperature (T2) °C
0.00	29.20	29.00
5.00	105.00	48.70
10.00	116.70	52.70
15.00	125.00	56.20
20.00	129.00	58.00
25.00	131.80	61.20
30.00	133.40	62.00
35.00	133.00	62.30
40.00	133.70	62.10
45.00	132.50	62.60
50.00	133.20	62.70
55.00	133.00	63.20
60.00	134.40	61.70

6.4.4. 24 cell string

In the industry, the use of a complete 24-cell strings is rare, even with the advantages of high power ratings and reduced bypass diode costs. The proximity of 18-cell setups to their operable limit suggests that the limit can be exceeded with 24 cells [85]. The primary goal is to terminate the experiment upon reaching the limit. Conversely, finding out the maximum temperature after surpassing 160°C is inconsequential, given that the desired objective has already been attained. As a result, the 24-cell string configurations did not pass the hot-spot endurance testing, aligning with the experiments. A possible explanation for the linear trend observed in Figure 6.38 is that in a series configuration, increasing the string length increases the voltage of the cells in reverse, thereby increasing the power dissipation in the cell. Refer chapter 7 for more explanation.

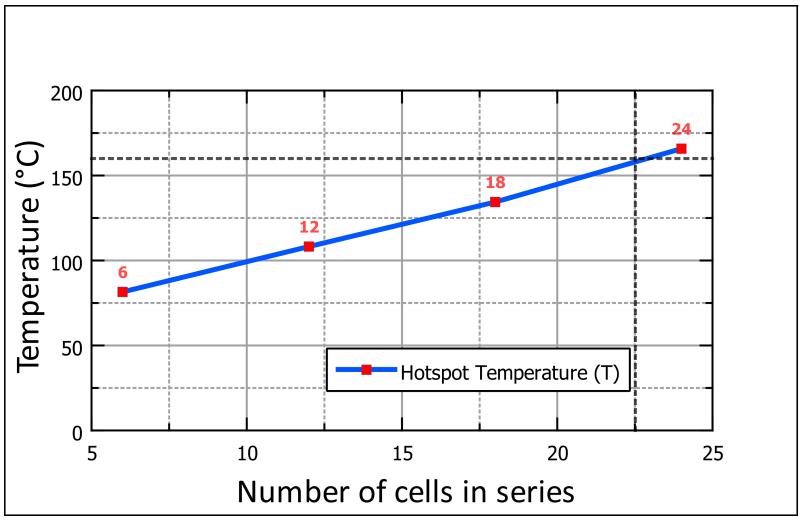

Figure 6.38: String length vs hot-spot temperature plot

The string length exceeds the safety threshold limit reaching a maximum hot-spot temperature 165.8°C with 24 cells in series. This observation was confirmed in section 4.3.5.

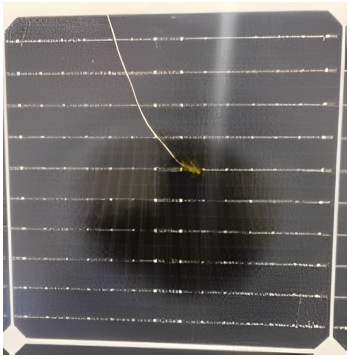

Figure 6.39: Visible damage was observed from melting of the front sheet, causing a large bubble in the center.

Two thermocouples play distinct roles: (T1) measures the hot-spot temperature, while (T2) tracks the ambient temperature around the module during accelerated indoor endurance testing. The temperature rapidly rose within the first 10 minutes and then exhibited slight fluctuations, attributed to natural convection around the module as shown in table 6.13.

Table 6.13: Temperature vs Time map monitored for every minute until temperature limit is reached.

Time (Minutes)	Hot-spot temperature (T1) °C	Module Temperature (T2) °C
0.00	32.00	32.00
1.00	70.00	35.00
2.00	107.00	37.00
3.00	125.00	38.00
4.00	136.00	39.40
5.00	142.20	41.90
6.00	149.40	42.40
7.00	153.00	42.80
8.00	155.00	42.80
9.00	158.20	43.00
10.00	160.60	44.00

After 10 minutes, the 24-cell string exceeded the 160°C limit, and the experiment was stopped to prevent module destruction. This decision was made considering that the actual maximum temperature is unknown, given the power dissipation, could potentially be even higher. The rest of the values were extrapolated as temperature stabilized providing an estimate, as shown in the plot 6.40. The observation of temperature stabilization over time in figures is consistent with the findings in [105].

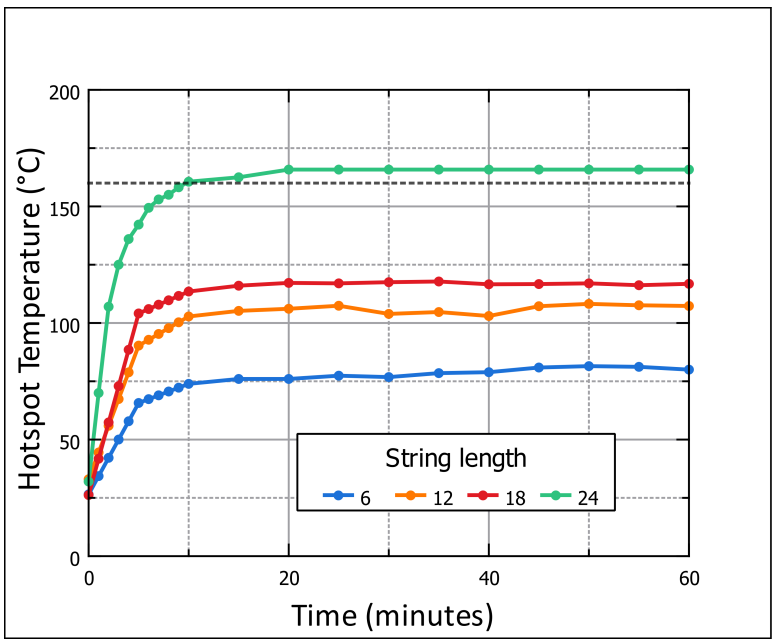

Figure 6.40: Temperature trend map vs time monitoring the maximum hot-spot temperature at shading rate (20 percent) shows thermal stability after 20 minutes.

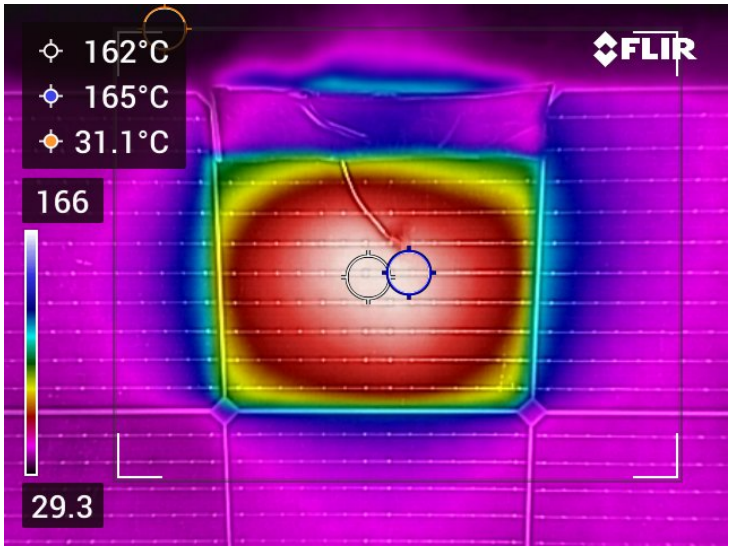

(a)

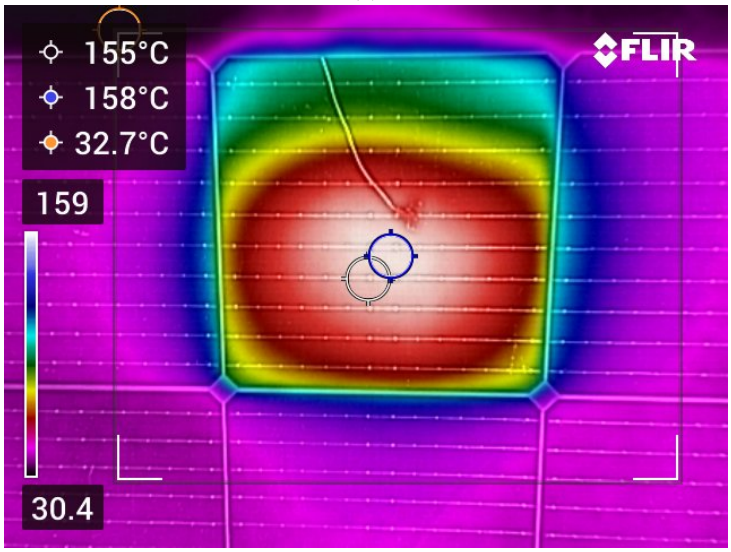

(b)

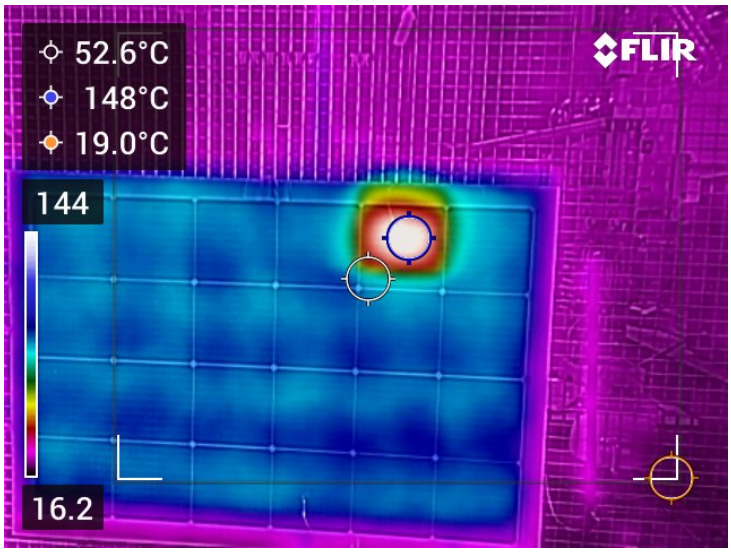

(c)

Figure 6.41: IR image of the hot-spot exceeding 165°C during 20 percent shading of a 24 cell module in series under short-circuit for 10 minutes (a) With cover (b) Without shading cover (c) Wide view of the module.

7 Conclusions & Recommendations

In this final chapter, the summary of the investigations culminates in a brief conclusion addresing the research objectives presented in section 7.1. Following this, a guideline for Solarge regarding the design criteria of hot-spots is proposed in section 7.2. The chapter ends with limitations encountered during the thesis in section 7.3 and future work for the readers to take away.

7.1. Summary

This thesis investigated the effects of partial shading on PV modules and shed light on the critical issue of hot-spot formation. Cell manufacturers, as mentioned in section 4.3, rarely provide information on their reverse characteristics. Determining the reverse operational point of a solar cell as a result becomes challenging. The effect of external factors such as temperature and illumination on cell-specific internal parameters adds to this complexity.

- How do the reverse bias characteristics of different cell technologies vary under different operating conditions ?.

  Simultaneously, understanding the reverse electrical processes that occur in these conditions, which drive the so-called "hot-spot effect," is critical, with Zener and Avalanche effects playing a key role. This influence is clear and obvious from the results presented in the section 6.1, which highlight distinct behaviors observed in IBC and PERC cells. A pivotal distinction between these breakdown processes is their underlying mechanisms—tunneling and carrier multiplication [72].

  This inherent dissimilarity is underscored by the magnitude of temperature coefficient (β) associated with the breakdown, providing a robust criterion for distinguishing between these two phenomena. Characterization performed on the IBC cell is consistent with the findings reported by the manufacturers, reporting a V_Z of around -5.2V [106]. Similarly, the PERC cells unveiled an interesting revelation of a V_{AB} around -19.6V in the dark, a value that has yet to be verified in relevant literature.

- What are the worst-case scenarios that lead to hot-spot formation in different cell technologies under partial shading?.

  The highest hot-spot temperature in a partially shaded cell almost always occurs in the illuminated region, as documented [85] and experimentally verified in chapter 6 . As stated in section 2.6.1, the shaded region has a lower voltage drop across the cell than the illuminated region. However, reverse current redistributes itself within the cell, taking the path of least resistance, which is usually provided by metal contacts since they are more conductive than silicon. Furthermore, the illuminated area encounters higher series resistance, and the local current density increases in this region, dissipating more power.

- What is the maximum number of cells that can be safely connected in series for different cell technologies under partial shading conditions to minimize the risk of hot-spot formation?.

  Another factor to consider is power dissipation. As indicated in table 6.9, at a string length of 12, it slightly surpasses 100 watts, initiating pre-breakdown characteristics as verified by literature. However, at string lengths 18–24, which are of interest to Solarge, permanent damage was observed in the PERC module for power values (P) exceeding 150-200 watts and heat flux ($\dot{Q}$) at 0.52-0.69 W/cm^2. This value of power (P) includes P_{illu}, P_{ph}, and P_{rev}. Moreover, power dissipation exhibited a linear relationship with the increasing string length [85], which also aligns with the findings in section 6.4.

  The ongoing discussion revolves around the validity of industry-established norms for severe shading ratios—specifically, 20% for full-cells and 40% for half-cut cells truly correspond to the conditions that there is maximum power dissipation P(x) and why this non-linearity occurs at that specific rate discussed in section 4.3.2. The incorporation of bypass diodes provides a plausible explanation for the observed trend. In practice, the string's topology with bypass diodes further complicates this task of finding out which cell is most likely to exhibit hot-spotting. The optimization of the string's operation point (MPP) constantly fluctuates leading to power dissipation among cells in an unpredictable order [84].

- What methods can be used to predict the formation and occurrence of hot-spots in specific locations, and which parameters are considered to characterize hot-spots?.

  Hence, the task of identifying the worst-performing cell proves more intricate than initially assumed. A precise methodology that employs inspections techniques like EL and IR for this selection, based on electrical performance within the string, still remains elusive. This challenge stems from the homogeneity of cells within the same batch, where subtle differences are difficult to measure and validate due to device sensitivity and changing ambient conditions, presenting a limitation in this thesis mentioned in section 4.4.1.

7.2. Guidelines for Solarge

It is critical for Solarge, a lightweight polymer-based module manufacturer, to assess the impact of using low-temperature lamination techniques on the front sheet and encapsulation. These processing steps closely match the operating temperature of the cell during hot-spot conditions. Furthermore, polymer modules face increased hot-spot risks due to the adhesion of shading elements like soiling and bird droppings on their front sheets. These modules may require improved thermal robustness and frequent field inspections to ensure long-term operational efficiency.

- What design approaches can be used to reduce the risk of hot-spots in polymer-based solar modules and ensure a hot-spot-resistant design?.

The results of section 6.4 highlight a critical observation that prolonged operation of Solarge modules using PERC cells with high breakdown limits can result in permanent damage. Moreover, breakdown limits vary by cell technology, and module manufacturers should consider them intuitively when establishing industry standards for maximum string length and wafer sizes. However, if Solarge manages to stay within the specified string length (S) of 18, the PERC full-cell polymer modules will most likely pass the hot-spot endurance test certification.

Given the rapid increase in wafer size across the industry, using half-cut cells is a safer alternative to using PERC M-10 full cells. Notably, half-cut cells have a lower hot-spot temperature than full cells and are more tolerant to shading which can result higher string lengths. Considering these advantages, investigating half-cut cells alongside testing can provide an interesting option for further exploration.

Rather than focusing on string lengths, another approach is to reduce power dissipation by lowering the breakdown voltage of the cells. Moreover, it has been observed that IBC cells are able to limit breakdown much earlier than PERC cells, essentially reducing power dissipation. They are slightly more expensive than PERC, but they also provide a more controlled breakdown. Therefore, another recommendation is to use low breakdown voltage cells, which are very suitable for Solarge's polymer-based modules.

Another intriguing design consideration is the back-sheet temperatures, which have been observed to rise significantly on occasion. The Solarge module's white backsheet promotes bifacial characteristics, which are good for performance. Nonetheless, it is important to note that polymers have lower thermal conductivity than their glass counterparts. This characteristic causes them to retain more heat and become more prominent due to their reduced capacity to efficiently dissipate heat in localized regions, particularly in hot-spot situations.

7.3. Future work

The use of conventional IR thermography to image breakdown currents with a reverse bias of up to several volts and map the dark characteristics of solar cells has limitations. Due to silicon's high thermal conductivity, the thermal signals captured by IR cameras are generally weak, resulting in blurred images, and the spatial resolution achieved is frequently poor and in the millimeter range. To overcome these limitations, new techniques such as lock-in thermography (LIT) and dynamic lock-in thermography (DLIT) can be implemented. These methods can reveal subsurface defects and hidden material variations with improved spatial resolution by using an IR camera to capture thermal images while modulating heating or cooling of the object [65].

Accelerated endurance testing under STC does not reveal the true nature of the degradation, as the industry still relies on IV curve analysis to quantify losses at the module level. In practice, temperatures can rise significantly, deviating from STC conditions, and illumination levels can increase drastically for short intervals of time due to clouds, which can also lead to notable damage. Field research suggests that running these tests over a longer period of time and a wider range of shading configurations would provide more realistic insights into the effects of time and degradation. More about long-term hot-spots is discussed in the appendix A.1.

Another limitation worth noting is the lack of in-depth analysis in IV characterization results, particularly when examining the shading orientation of cell electrical properties such as R_{sh} and R_S were not investigated due to device constraints. This is due to the inherent limitations of the IV tracer software Enlitech, which employs a 1-D model that excludes other non-idealities. The incorporation of Zener and avalanche carrier multiplication equations within the bishop model, as discussed in section 3.3.1, can theoretically simulate the curves that determine the operating point of a cell in reverse. This can validate experimental findings and conclusively to correlate with existing literature.

References

[1] B. Iqbal, A. Nasir, and A. F. Murtaza, "Stochastic maximum power point tracking of photovoltaic energy system under partial shading conditions," Protection and Control of Modern Power Systems, vol. 6, no. 1, 2021. DOI: 10.1186/s41601-021-00208-9.

[2] I. Geisemeyer, F. Fertig, W. Warta, S. Rein, and M. Schubert, "Prediction of silicon pv module temperature for hot spots and worst case partial shading situations using spatially resolved lock-in thermography," Solar Energy Materials and Solar Cells, vol. 120, pp. 259–269, Jan. 2014. DOI: 10.1016/j.solmat.2013.09.016.

[3] C. A. Belhadj, I. H. Banat, and M. Deriche, "A detailed analysis of photovoltaic panel hot spot phenomena based on the bishop model," pp. 222–227, 2017. DOI: 10.1109/SSD.2017.8166924.

[4] M. Aghaei, A. Fairbrother, A. Gok, et al., "Review of degradation and failure phenomena in photovoltaic modules," Renewable and Sustainable Energy Reviews, vol. 159, p. 112 160, 2022, ISSN: 1364-0321. DOI: https://doi.org/10.1016/j.rser.2022.112160.

[5] M. Owen-Bellini, P. Hacke, D. C. Miller, et al., "Advancing reliability assessments of photovoltaic modules and materials using combined-accelerated stress testing," Progress in Photovoltaics: Research and Applications, vol. 29, no. 1, pp. 64–82, 2021. DOI: https://doi.org/10.1002/pip.3342.

[6] NUS Singapore. (2023), [Online]. Available: https://www.seris.nus.edu.sg/services/Thermographic-Analysis-of-PV-Systems.html.

[7] Solarge. (2022), [Online]. Available: https://solarge.com/duurzaamheid.

[8] M.-J. Park, S. Youn, K. Jeon, S. H. Lee, and C. Jeong, "Optimization of shingled-type lightweight glass-free solar modules for building integrated photovoltaics," Applied Sciences, vol. 12, no. 10, 2022, ISSN: 2076-3417. DOI: 10.3390/app12105011.

[9] Solarge. (2018), [Online]. Available: https://solarge.com/over-solarge.

[10] S. Deng, Z. Zhang, C. Ju, et al., "Research on hot spot risk for high-efficiency solar module," Energy Procedia, vol. 130, pp. 77–86, 2017, Proceedings of the SNEC 11th International Photovoltaic Power Generation Conference & Exhibition, SNEC 2017 Scientific Conference, ISSN: 1876-6102. DOI: https://doi.org/10.1016/j.egypro.2017.09.399.

[11] P. Manganiello, M. Balato, and M. Vitelli, "A survey on mismatching and aging of pv modules: The closed loop," IEEE Transactions on Industrial Electronics, vol. 62, pp. 7276–7286, 2015. DOI: 10.1109/TIE.2015.2418731.

[12] J. K. Mathew, J. Kuitche, and G. TamizhMani, "Test-to-failure of pv modules: Hot-spot testing," pp. 002 839–002 843, 2010. DOI: 10.1109/PVSC.2010.5616895.

[13] R. Moretón, E. Lorenzo, and L. Narvarte, "Experimental observations on hot-spots and derived acceptance/rejection criteria," Solar Energy, vol. 118, pp. 28–40, 2015, ISSN: 0038-092X. DOI: https://doi.org/10.1016/j.solener.2015.05.009.

[14] O. Breitenstein, J. Bauer, K. Bothe, et al., "Understanding junction breakdown in multicrystalline solar cells," Journal of Applied Physics, vol. 109, no. 7, p. 071 101, 2011. DOI: 10.1063/1.3562200.

[15] W. Ahmed, M. U. Ali, S. J. Hussain, A. Zafar, and S. A. Hasani, "Visual vocabulary based photovoltaic health monitoring system using infrared thermography," IEEE Access, vol. 10, pp. 14 409–14 417, 2022. DOI: 10.1109/ACCESS.2022.3148138.

[16] D. C. Jordan, T. J. Silverman, J. H. Wohlgemuth, S. R. Kurtz, and K. T. VanSant, "Photovoltaic failure and degradation modes," Progress in Photovoltaics: Research and Applications, vol. 25, no. 4, pp. 318–326, 2017. DOI: https://doi.org/10.1002/pip.2866.

[17] Y. Tao and A. Rohatgi, High Efficiency Front Junction n Type Crystalline Silicon Solar Cells. Feb. 2017, ISBN: 978-953-51-2935-6. DOI: 10.5772/65023.

[18] K. Chethan, S. Jayaraman, K. Kumar, and K. Sivaji, "Sustainable forest management techniques," Mar. 2012. DOI: 10.5772/35823.

[19] A. M. Humada, M. Hojabri, S. Mekhilef, and H. M. Hamada, "Solar cell parameters extraction based on single and double-diode models: A review," Renewable and Sustainable Energy Reviews, vol. 56, pp. 494–509, 2016, ISSN: 1364-0321. DOI: https://doi.org/10.1016/j.rser.2015.11.051.

[20] E. Batzelis, "Non-iterative methods for the extraction of the single-diode model parameters of photovoltaic modules: A review and comparative assessment," Energies, vol. 12, no. 3, 2019, ISSN: 1996-1073. DOI: 10.3390/en12030358.

[21] M. de Blas, J. Torres, E. Prieto, and A. García, "Selecting a suitable model for characterizing photovoltaic devices," Renewable Energy, vol. 25, no. 3, pp. 371–380, 2002, ISSN: 0960-1481. DOI: https://doi.org/10.1016/S0960-1481(01)00056-8.

[22] C. Honsberg and S. Bowden. "Double diode model," PVEducation. (2023), [Online]. Available: https://www.pveducation.org/pvcdrom/characterisation/double-diode-model.

[23] O. Breitenstein, J. P. Rakotoniaina, M. H. Al Rifai, and M. Werner, "Shunt types in crystalline silicon solar cells," Progress in Photovoltaics: Research and Applications, vol. 12, no. 7, pp. 529–538, 2004. DOI: https://doi.org/10.1002/pip.544.

[24] O. Breitenstein and S. Rißland, "A two-diode model regarding the distributed series resistance," Solar Energy Materials and Solar Cells, vol. 110, pp. 77–86, 2013, ISSN: 0927-0248. DOI: https://doi.org/10.1016/j.solmat.2012.11.021.

[25] K. Bouzidi, M. Chegaar, and A. Bouhemadou, "Solar cells parameters evaluation considering the series and shunt resistance," Solar Energy Materials and Solar Cells, vol. 91, no. 18, pp. 1647–1651, 2007, ISSN: 0927-0248. DOI: https://doi.org/10.1016/j.solmat.2007.05.019.

[26] F. Lindholm, J. Fossum, and E. Burgess, "Application of the superposition principle to solar-cell analysis," IEEE Transactions on Electron Devices, vol. 26, no. 3, 165–171, 1979, ISSN: 0018-9383.

[27] S. Mahadevan, S. M. Hardas, and G. Suryan, "Electrical breakdown in semiconductors," physica status solidi (a), vol. 8, no. 2, pp. 335–374, 1971. DOI: https://doi.org/10.1002/pssa.2210080202.

[28] A. Smets, K. Jäger, O. Isabella, R. van Swaaij, and M. Zeman, Solar Energy: The physics and engineering of photovoltaic conversion, technologies and systems, English. UIT Cambridge Limited, 2016, ISBN: 978-1-906860-32-5.

[29] M. A. Green, "Solar cell fill factors: General graph and empirical expressions," Solid-State Electronics, vol. 24, pp. 788–789, 1981, <br />, ISSN: 00381101. DOI: 10.1016/0038-1101(81)90062-9.

[30] W. Storr. "I-v characteristic curves or current-voltage curves," Basic Electronics Tutorials. (Aug. 2022), [Online]. Available: https://www.electronics-tutorials.ws/blog/i-v-characteristic-curves.html.

[31] C. Honsberg and S. Bowden. "Double diode model," PVEducation. (2023), [Online]. Available: https://www.pveducation.org/pvcdrom/characterisation/dark-iv-measurements.

[32] D. King, B. Hansen, J. Kratochvil, and M. Quintana, "Dark current-voltage measurements on photovoltaic modules as a diagnostic or manufacturing tool," in Conference Record of the Twenty Sixth IEEE Photovoltaic Specialists Conference - 1997, 1997, pp. 1125–1128. DOI: 10.1109/PVSC.1997.654286.

[33] C. Honsberg and S. Bowden. "Mismatch for cells connected in series," PVEducation. (2023), [Online]. Available: https://www.pveducation.org/pvcdrom/modules-and-arrays/mismatch-for-cells-connected-in-series.

[34] C. Honsberg and S. Bowden. "Mismatch for cells connected in parallel," PVEducation. (2023), [Online]. Available: https://www.pveducation.org/pvcdrom/modules-and-arrays/mismatch-for-cells-connected-in-parallel.

[35] A. E. Tutorials. "Solar cell i-v characteristic and the solar cell i-v curve," Alternative Energy Tutorials. (2016), [Online]. Available: https://www.alternative-energy-tutorials.com/photovoltaics/solar-cell-i-v-characteristic.html.

[36] C. Honsberg and S. Bowden. "Effect of temperature," PVEducation. (2023), [Online]. Available: https://www.pveducation.org/pvcdrom/solar-cell-operation/effect-of-temperature.

[37] Seaward. (2023), [Online]. Available: https://www.seaward.com/gb/support/solar/faqs/00797-how-does-temperature-and-irradiance-affect-i-v-curves/.

[38] W. Bludau, A. Onton, and W. Heinke, "Temperature dependence of the band gap of silicon," Journal of Applied Physics, vol. 45, no. 4, pp. 1846–1848, Oct. 2003, ISSN: 0021-8979. DOI: 10.1063/1.1663501.

[39] J. Bishop, "Microplasma breakdown and hot-spots in silicon solar cells," Solar Cells, vol. 26, no. 4, pp. 335–349, 1989, ISSN: 0379-6787. DOI: https://doi.org/10.1016/0379-6787(89)90093-8.

[40] "Improved pv module performance under partial shading conditions," Energy Procedia, vol. 33, pp. 248–255, 2013, PV Asia Pacific Conference 2012, ISSN: 1876-6102. DOI: https://doi.org/10.1016/j.egypro.2013.05.065.

[41] "Solar cell busbars, fingers, tab wires and bus wires," DS energy. (2019), [Online]. Available: https://www.dsneg.com/info/solar-cell-busbars-fingers-tab-wires-and-bus-39808254.html.

[42] A. Atia, F. Anayi, and G. Min, "Comparing shading with irradiance reduction effects on solar cells electrical parameters," Aug. 2021, pp. 1–5. DOI: 10.1109/UPEC50034.2021.9548160.

[43] M. Chegaar, A. Hamzaoui, A. Namoda, P. Petit, M. Aillerie, and A. Herguth, "Effect of illumination intensity on solar cells parameters," Energy Procedia, vol. 36, pp. 722–729, 2013, TerraGreen 13 International Conference 2013 - Advancements in Renewable Energy and Clean Environment, ISSN: 1876-6102. DOI: https://doi.org/10.1016/j.egypro.2013.07.084.

[44] C. E. Clement, J. P. Singh, E. Birgersson, Y. Wang, and Y. S. Khoo, "Illumination dependence of reverse leakage current in silicon solar cells," IEEE Journal of Photovoltaics, vol. 11, no. 5, pp. 1285–1290, 2021. DOI: 10.1109/JPHOTOV.2021.3088005.

[45] M. Alonso-García and J. Ruíz, "Analysis and modelling the reverse characteristic of photovoltaic cells," Solar Energy Materials and Solar Cells, vol. 90, no. 7, pp. 1105–1120, 2006, ISSN: 0927-0248. DOI: https://doi.org/10.1016/j.solmat.2005.06.006.

[46] RENA. "Wafer wet chemical surface treatment from m0 to m6 & m12." (2022), [Online]. Available: https://www.rena.com/en/products/large-wafer-wet-processing.

[47] Solar Magazine. (Mar. 2022), [Online]. Available: https://solarmagazine.com/solar-panels/perc-solar-panels/.

[48] A. Halm, V. Mihailetchi, G. Galbiati, et al., "The zebra cell concept – large area n-type interdigitated back contact solar cells and one-cell modules fabricated using standard industrial processing equipment," Sep. 2012. [Online]. Available: https://www.researchgate.net/publication/257415342_The_Zebra_Cell_Concept_-_large_Area_n-type_Interdigitated_Back_Contact_Solar_Cells_and_One-Cell_Modules_Fabricated_Using_Standard_Industrial_Processing_Equipment.

[49] "Perc cell," AZO Materials. (May 2022), [Online]. Available: https://www.azom.com/article.aspx?ArticleID=16715.

[50] M. Dahlinger, B. Bazer-Bachi, T. Röder, J. Köhler, R. Zapf-Gottwick, and J. Werner, "22.0 percent efficient laser doped back contact solar cells," Energy Procedia, vol. 38, pp. 250–253, Dec. 2013. DOI: 10.1016/j.egypro.2013.07.274.

[51] "182mm 10bb bifacial mono perc cell," ENF Solar. (2023), [Online]. Available: https://www.enfsolar.com/pv/cell-datasheet/2925.

[52] DMEGC Solar. (2019), [Online]. Available: https://www.dmegc.solar/files/bestanden/datasheets/G1-DMBD5B159-223-116SE-201908.pdf.

[53] "Spic solar ibc cell," SPIC. (2023), [Online]. Available: http://en.spicsolar.com/default/products/18.html.

[54] "Ibc cell technology," Maxeon. (2020), [Online]. Available: https://investors.sunpower.com/static-files/7781756b-af57-4be6-bbe0-5ee06e098886.

[55] "Isc cell technology," ISC. (2020), [Online]. Available: https://isc-konstanz.de/en/isc-cell-technology/.

[56] "All about high efficiency solar cells: Perc and half cut," GSES. (Apr. 2021), [Online]. Available: https://www.gses.com.au/high-efficiency-cells-perc-and-half-cut/.

[57] D. D. Rooij. "Half cut solar cells: New standard in product differentiation?" (Mar. 2023), [Online]. Available: https://sinovoltaics.com/solar-cells/half-cut-solar-cells-the-new-standard/.

[58] F. Kaule, M. Pander, M. Turek, M. Grimm, E. Hofmueller, and S. Schoenfelder, "Mechanical damage of half-cell cutting technologies in solar cells and module laminates," AIP Conference Proceedings, vol. 1999, no. 1, Aug. 2018, 020013, ISSN: 0094-243X. DOI: 10.1063/1.5049252.

[59] "An overview - advantages of half cut cells photovoltaic solar panels," Voltacon Power conversion. (Dec. 2020), [Online]. Available: https://voltaconsolar.com/blog/2020/11/28/advantages-of-half-cut-cells-photovoltaic-solar-panels/.

[60] K. Bothe, K. Ramspeck, D. Hinken, et al., "Luminescence emission from forward- and reverse-biased multicrystalline silicon solar cells," Journal of Applied Physics, vol. 106, no. 10, p. 104 510, Nov. 2009, ISSN: 0021-8979. DOI: 10.1063/1.3256199.

[61] J. Qian, A. Thomson, M. Ernst, and A. Blakers, "Two-dimensional hot spot temperature simulation for c-si photovoltaic modules," physica status solidi (a), vol. 215, no. 21, p. 1 800 429, 2018. DOI: https://doi.org/10.1002/pssa.201800429.

[62] G. Notton, C. Cristofari, M. Mattei, and P. Poggi, "Modelling of a double-glass photovoltaic module using finite differences," Applied Thermal Engineering, vol. 25, no. 17, pp. 2854–2877, 2005, ISSN: 1359-4311. DOI: https://doi.org/10.1016/j.applthermaleng.2005.02.008.

[63] T. Xu, S. Deng, G. Zhang, and Z. Zhang, "Research on hot spot risk of high wattage solar modules," Solar Energy, vol. 230, pp. 583–590, 2021, ISSN: 0038-092X. DOI: https://doi.org/10.1016/j.solener.2021.10.037.

[64] M. Singh Tyagi, "Zener and avalanche breakdown in silicon alloyed p-n junctions—i: Analysis of reverse characteristics," Solid-State Electronics, vol. 11, no. 1, pp. 99–115, 1968, ISSN: 0038-1101. DOI: https://doi.org/10.1016/0038-1101(68)90141-X.

[65] O. Breitenstein, "Understanding the current-voltage characteristics of industrial crystalline silicon solar cells by considering inhomogeneous current distributions," Opto-Electronics Review, vol. 21, no. 3, pp. 259–282, Jan. 2013. DOI: 10.2478/s11772-013-0095-5.

[66] C. E. C. CLEMENT, The design of hot-spot resistant shingled photovoltaic modules, 2021. [Online]. Available: https://scholarbank.nus.edu.sg/handle/10635/214504.

[67] E. Meyer and E. Ernest van Dyk, "The effect of reduced shunt resistance and shading on photovoltaic module performance," in Conference Record of the Thirty-first IEEE Photovoltaic Specialists Conference, 2005., 2005, pp. 1331–1334. DOI: 10.1109/PVSC.2005.1488387.

[68] G. Sahin, "Effect of temperature on the series and shunt resistance of a silicon solar cell under frequency modulation," Journal of Basic and Applied Physics, vol. 5, pp. 21–29, Dec. 2016. DOI: 10.5963/JBAP0501003.

[69] M. El-Saba, Fundamentals of Electronic Devices & Circuits (from A to Z). Jan. 2010, pp. 50–121.

[70] K. M. Gupta and N. Gupta, Advanced Semiconducting Materials And Devices. Springer International Publishing, 2016.

[71] T. Kemmer, J. M. Greulich, A. Krieg, and S. Rein, "Current-voltage characteristics of silicon solar cells: Determination of base doping concentration and hysteresis correction," Solar Energy Materials and Solar Cells, vol. 248, p. 111 953, 2022, ISSN: 0927-0248. DOI: https://doi.org/10.1016/j.solmat.2022.111953.

[72] N. Klein, "Electrical breakdown in solids," in ser. Advances in Electronics and Electron Physics, L. Marton, Ed., vol. 26, Academic Press, 1969, pp. 309–424. DOI: https://doi.org/10.1016/S0065-2539(08)60985-3.

[73] E. Kam-Lum, A. Brooks, D. Cormode, and A. Cronin, "Effect of solar cells reverse biased voltage on pv modules partial shade performance," Feb. 2016.

[74] H. Chu, L. J. Koduvelikulathu, V. D. Mihailetchi, G. Galbiati, A. Halm, and R. Kopecek, "Soft breakdown behavior of interdigitated-back-contact silicon solar cells," Energy Procedia, vol. 77, pp. 29–35, 2015, 5th International Conference on Silicon Photovoltaics, SiliconPV 2015, ISSN: 1876-6102. DOI: https://doi.org/10.1016/j.egypro.2015.07.006.

[75] K. G. McKay, "Avalanche breakdown in silicon," Phys. Rev., vol. 94, pp. 877–884, 4 May 1954. DOI: 10.1103/PhysRev.94.877.

[76] C. Lopez Pineda, "Experimental evaluation of reverse bias stress induced on photovoltaic modules for different configurations," Solar& Wind Technology, vol. 3, no. 2, pp. 85–88, 1986, ISSN: 0741-983X. DOI: https://doi.org/10.1016/0741-983X(86)90018-4.

[77] J. Bauer, J.-M. Wagner, A. Lotnyk, et al., "Hot spots in multicrystalline silicon solar cells: Avalanche breakdown due to etch pits," physica status solidi (RRL) – Rapid Research Letters, vol. 3, no. 2-3, pp. 40–42, 2009. DOI: https://doi.org/10.1002/pssr.200802250.

[78] J.-M. Wagner, J. Bauer, and O. Breitenstein, "Classification of pre-breakdown phenomena in multicrystalline silicon solar cells," Sep. 2009. DOI: 10.4229/24thEUPVSEC2009-2AO.1.5.

[79] S. Kasap, "Elementary quantum physics," in Principles of electronic materials and Devices, 4th ed. McGraw Hill Education, 2018, p. 564.

[80] D. Neamen, Semiconductor Physics And Devices (McGraw-Hill Series in Electrical and Computer Engineering). McGraw-Hill Education, 2003, p. 259, ISBN: 9780072321074. [Online]. Available: https://books.google.nl/books?id=9oEifMuMAVsC.

[81] M. K. Saini. "Difference between avalanche breakdown and zener breakdown," Tutorials Point. (Sep. 2022), [Online]. Available: https://www.tutorialspoint.com/difference-between-avalanche-breakdown-and-zener-breakdown#.

[82] "Standard test method for hot spot protection testing of photovoltaic modules," ASTM International - Standards Worldwide, Jun. 2018. [Online]. Available: https://v1backup.astm.org/Standards/E2481.htm.

[83] W. Herrmann, W. Wiesner, and W. Vaassen, "Hot spot investigations on pv modules-new concepts for a test standard and consequences for module design with respect to bypass diodes," in Conference Record of the Twenty Sixth IEEE Photovoltaic Specialists Conference - 1997, 1997, pp. 1129–1132. DOI: 10.1109/PVSC.1997.654287.

[84] E. Bende, N. Dekker, and M. Jansen, "Performance and safety aspects of pv modules under partial shading: A simulation study," Sep. 2014. DOI: 10.13140/2.1.1569.6640.

[85] Q. Zhang and Q. Li, "Temperature and reverse voltage across a partially shaded si pv cell under hot spot test condition," in 2012 38th IEEE Photovoltaic Specialists Conference, 2012, pp. 001 344–001 347. DOI: 10.1109/PVSC.2012.6317849.

[86] K. A. Kim and P. T. Krein, "Photovoltaic hot spot analysis for cells with various reverse-bias characteristics through electrical and thermal simulation," in 2013 IEEE 14th Workshop on Control and Modeling for Power Electronics (COMPEL), 2013, pp. 1–8. DOI: 10.1109/COMPEL.2013.6626399.

[87] J. Wohlgemuth and W. Herrmann, "Hot spot tests for crystalline silicon modules," in Conference Record of the Thirty-first IEEE Photovoltaic Specialists Conference, 2005., 2005, pp. 1062–1063. DOI: 10.1109/PVSC.2005.1488317.

[88] E. J. Wolf, I. E. Gould, L. B. Bliss, J. J. Berry, and M. D. McGehee, "Designing modules to prevent reverse bias degradation in perovskite solar cells when partial shading occurs," Solar RRL, vol. 6, no. 3, p. 2 100 239, 2022. DOI: https://doi.org/10.1002/solr.202100239.

[89] M. Dhimish, V. Holmes, P. Mather, and M. Sibley, "Novel hot spot mitigation technique to enhance photovoltaic solar panels output power performance," Solar Energy Materials and Solar Cells, vol. 179, pp. 72–79, 2018, ISSN: 0927-0248. DOI: https://doi.org/10.1016/j.solmat.2018.02.019.

[90] Y. Wang, K. Itako, T. Kudoh, K. Koh, and Q. Ge, "Voltage-based hot-spot detection method for pv string using projector," in 2016 IEEE International Conference on Power and Renewable Energy (ICPRE), 2016, pp. 570–574. DOI: 10.1109/ICPRE.2016.7871140.

[91] Tektronix. "Keithley smu 2650 series high power sourcemeter®," Keithley. (2023), [Online]. Available: https://www.tek.com/en/products/keithley/source-measure-units/2650-series-high-power-sourcemeter.

[92] G. Goudelis, P. I. Lazaridis, and M. Dhimish, "A review of models for photovoltaic crack and hotspot prediction," Energies, vol. 15, no. 12, 2022, ISSN: 1996-1073. DOI: 10.3390/en15124303.

[93] R. Moretón, E. Lorenzo, and L. Narvarte, "Experimental observations on hot-spots and derived acceptance/rejection criteria," Solar Energy, vol. 118, pp. 28–40, 2015.

[94] "Flir c3-x compact thermal camera with cloud connectivity and wi-fi | teledyne flir," FLIR. (2023), [Online]. Available: https://www.flir.com/products/c3-x/.

[95] U. Jahn and M. Herz. "Review on ir and el imaging for pv field applications - iea-pvps," IEA. (Mar. 2018), [Online]. Available: https://iea-pvps.org/key-topics/review-on-ir-and-el-imaging-for-pv-field-applications/.

[96] Y. Jia, Y. Wang, X. Hu, et al., "Diagnosing breakdown mechanisms in monocrystalline silicon solar cells via electroluminescence imaging," Solar Energy, vol. 225, pp. 463–470, 2021, ISSN: 0038-092X. DOI: https://doi.org/10.1016/j.solener.2021.07.052.

[97] T. Fuyuki and A. Kitiyanan, Photographic diagnosis of crystalline silicon solar cells utilizing electroluminescence, Jul. 2009. DOI: 10.1007/S00339-008-4986-0.

[98] "Fluke 87v industrial multimeter," FLUKE. (2023), [Online]. Available: https://www.fluke.com/en-us/product/electrical-testing/digital-multimeters/fluke-87v.

[99] C. Electronic. "Voltcraft PL-125-T2 Thermometer -200 - +1372 °C Sensor Type K, J." (2020), [Online]. Available: https://www.conrad.com/p/voltcraft-pl-125-t2-thermometer-200-1372-c-sensor-type-k-j-1012836.

[100] Electrical Information. (Dec. 2022), [Online]. Available: https://electrical-information.com/zener-diode-temperature-coefficient/.

[101] "Are there any special considerations for the temperature coefficient of diodes?" Toshiba Electronic Devices Semiconductors. (2023), [Online]. Available: https://toshiba.semicon-storage.com/us/semiconductor/knowledge/faq/diode/are-there-any-special-considerations-for-the-temperature-coeffic.html.

[102] I. Newton. "Newton's law of cooling." (1701), [Online]. Available: https://en.wikipedia.org/wiki/Newton%27s_law_of_cooling.

[103] H. J. Solheim, H. G. Fjær, E. A. Sørheim, and S. E. Foss, "Measurement and simulation of hot spots in solar cells," Energy Procedia, vol. 38, pp. 183–189, 2013, Proceedings of the 3rd International Conference on Crystalline Silicon Photovoltaics (SiliconPV 2013), ISSN: 1876-6102. DOI: https://doi.org/10.1016/j.egypro.2013.07.266.

[104] N. Balaji, M. C. Raval, and S. Saravanan, "Review on metallization in crystalline silicon solar cells," in Solar Cells, M. Nayeripour, M. Mansouri, and E. Waffenschmidt, Eds., Rijeka: IntechOpen, 2019, ch. 2. DOI: 10.5772/intechopen.84820.

[105] "Hotspot testing of glass/backsheet and glass/glass pv modules pre-stressed in extended thermal cycling," Solar Energy, vol. 249, pp. 467–475, 2023, ISSN: 0038-092X. DOI: https://doi.org/10.1016/j.solener.2022.12.006.

[106] A. Halm, V. Mihailetchi, G. Galbiati, et al., "The zebra cell concept – large area n-type interdigitated back contact solar cells and one-cell modules fabricated using standard industrial processing equipment," Sep. 2012.

[107] R. G. Vieira, F. M. U. de Araújo, M. Dhimish, and M. I. S. Guerra, "A comprehensive review on bypass diode application on photovoltaic modules," Energies, vol. 13, no. 10, 2020, ISSN: 1996-1073. [Online]. Available: https://www.mdpi.com/1996-1073/13/10/2472.

[108] M. Karimi, H. Samet, T. Ghanbari, and E. Moshksar, "A current based approach for hot-spot detection in photovoltaic strings," International Transactions on Electrical Energy Systems, vol. 30, no. 9, e12517, 2020. DOI: https://doi.org/10.1002/2050-7038.12517.

[109] M. D. Kelzenberg. "I-V software." (2015), [Online]. Available: https://mkelzenb.caltech.edu/software/IV/IV_help_web.html.

A Degradation

A.1. Long-term hot-spot scenario

During long-term operation, it is important to consider the potential consequences of temperature rise in bypassing devices used to mitigate the effects of shading. The cell continues to dissipate power, spreading heat throughout the panel undetected, until the diode turns on after the critical level of shading is reached. Bypass diodes do not help protect the panel from hot-spot risks as they consume part of the generated power by heating up [107]. Elevated temperatures in these devices can cause thermal cycling, inducing mechanical stresses on adjacent cells. This cyclic expansion and contraction can cause material fatigue, resulting in micro-cracks, de-lamination, discoloration, and increased degradation of cell components. Hot-spots have the potential to damage the junction box, which houses critical electrical connections and is located within the solar panel. Prolonged exposure to high temperatures periodically can degrade the materials in the junction box, leading to insulation breakdown, increased electrical resistance, compromised electrical performance, and long-term damage [108].

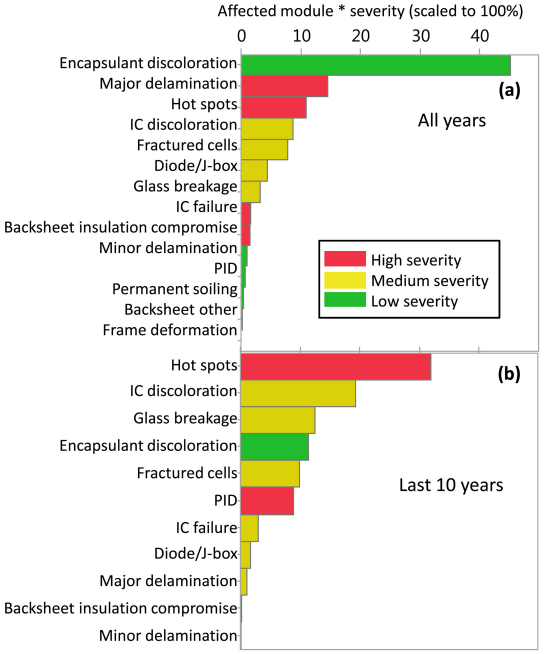

Figure A.1: Modules affected by a specific degradation modes shown in (a) Pareto chart for all years and (b) systems installed in the last 10 years with the bars color-coded by severity [16].

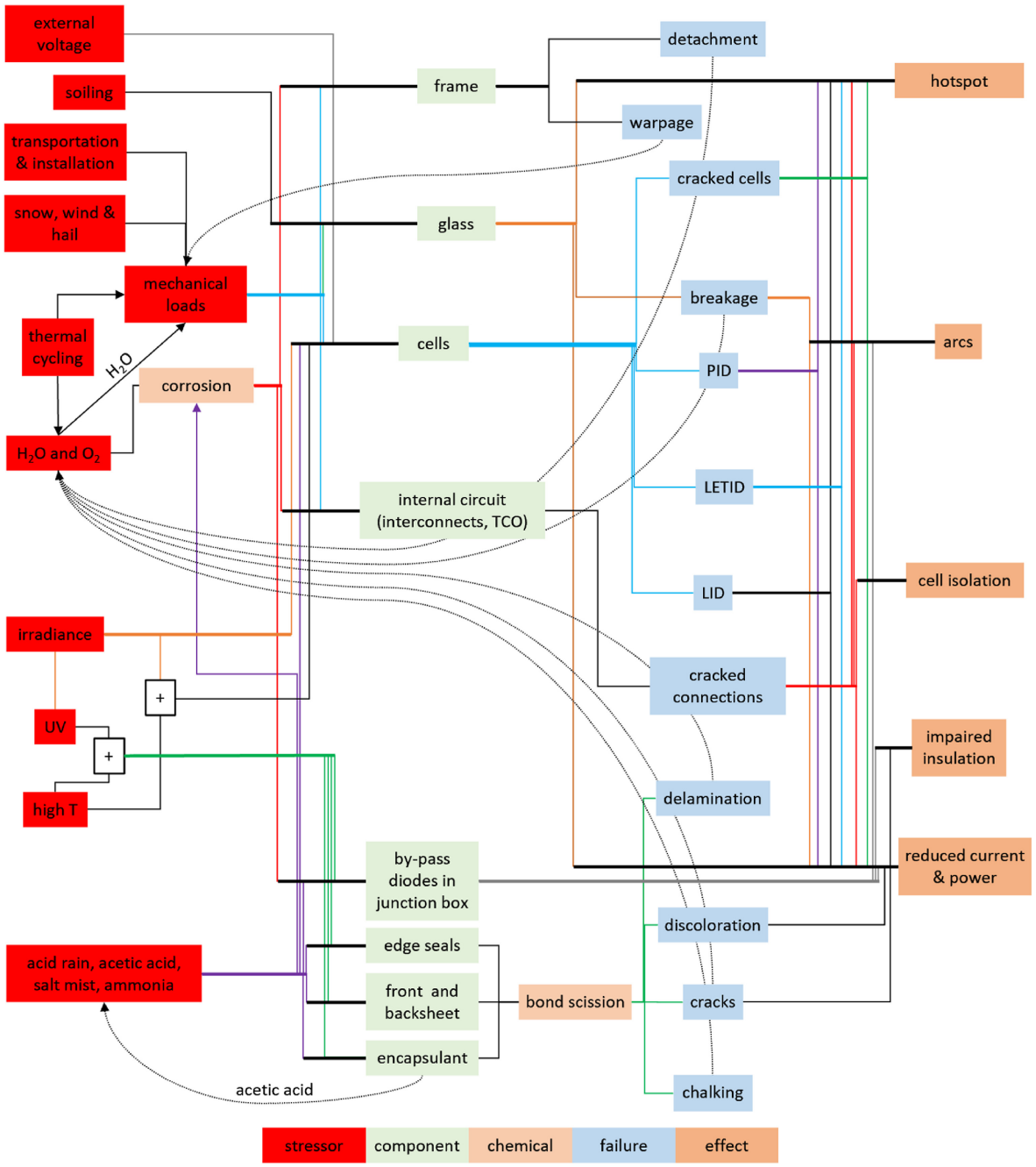

Figure A.2: An overview of all module degradations reveals potential relationships between stresses, components, and failure effects. Rare and unforeseen degradations, in the presence of other stresses, can result in more common and severe issues, leading to complete failure, depending on the dominant mechanism [4].

B
Datasheets

During the experiments, the Keithley 2651A SMU performs IV sweeps within specific ranges mentioned in table B.1. It's essential to consider the limitations of each cell technology pre-sweep. For a thorough sweep, the starting point of the current I_{sc} intercept on the y-axis should be below the current limit of the SMU. For instance, if the limit is 10 amps, an M-10 PERC cell with an I_{sc} of 13 amps cannot complete the sweep. To overcome this, we switch to 20 amps for the sweep, lowering the operating voltage of the device. In reverse sweeps, breakdown is achieved at -20V and beyond, so the voltage is switched to -40V to achieve accurate measurements. This constant, dynamic switching enables characterization of all the cells under different conditions.

Table B.1: Maximum Output Power and source/sink limits of the model 2651A

Power Specifications	
Four-quadrant source or sink operation	
Maximum - 202 W	
Voltage (V)	Current (I)
±10.1 V @ ±20.0 A	± 5.05 A @ ± 40 V
±20.2 V @ ±10.0 A	± 10.1 A @ ± 20 V
±40.4 V @ ± 5.0 A	± 20.2 A @ ± 10 V

The step voltage is an important parameter that impacts the smoothness of the curve, as longer step voltages do not accurately help plot the curve but rather extrapolate data points in straight lines. Too small, the step size is insufficient to complete a full sweep in the specified range. Hence, the step size must be chosen iteratively to sweep the IV curves.

Sweep delay, another value which is programmed into the SMU prior to sweep start, specifies the time between IV steps in a sweep. This setting specifically controls the time between changing the bias level and starting the reading(s). This delay is usually added to or merged with a default delay for each measurement range, depending on instrument configuration. The sweep delay determines the approximate minimum delay between successive measurements during DC-mode measurements and is not transmitted to the SMU as part of the measurement process [109]. Hysterisis in curves as discussed in section 3.3.3 can be eliminated by adjusting the delay based on how the solar cell responds to the conditions.

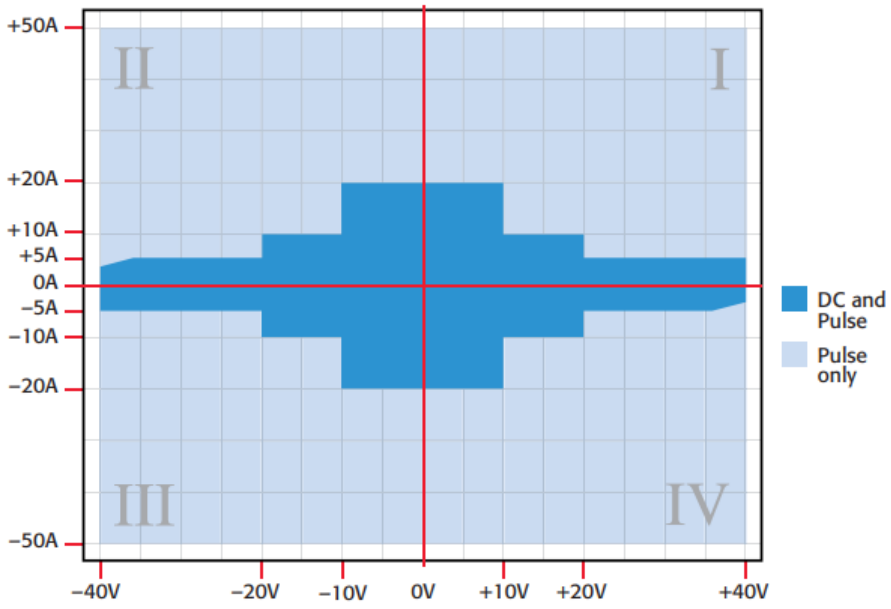

Figure B.1: The Model 2651A can source or sink up between the ranges of ±40V and ±50A across all four quadrants respectively [91].

C
RebEL Imaging

In practice, reverse-bias electro-luminescence (RebEL) imaging is performed at -0.1 V to investigate and map defects such as shunts in the dark. Strong ohmic shunts locally short-circuit the P-N junction [14]. But conventional low-reverse-bias EL imaging, a widely used method, proves inadequate for accurately detecting such issues because the electric field strength in these regions is not sufficiently high. However, around breakdown conditions, localized thermalization can be observed as bright spots. Thus, high-reverse-bias El imaging reveals an interesting heat pattern of the hot-spot which coincides with the IR images. In essence, mapping local dark current densities along breakdown sites with heat dissipation paths provides a new way of looking at characterizing hot-spot behavior in localized areas.

Silicon materials emit luminescence in the 1000–1200 nm range in forward bias as discussed in section 5.3.3, with a peak emission detected at 1150 nm due to the band gap. The camera used in this set-up can capture a mix of near-IR from 800-950 nm and light up to 1200 nm, resulting in a combination of these two. The hot-spot coincides with the pattern seen in the IR image, re-confirming what is seen is the heat signature produced by reverse current in the dark. Surprisingly, most EL cameras are unable to image this pattern because an IR filter eliminates these heat signatures. While intriguing, this technique is not always useful for characterizing hot-spots, as the conditions permanently damage the solar cell.

The figure C.1a depicts a violet EL image of a PERC cell with small dark marks indicating minor defects. In contrast, the high reverse bias EL image in figure C.1b has a distinct hot-spot with a 30-second shutter to capture and enhance the faint, reddish emissions. This observation supports the earlier assumption that the wavelengths of these emissions are different. The image also shows concentric circles of varying intensities, with the center having the highest temperature. This correlation was confirmed by cross-referencing with an IR camera.

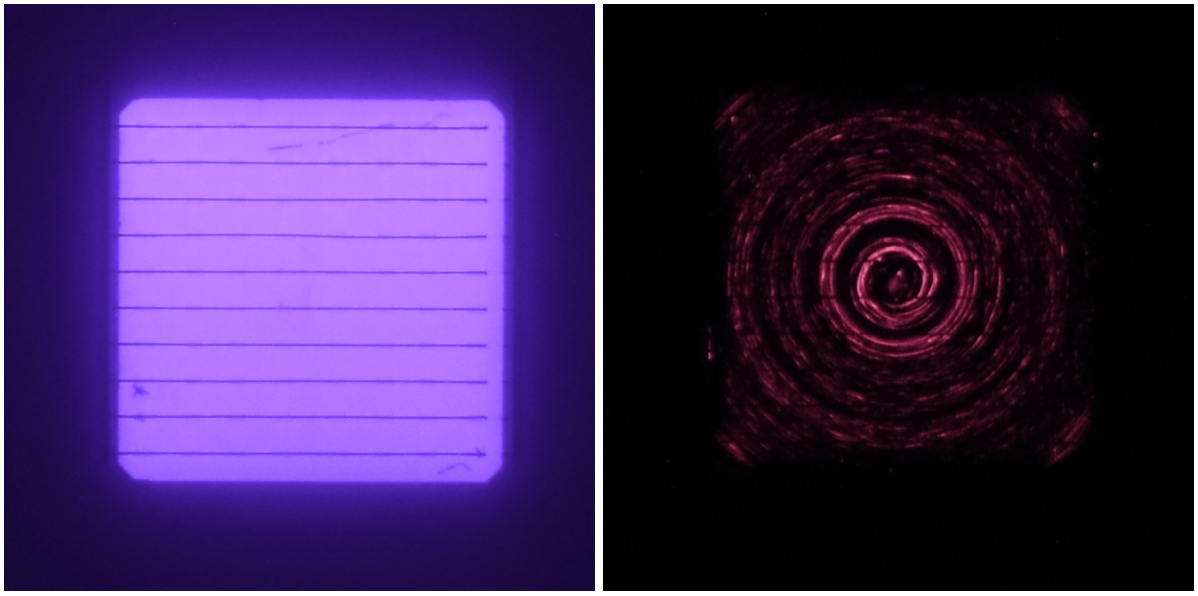

(a) (b)

Figure C.1: PERC M-10 full-cell: (a) EL image, (b) RebEL image of a hot-spot.

Figure C.2a depicts two or more PERC G1 full-cells cells in series connected with EL images depicting large cracks across one of the cells. Meanwhile, figure C.2b shows both the EL and RebEL side-by-side as they were connected in anti-parallel with one cell in forward and the other in reverse and figure C.2c are both in reverse. Finally, C.2d shows a string of three PERC G1 half-cut cells in series all in reverse. The first two cells display the expected half-circle hot-spot pattern seen in half-cut cells at the cut edge. However, the third cell is severely and permanently damaged, causing a short circuit that prevents it from producing a hot-spot. Instead, it emits a bright violet light similar to the EL image wavelengths.

Figure C.3 depicts a progressive arrangement of three and four cells connected in series, respectively, observed using the EL camera in both forward and reverse modes. The potential exploration of hot-spot patterns in relation to defects under the EL camera opens up novel opportunities for future research.

As previously discussed in section 6.3.3, the task of reverse biasing the entire series of cells with a DC power supply becomes progressively more challenging due to the cumulative effect of reverse-added breakdown voltages. This specific scenario was conducted solely for the duration of capturing this alluring image in figure C.4.

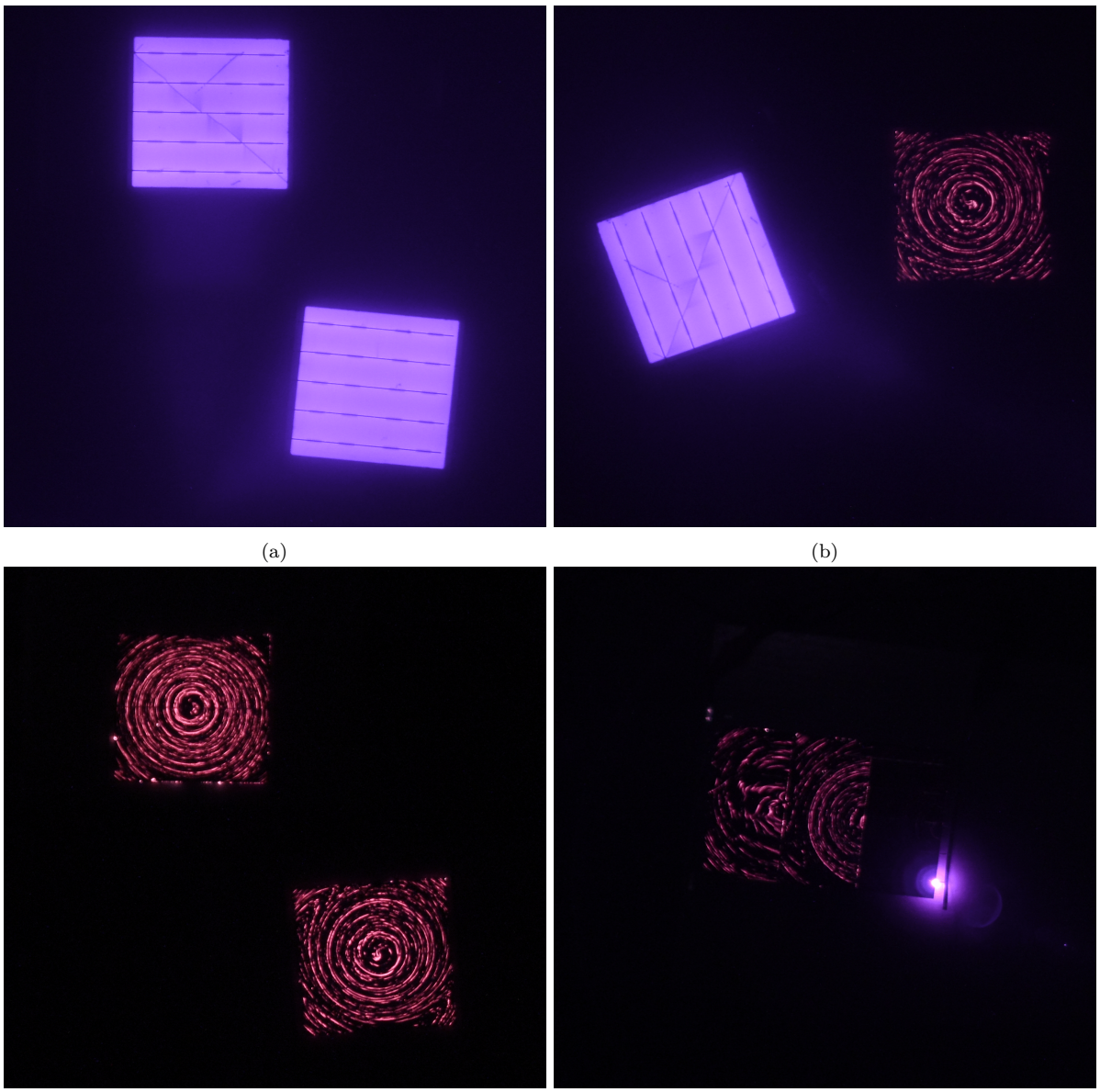

(a) (b)

(c) (d)

Figure C.2: EL images of 2 cells in series: (a) Both in forward, (b) One forward and one reverse, (c) Both reverse, (d) 3 half-cut cells in reverse.

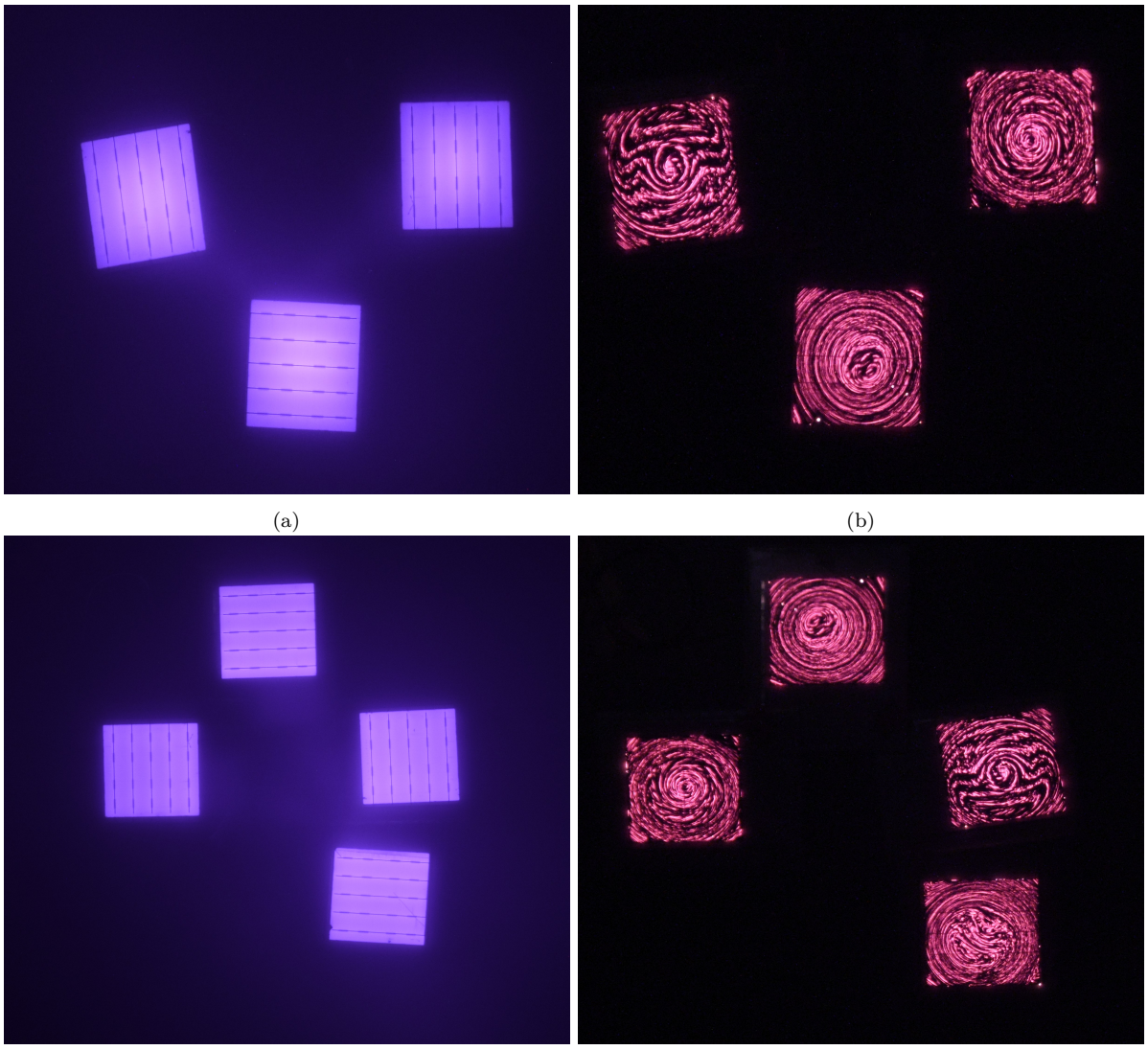

(a) (b)

(c) (d)

Figure C.3: EL images of a series string: (a) 3 cells in forward, (b) 3 cells in reverse, (c) 4 cells in forward, (d) 3 cells in reverse.

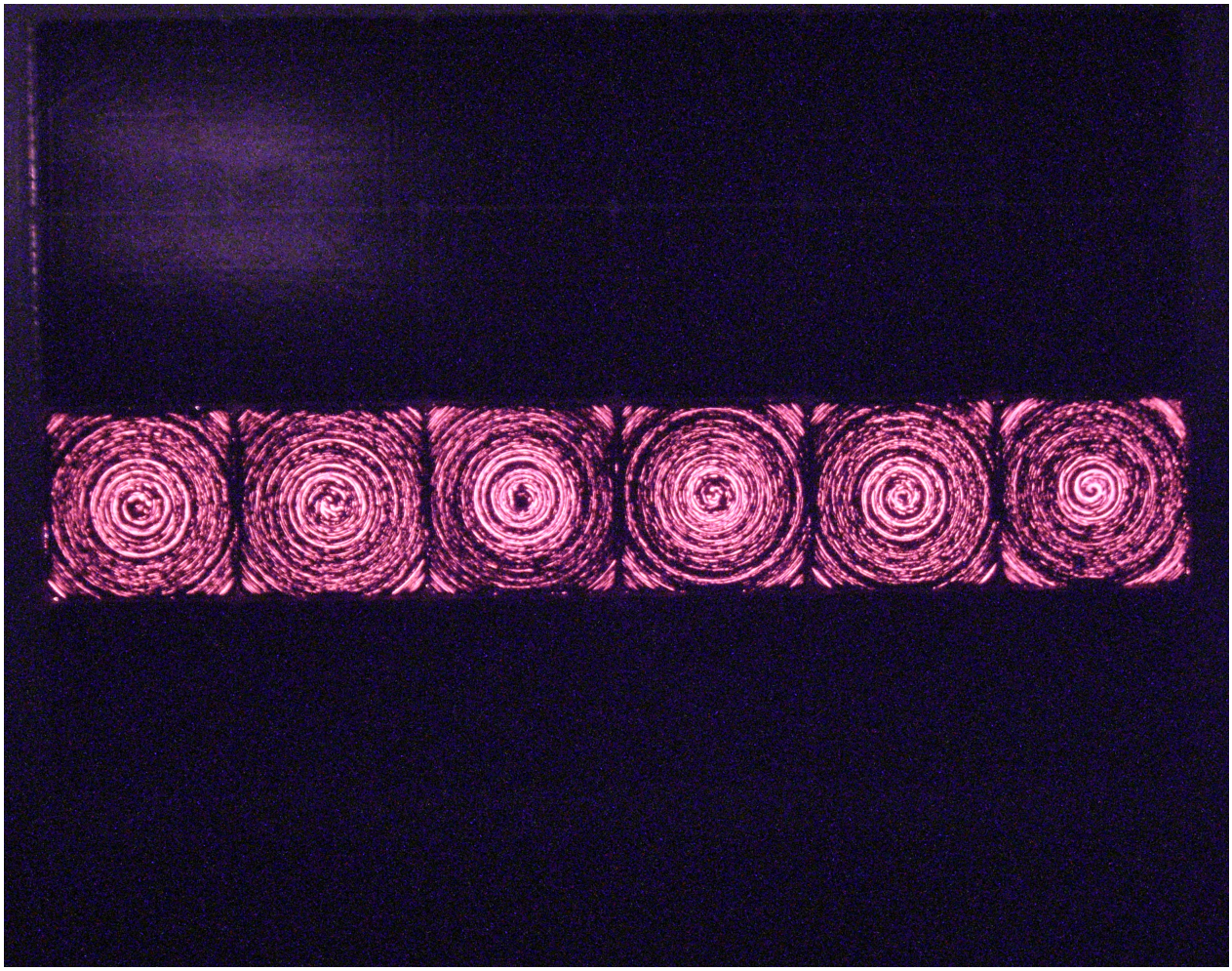

Figure C.4: RebEL image of string of six M-10 full-cells in series showing circular hot-spot pattern.